ABSTRACT

The Maryland Centrifugal Experiment (MCX) has been built to study the confinement of supersonically-rotating plasmas and velocity shear stabilization of MHD instabilities. Theory predicts improved stability and confinement when a strong radial electric field is introduced into a magnetic-mirror geometry. The resulting radial currents establish a stable highly sheared plasma rotating at supersonic velocities in the azimuthal direction under the influence of $\mathbf{J} \times \mathbf{B}$ forces. This arrangement leads to increased confinement because the supersonic rotation creates an artificial radial gravity which draws the plasma away from the mirrors, closing the mirror loss cone. The large v_ϕ shear stabilizes the plasma and enforces laminar flow. Based on these concepts, we have designed and constructed a machine to produce supersonically rotating highly-ionized plasmas. It typically does this by introducing a radial voltage of 7 kV in a magnetic-mirror geometry, 2 kG at the midplane and 19 kG at each mirror. MCX has completed its main construction phase and is acquiring data, here analyzed primarily in terms of a circuit model which infers plasma characteristics from the radial voltage across the plasma and the total radial current. The theory and simulations supporting the MCX centrifugal confinement scheme are presented here with the data and analysis from its first nine months of operation, including a description of basic plasma characteristics and evidence for both stability and confinement. Theory, simulation, and initial experimental data all indicate that this centrifugal confinement scheme provides good stability and confinement at the temperatures and densities under study, as well as at the larger temperatures, fields, and dimensions expected for a fusion reactor. In particular, spectroscopic and circuit-model data indicate rotational velocities in MCX of up to 100 km/s, ion temperatures of approximately 30 eV, and ion densities upwards of $10^{20}\mathrm{m}^{-3}$. These parameters give rotational Mach numbers between 1 and 2 and imply $\partial_r v_\phi \sim 10^6\mathrm{s}^{-1}$. Measurements of the loss times found via our circuit model indicate the neutral density is typically a few times $10^{17}\mathrm{m}^{-3}$. Calculations based on a zero-dimensional MHD model indicate that the plasma is collisional and highly ionized. In this paper, we outline the direct and indirect evidence for supersonic flow, high ($10^{20}\mathrm{m}^{-3}$) ion density, scarce neutrals ($\sim$ 1 neutral per 1000 ions), and a plasma state which is at least quasi-stable. Some notes are given on improvements to the models and how these affect the calculations. We also describe planned improvements to the MCX machine and its diagnostics.

SUPERSONIC ROTATION IN THE MARYLAND CENTRIFUGAL EXPERIMENT

by

Sarah Messer

Dissertation submitted to the Faculty of the Graduate School of
the University of Maryland, College Park in partial fulfillment
of the requirements of the degree of
Doctor of Philosophy
2003

Advisory Committee:

Professor Richard Ellis, Chair
Professor Michael Coplan
Professor George Goldenbaum
Professor Hans Griem
Professor Adil Hassam

ACKNOWLEDGEMENTS

Assistance in construction of the experiment and compilation and interpretation of the data has been gratefully received from Andrew Case, Richard Ellis, Joydeep Ghosh, Alan DeSilva, Deepak Gupta, Adil Hassam, Yi-min Huang, Robert Lunsford, Ronald McLaren, and Catalin Teodorescu. In particular, Joydeep Ghosh has helped greatly by converting raw spectroscopic data into temperature and velocity measurements. I also appreciate the moral support provided by my friends and roommates Maurice Lane III, Jamie Lennon, and Steven Roth.

TABLE OF CONTENTS

LIST OF TABLES

LIST OF FIGURES

ABBREVIATIONS

Symbol	Definition of Symbol	Reference
a	plasma width	
$\mathbf{B}$	magnetic field	
$\mathbf{B_{midplane}}$	magnetic field at the midplane	
$\mathbf{B_{mirror}}$	magnetic field at the mirror throat	
c	speed of light in vacuum, 2.9979×10^8	[18, p. 14]
CCD	Charge-Coupled Diode	
c_S	speed of sound, usually the thermal velocity v_{Ti}	p. 75
C	plasma capacitance	p. 20
C	Coulombs, a unit of charge	
C_0	vacuum capacitance for the plasma geometry	p. 20, F
DOE	U.S. Department of Energy, primary support for MCX	p. 1
$\mathbf{E}$	electric field	
ECRH	electron-cylcotron-resonance heating, a preionization method	p. 50
e_0	charge of a proton, 1.6022×10^{-19} Coulombs	[18, p. 14]
eV	elecron-Volt, 1.6022×10^{-19} J or 11604 Kelvin	[18, p. 14]
FESAC	Fusion Energy Science Advisory Committee	p. 1
HDPE	high-density polyethylene, a plastic	
$I_{crowbar}$	plasma current just before the crowbar	p. 20
ICC	Innovative Confinement Concept	p. 1
IREAP	Institute for Research in Electronics and Applied Physics	
k	Boltzmann's constant, $1.3807 \times 10^{-23} \frac{\mathrm{J}}{\mathrm{K}}$ or $1.6022 \times 10^{-19} \frac{\mathrm{J}}{\mathrm{eV}}$	[18, p. 14]
L	plasma length, axial extent of the plasma	p. 95
M_A	Alfvénic Mach number	p. 75
m_i	ion mass, usually the proton mass, m_p	
m_p	proton mass, 1.6726×10^{-27} kg	[18, p. 14]
M_S	$\frac{v_\phi}{v_{Ti}}$, "sonic" Mach number	p. 75
MCX	Maryland Centrifugal Experiment	
MHD	Magnetohydrodynamics	
n_i	ion density	p. 81
n_0	neutral density	p. 81
P	Pressure	
$\mathcal{P}_{crowbar}$	input $I \cdot V$ power just before crowbar	
q	particle charge	
Q	integration of the current-reversal, stored charge	p. 20
R	plasma resistance	p. 17
$\mathcal{R}$	mirror ratio, $\frac{B_{mirror}}{B_{midplane}}$	p. 1
R_μ	magnetic Reynolds number, $\frac{\mu_0 a v_\phi}{\eta_\perp}$	[18, p. 24]
r_o	outer radius of the plasma	
r_i	inner radius of the plasma	
T	temperature	
T_i	ion temperature	
T_e	electron temperature	
U	electrostatic stored energy, $\frac{1}{2}QV$	
$U_{formation}$	$\int IV\,dt$ energy expended during the formation phase	
UMCP	University of Maryalnd at College Park	
V	machine voltage	
$\mathcal{V}$	plasma volume	
$\mathbf{v_A}$	Alfvén velocity	
$V_{crowbar}$	machine voltage immediately before the crowbar	p. 20
$\mathbf{v_{E \times B}}$	bulk $\mathbf{E} \times \mathbf{B}$ velocity	

v_T	thermal velocity	p. 75
v_{Ti}	ion thermal velocity, $\left(\frac{kT_i}{m_i}\right)^{\frac{1}{2}}$	[18, p. 14]
v_ϕ	rotational velocity	
$v_\parallel$	velocity parallel to the magnetic field	p. 1
$v_\perp$	velocity perpendicular to the magnetic field	p. 1
W	particle energy (Hamiltonian)	
Z	average ionization state, $n_e \equiv Z n_i$	
$Z_{crowbar}$	plasma $\frac{V}{I}$ impedance just before crowbar	
$\beta_{rotation}$	ratio of rotational to magnetic energy densities	p. 75
$\beta_{thermal}$	ratio of thermal to magnetic energy densities	[18, p. 29]
η	resistivity	
$\eta_\parallel$	parallel resistivity	
$\eta_\perp$	perpendicular resistivity	
ϵ	permittivity	
ϵ_0	permittivity of free space, 8.8542 $\times 10^{-12}$ F/m	[18, p. 14]
λ_D	Debye length, the length scale for screening charge	[5, p. 49], C.1.2
Λ	$\ln \Lambda$ is the Coulomb logarithm	[18, pp. 34-35]
μ	magnetic moment of a particle	p. 65
μ_{plasma}	magnetic permeability	
μ_0	permeability of free space, $4\pi \times 10^{-7}$	[18, p. 14]
ν_e	electron collision rate	[18, p. 28]
ρ_e	electron gyroradius (electron Larmor radius)	[18, p. 28]
ρ_i	ion gyroradius (ion Larmor radius)	[18, p. 28]
σ_0	atomic collision cross-section, 8.7974 $\times 10^{-21}$	[18, p. 14]
σ_{CX}	charge-exchange cross-section	
τ_{CX}	charge-exchange time	
τ_E	energy confinement time	p. 93
τ_e	electron collision time = $\frac{1}{\nu_e}$	
τ_M	momentum confinement time	p. 93
Φ	electric potential	
ω_{pe}	electron plasma frequency	
ω_{pi}	ion plasma frequency	
Ω	rotational frequency	

Chapter 1: Introduction

The Maryland Centrifugal Experiment (MCX) is part of an ongoing effort to develop nuclear fusion as a viable power production method. As such, it is funded by the U.S. Department of Energy's (DOE's) Innovative Confinement (ICC) program. The ICC experiments explore plasma confinement schemes other than tokamaks. While the torus-shaped tokamak plasmas are the major components in fusion-oriented research, they face several obstacles which ICC research is intended to understand and mitigate, possibly through the development of alternative concepts for reactor design. The goal of this research is to suggest modifications to be made to tokamaks or to suggest alternative devices which may replace tokamaks as the leading fusion-plasma devices.

MCX is funded by the ICC program to explore an idea called centrifugal confinement. This concept relies on inducing supersonic rotation in a mirror-confined plasma. Supersonic rotations stabilize the MCX plasma and reduce losses of heat and particles, resulting in long-lived, highly-ionized plasmas. In this paper we will display the evidence that MCX generates a quasi-stable, high-density, highly-ionized supersonically rotating plasma.

1.1 Mirror Confinement

A mirror machine uses a cylindrical geometry with an axial-directed magnetic field that is strongest near either end and weaker near the midplane to obtain "mirror confinement". (See figure 1.1.) This inhibits the plasma from escaping radially and yields slower axial loss than would be expected of a uniform $B\hat{\mathbf{z}}$ field, since only those particles with $\frac{v_\parallel}{v_\perp} > \sqrt{\mathcal{R}-1}$ can escape, where $v_\parallel$ and $v_\perp$ are the components of particle velocity parallel to and perpendicular to the magnetic field (as measured at the midplane), and $\mathcal{R}$ is the mirror ratio, the ratio of magnetic field strength at the ends ("mirrors") to the strength at the midplane. [12, p. 40] Since the lost particles forms a cone in velocity space, it's commonly referred to as the "mirror loss cone." Since collisions randomize particle velocities, particles are rapidly lost out the ends of a mirror machine as long as the density is high enough to provide regular collisions. More details on mirror confinement may be found in appendix C.

Figure 1.1: Mirror Machine Geometry: The magnetic field and the simultaneous conservation of both total energy and magnetic moment traps the plasma in the shaded region. the thin curves show the shape of the magnetic field, and have been erased from the area outside the vacuum vessel (the large box). The smaller squares with X's show positions of the electromagnets.

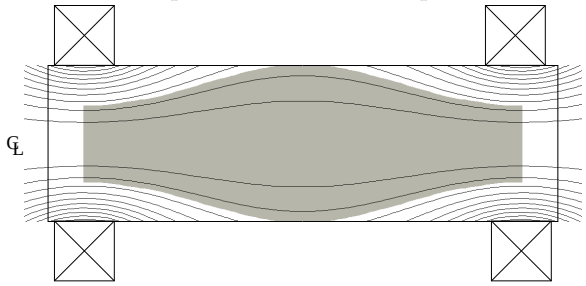

1.2 Centrifugal Confinement

In MCX, the mirror magnetic field is augmented by a radial electric field maintained by a central electrode. (See figure 1.2.) Under the force-free approximation, the Lorentz equation, $\mathbf{F} = q(\mathbf{E} + \mathbf{v} \times \mathbf{B})$, causes the plasma to rotate in the azimuthal direction at a velocity

$$\mathbf{v}_\phi = \frac{\mathbf{E} \times \mathbf{B}}{\mathbf{B^2}} = \frac{E_r}{B_z}\hat{\phi} \tag{1.1}$$

For centrifugal confinement to be effective, the rotational velocity must be substantially faster than the ion thermal speed; theory shows confinement increasing with Mach number, with the strongest confinement at Mach numbers of

$$M_S = \frac{v_\phi}{v_{Ti}} \gtrsim 3 \tag{1.2}$$

Details of this scheme can be found in appendix D.

1.2.1 Reduction of Mirror End Losses

High-speed rotation provides several improvements over the conventional mirror machine. The first improvement is that the axial losses of the mirror machine are greatly reduced, since escaping particles must have sufficient speed parallel to $\mathbf{B}$ that they may kinematically overcome the centrifugal potential formed by the tightening of magnetic field lines near the ends [27, p. 20]. A detailed comparison of the confinement features of mirror machines and the MCX centrifugal confinement is given in appendix G. The pressure gradient along a single magnetic field line has been calculated by Hassam [16], under the assumption of a uniform temperature. He finds

Figure 1.2: Geometry for centrifugal confinement: The plasma (shaded region) is trapped between the magnetic field lines as shown by the B field and the velocity shear and confined to large radii by the centrifugal force. The width of the plasma at the midplane is a.

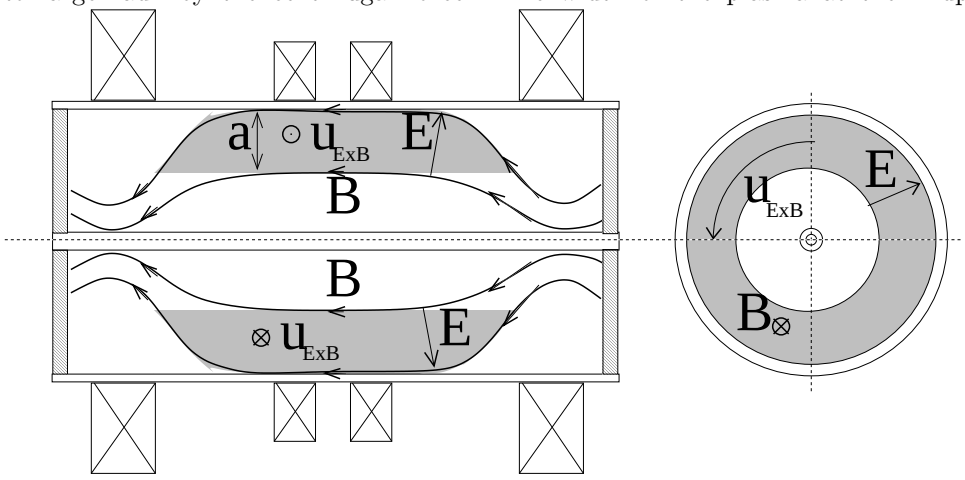

$$P(\Psi, r) \propto e^{\frac{m_i r^2 \Omega^2}{2kT}} \tag{1.3}$$

where r is the local radius of the field line Ψ, Ω is the angular velocity of the field line, and m_i is the mass of individual ions in the plasma.

1.2.2 Improved Stability from Velocity Shear

The second benefit of the rotation is that it is not uniform, but shaped into a highly-sheared profile by viscous and other effects. (See appendix E.) This has the benefit of breaking up convective cells and providing great stability to the Rayleigh-Taylor interchange mode and other typical plasma instabilities [15]. For velocity shear to stabilize the plasma against an interchange mode with azimuthal wavenumber k_ϕ, the velocity shear v'_ϕ must satisfy the following relations:

$$v'^{\,2}_\phi \gtrsim (g\kappa) \ln \frac{\sqrt{g\kappa}}{\mu k_\phi^2} \tag{1.4}$$

$$g = \frac{v_\phi^2}{r} \tag{1.5}$$

$$\kappa = \frac{\partial_r n_i}{n_i} \tag{1.6}$$

Here, g is the centripetal acceleration, κ is the scale of the radial density gradient, and μ is the viscosity. In a cylindrical system, k_ϕ cannot be smaller than $1/(2\pi r)$. It should also be noted that if the second derivative of the velocity v''_ϕ is nonzero, the plasma is also subject to the

formation of turbulent convective cells by the Kelvin-Helmholtz instability [15].
The promising confinement and stability characteristics of the centrifugal confinement scheme are the primary motivations behind the development of the MCX experiment because they allow the plasma to reach high temperatures and high levels of ionization. (See appendix F.)

1.3 Author's Contributions to the Experiment

The author joined the MCX group in June 1999 and began checking and running several codes to calculate the magnetic and electric fields, and to predict plasma performance for a variety of vessel and magnet geometries. Based in large part on these calculations, Rick Ellis and Adil Hassam submitted a proposal to DOE during spring 2000. After we received notification of funding, the author moved her office into the lab which had until that point housed the Maryland Spheromak and other experiments managed by Alan DeSilva. There she continued design calculations, including predictions of coil heating and mechanical stresses, and began removing hardware from the laboratory. Later she took a prime position in moving new power supplies, magnets, and other hardware into the laboratory, running cable, designing a data collection and control system, and testing power supplies and magnets. The author also assisted in the design and installation of the vacuum chamber and pumps and played a leading role in acquiring and interpreting the first year's worth of test and data runs.
In addition, the author designed and programmed the computerized control and data acquisition system, including specification and installation of hardware, design and programming of the software, and connection of the computer system to the diagnostic hardware.

1.4 Summary of Results

As of this writing, MCX has been reliably producing dense, quasi-stable, highly ionized, supersonically-rotating plasmas for nine months. This document outlines the current capabilities of the device and the data measuring the critical parameters of rotational velocity and ionization fraction, focusing on the evidence for a quasi-stable plasma with $n_i \sim 10^{20}\mathrm{m}^{-3}$, $M_S \sim 1.3$, and the ratio $n_0/n_i \lesssim 0.001$. The theoretical and circuit models used here for prediction and analysis are fairly simple: The plasma is modeled as a resistor and capacitor in parallel, with values of R and C that change slowly compared with the digitizer sampling and MHD time scales. Better-developed models are outlined in the appendices, as are detailed descriptions of the hardware, power supplies, and diagnostics used on the experiment.

1.5 Structure of this Dissertation

Chapter 2 gives an overview of the theory supporting the MCX centrifugal confinement scheme. In chapter 3, we briefly describe the MCX machine and our primary diagnostics. In chapter 4, we describe the simple numerical models which form the basis for our analysis. Much of the data we've collected is described and compared in chapter 5, including both qualitative and quantitative features of the plasma and measured dependencies of a large number of quantities on the controllable parameters. Chapter 6 outlines our plans for improvements of both the plasma diagnostics and machine hardware, describing why such improvements are necessary and what we have been able to determine from preliminary tests. Our conclusions are summarized and presented in chapter 7.

The appendices give greater detail on, and more rigorous derivations of, many of the concepts outlined in the main body of the dissertation. Appendix A describes the machine hardware and capabilities. Appendix B gives more details on the spectrometry system and describes how it is used to measure the plasma's temperature and velocity. An overview of the physics for the mirror confinement scheme is given in appendix C, and a similar treatment for centrifugal confinement is given in appendix D. Appendix E gives estimates of the magnitude and importance of velocity shear, and in appendix F we examine the ion and neutral densities and make several estimates of the plasma's ionization fraction. Appendix G examines a number of issues related to containing heat, momentum, and particles in the plasma. Appendix H discusses a number of revisions and improvements to the models used in this dissertation, which might be used to provide more clear and precise results than what are presented herein. Finally, Appendix I lists and quantifies all the well-defined trends observed in the data up to this point.

Chapter 2: Centrifugal Confinement Theory

In this chapter we outline the theoretical underpinning of the centrifugal confinement scheme used to design MCX. In particular, we examine the motion of individual particles, the MHD fluid equations, and the differences between rotating and non-rotating plasmas in a magnetic mirror. Those wishing more detail are referred to the cited sources and the appendices C, D, and E.

2.1 Cause of Plasma Rotation

Individual charged particles in combined electric and magnetic fields are subject to the Lorentz force,

$$\mathbf{F} = q(\mathbf{E} + \mathbf{v} \times \mathbf{B}) \tag{2.1}$$

The nature of this force may be most easily illustrated by imagining its effect upon an initially-stationary test charge. At $t = 0$, its velocity is zero, so we may ignore the magnetic field, and the particle's acceleration is:

$$\dot{\mathbf{v}} = \frac{q}{m}\mathbf{E} \tag{2.2}$$

If this acceleration is parallel to B, the magnetic field has no effect and the charge is accelerated continuously, but if the acceleration is perpendicular to B, the increasing speed of the particle causes an increasing perpendicular acceleration. The combination of these two effects yields a velocity which is the sum of two components: [12, pp. 24-27] The first is the drift of a "guiding center", which moves at the unique velocity for which the electric and magnetic terms in the Lorentz force equation exactly cancel:

$$\mathbf{v}_{gc} = \frac{\mathbf{E} \times \mathbf{B}}{B^2} \tag{2.3}$$

The second component of the motion is a circular orbit of our test particle about this guiding center, with the magnitude and direction of the magnetic component of the force varying throughout the orbit. The orbit has a radius and frequency given by:

$$\rho_c = \frac{mE}{qB^2} \tag{2.4}$$

$$\omega_c = \frac{qB}{m} \tag{2.5}$$

We note that the $\mathbf{E} \times \mathbf{B}$ drift velocity $\mathbf{v}_{gc}$ and gyrofrequency ω_c are both independent of initial conditions, while the gyroradius is not. In addition, the drift velocity is independent of both charge and mass, so that in a plasma with both ions and electrons at some initial randomized distribution, the electromagnetic forces will cause a bulk drift at the guiding center velocity and net currents and charge distributions which tend to make $\mathbf{E} \cdot \mathbf{B}$ small. For a Maxwellian distribution, the typical gyroradius is the Larmor radius,

$$\frac{v_{Ti}}{\omega_c} = \frac{\sqrt{mkT}}{qB} \tag{2.6}$$

2.2 Characteristics of Plasma Rotation

2.2.1 Magnetic Surfaces are Rigid Rotors

To examine plasma rotation, we will first compare the relative velocities of different fluid elements on the same magnetic flux surface. We assume an axisymmetric magnetic field with no azimuthal component and write

$$\mathbf{B} = \nabla\phi \times \nabla\psi \tag{2.7}$$

where ϕ is the azimuthal coordinate and $\nabla\phi = \frac{1}{r}\hat{\phi}$. Then we may write the electric field in terms of its scalar potential as $\mathbf{E} = -\nabla\Phi$. From the generalized Ohm's Law for MHD plasmas, the assumptions that collisions are more frequent than the time scales of interest and that $m_i \nabla P_e >> m_e \nabla P_i$, we may write for a plasma current density $\mathbf{j}$ and resistivity η [5, p. 267]:

$$\mathbf{E} + \mathbf{v} \times \mathbf{B} - \eta\mathbf{j} = \frac{1}{ne_0}(\mathbf{j} \times \mathbf{B} - \nabla P_e) \tag{2.8}$$

Using order-of-magnitude estimates from theory and experimental data, we find that the leftmost two terms in this equation are much larger than any of the others, confirming that $\mathbf{E} \times \mathbf{B}$ motion is the dominant motion of the plasma and allowing us to write:

$$\nabla\Phi = \mathbf{v} \times \mathbf{B} \tag{2.9}$$

Equation 2.9 shows that the magnetic and electric fields are perpendicular to each other and to the plasma velocity, so we may drop the vector notation and write

$$v = \frac{|\nabla\Phi|}{B} = \frac{|\nabla\Phi|}{|\nabla\phi \times \nabla\psi|} \tag{2.10}$$

Since our magnet coils are approximately axisymmetric with only azimuthal components of current, we may assume that $\nabla\psi$ has no large azimuthal component, so that [8]

$$v = \frac{1}{|\nabla\phi|}\frac{|\nabla\Phi|}{|\nabla\psi|} \tag{2.11}$$

$$\mathbf{v} = r\hat{\phi}\frac{d\Phi}{d\psi} \tag{2.12}$$

By assumption, neither Φ nor ψ has a significant azimuthal component, and since $\mathbf{E}\cdot\mathbf{B} \approx 0$ from equation 2.9, $\frac{d\Phi}{d\psi}$ can be written as a function purely of ψ. Because of this, we have

$$\mathbf{v} = r\Omega\hat{\phi} \tag{2.13}$$

$$\Omega(\psi) = \frac{d\Phi}{d\psi} \tag{2.14}$$

where $\Omega(\psi)$ is the rotational frequency of the magnetic surface ψ. A further discussion of the rotation and its effects on the plasma may be found in appendix D.

2.2.2 Velocity Profile

Although individual flux surfaces are rigid rotors, the rotational frequency $\Omega(\psi)$ may have a non-trivial form, with successive surfaces moving at different angular velocities due to a combination of effects from viscosity, variations in current density and magnetic field. Therefore we expect that a typical MCX velocity profile will be sheared with a substantial angular velocity gradient. As we will show below, this velocity shear is expected to stabilize the plasma against pressure-driven instability modes. (See section 2.3.2.)

2.3 MHD Equilibrium and Stability

The same set of assumptions that led to equation 2.8 lets us write for the mass density ρ and pressure P, [5, p. 266, 274-275]

$$\rho\frac{d\mathbf{v}}{dt} = \mathbf{j}\times\mathbf{B} - \nabla P \tag{2.15}$$

$$\rho(\partial_t\mathbf{v} + (\mathbf{v}\cdot\nabla)\mathbf{v}) = \mathbf{j}\times\mathbf{B} - \nabla P \tag{2.16}$$

2.3.1 MHD Equilibrium

We now also assume that the system is in steady-state, so that $\partial_t \mathbf{v} \approx 0$, and use the ion/electron mass ratio to write $\rho \approx n m_i$, where we have assumed quasineutrality, $n_e \approx Z n_i \equiv Z n$: [8]

$$n m_i (\mathbf{v} \cdot \nabla)\mathbf{v} = -\nabla P + \mathbf{j} \times \mathbf{B} \tag{2.17}$$

We may use the dot-product of this equation with the magnetic field $\mathbf{B}$ and the identity $\nabla = \frac{1}{r}\hat{\phi}\partial_\phi + (\nabla\psi)\partial_\psi + \mathbf{B}\partial_B$ to calculate the pressure profile. We assume that temperature is constant along a field line: [8]

$$P = (Z+1)nT \tag{2.18}$$

$$\mathbf{B} \cdot (n m_i (\mathbf{v} \cdot \nabla)\mathbf{v}) = \mathbf{B} \cdot (-\nabla P + \mathbf{j} \times \mathbf{B}) \tag{2.19}$$

$$n m_i \mathbf{B} \cdot ((\mathbf{v} \cdot \nabla)\mathbf{v}) = -(Z+1)T\mathbf{B} \cdot \nabla n \tag{2.20}$$

From equation 2.13, we calculate

$$(\mathbf{v} \cdot \nabla)\mathbf{v} = r\Omega \frac{1}{r}\partial_\phi (r\Omega\hat{\phi}) = -r\Omega^2 \hat{\mathbf{r}} = -\frac{1}{2}\Omega^2 \nabla r^2 \tag{2.21}$$

Combining these gives the steady-state density profile along an isothermal magnetic surface when we define a spatial coordinate l to be the distance along a field line:

$$-n m_i \mathbf{B} \cdot (\frac{1}{2}\Omega^2 \nabla r^2) = -(Z+1)T\mathbf{B} \cdot \nabla n \tag{2.22}$$

$$n m_i B \frac{1}{2}\Omega^2 \partial_l r^2 = (Z+1)TB\partial_l n \tag{2.23}$$

$$n m_i \frac{1}{2}\Omega^2 \partial_l r^2 = (Z+1)T\partial_l n \tag{2.24}$$

$$\frac{m_i \Omega^2}{2(Z+1)T}\, d(r^2) = \frac{1}{n}\, dn \tag{2.25}$$

$$n = n_0 e^{\frac{m_i r^2 \Omega^2}{2(Z+1)T}} \tag{2.26}$$

$$P = P_0 e^{\frac{m_i r^2 \Omega^2}{2(Z+1)T}} \tag{2.27}$$

$$P = P_0 e^{\frac{M_S^2}{2(Z+1)}} \tag{2.28}$$

Thus as one travels along a field line from small to large radius, one sees an exponential increase in both density and pressure. Since large radii correspond to the midplane of the device and small radii to the magnetic mirrors, this is just what we want for confinement. In the more realistic case, temperature T is not constant on a magnetic surface, but is higher near

the midplane than near the mirror, so that the pressure gradient is somewhat steeper than indicated above. Since the square of the Mach number is present in the exponential, even modest supersonic rotation should give noticeable improvement over mirror machines, and $M_S \sim 4$ should reduce the end losses of a hydrogen plasma to a few percent of those in a mirror machine of comparable characteristics.

2.3.2 Stability Requirements

Two types of instabilities are regularly discussed in connection with the MCX plasma, according to whether they are driven by pressure or velocity gradients. Interchange modes such as those driven by pressure gradients can be stabilized by high velocity shear [8], [15], [16]. For a given velocity gradient scale length $\frac{a}{2}$, plasma length L, and Reynolds number R_μ, the interchange mode will be stabilized for rotational Mach numbers

$$M_S > \sqrt{\frac{a}{2L} \ln R_\mu} \tag{2.29}$$

In part because of the dependence of the RHS on machine geometry, MCX has been designed with substantial elongation; $\frac{L}{a} \sim 7$. For typical MCX plasmas of $a \sim 0.21$ m, $L \sim 1.4$ m, and $R_\mu \sim 2000$, the RHS of the above criterion is 0.76. Thus supersonic rotation should be sufficient to suppress pressure-driven interchange modes.

Velocity-driven instabilities are somewhat harder to describe analytically, although it is known that turbulent convective cells will not be driven if the velocity profile is linear (i.e. $v_\phi'' = 0$). Since we expect non-slip boundary conditions, the second derivative of velocity will have to be finite somewhere. Based on numerical MHD codes, [17] we believe that convective cells will only form near the middle of the plasma, where neighboring magnetic surfaces are co-rotating, and thus will not contribute significantly to the transport of heat or particles to the walls.

Chapter 3: Experimental Apparatus

3.1 Design Considerations

The author worked closely with the co-PIs on the design, construction, and testing of the MCX device, and since the centrifugal confinement scheme is not common, the various design criteria and how they were met will be briefly discussed here.

3.1.1 End Insulators

Rotation of the MCX plasma requires the maintenance of a radial electric field. (See sections 1.2 and 2.1.) Since electrons can flow easily along magnetic field lines, the electric field can not be sustained on any magnetic surface that intersects a conductor allowing electrons to flow across the field. The flow of charged particles along a magnetic field line may be interrupted by the presence of an insulator, and the electric field thus maintained in the plasma. Therefore rotation requires that the plasma bounded at either end by insulating discs.

3.1.2 High Mirror Ratio

Second, both mirror confinement and centrifugal confinement are more effective if the mirror ratio $\mathcal{R}$ is as high as possible. (Since equation 2.27 predicts a rapid increase in pressure with radius, and since $r^2 \propto B$ on a given magnetic surface, a large mirror ratio means that the difference $r^2_{midplane} - r^2_{mirror}$ is also large. This implies a very large pressure difference between the midplane and the mirror.) This criterion is moderated by the need to have the plasma magnetized - the electron and ion Larmor radii must be much smaller than the plasma dimensions if we are to use the MHD equations upon which the centrifugal confinement scheme is based, and if we are to extrapolate MCX's performance to fusion conditions. Additionally, strong magnetic curvature can drive instabilities, so the magnetic field should look like a solenoidal field ($B_z >> B_r$) near the midplane. It is the combination of these requirements which gives MCX the magnetic field shape it has, with strong magnetic coils having a small bore at either end and weaker, larger-bore magnets near the midplane. These criteria also brought us to design MCX around a nominal mirror ratio of 9. Since the plasma stretches along magnetic field lines, and the conducting steel vessel should not cut those field lines, the

shape of the vacuum vessel should approximate the magnetic geometry in a rotating system such as ours.

3.1.3 Core Electrode

Another major consideration was the support and design of the central electrode. For target ion temperatures of a few tens of electron-Volts, and target magnetic fields of a few kilogauss, supersonic rotation and the machine dimensions require the core to reach several kilovolts and to carry currents of several kiloamps. In addition, any substantial sagging of the core due to gravity or electrostatic effects would introduce perturbations into the plasma flow profile and lead to oscillations in the magnetic field seen by individual particles as they orbited the core. Such perturbations in magnetic field are responsible for banana orbits in tokamaks and would yield increased transport, decreasing plasma temperature and density. Therefore, the core was designed to be made of a single piece of rigid steel pipe, supported at either end by insulating discs.

3.1.4 High-Voltage Feedthrough

Next was the matter of the high-voltage feed-through. A high-current, high-voltage vacuum feed-through with a large plasma-facing insulator capable of supporting the 20 kilogram weight of the core was not commercially available. One was therefore designed. Our initial attempt showed evidence of plasma breakdown in the region outside the insulating discs, so the core was clad in insulating tubes and additional insulators were used to supplement the discs, improving their fit to the vessel wall so that hot gas would not be able to travel from the main chamber to the end regions.

3.1.5 Inclusion of Existing Power Supplies

To provide the best experimental capabilities possible on a limited budget, MCX was also designed around the inclusion of a number of expensive pieces of hardware already available at IREAP. These included both large DC power supplies, the capacitor bank which provides voltage to the core, and the electromagnets.

Figure 3.1: MCX Construction: This cut-away view of the machine shows the design and positioning of the MCX vacuum vessel, including the core (The high voltage feed-through is on the right.), the MS coils (midplane), and the O coils near either end. Also visible are the insulating discs just outside the O coils.

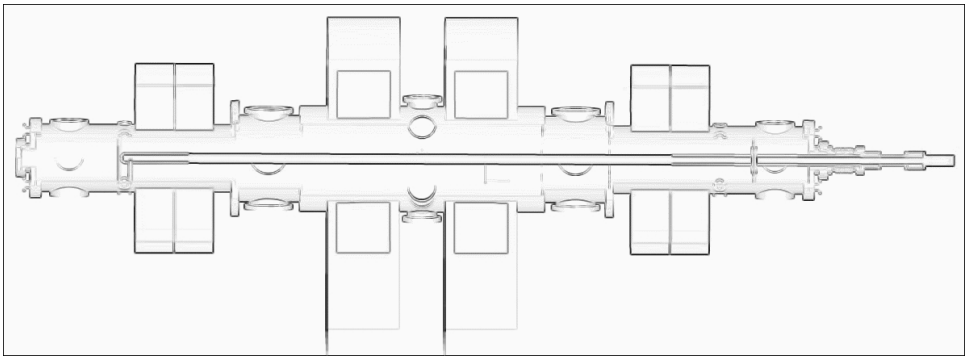

3.1.6 Large Range of Experimental Parameters

Since MCX was exploring new concepts, we tried to keep as much variability as possible in the operational parameters. The mirror and midplane magnetic fields, the radial electric field, and the fill pressure may all be varied easily. With some work, it is also possible to move the magnets and insulating discs by small amounts along the axis of the machine, changing the shape of the field and the details of the boundary conditions. Some provisions have also been made for the possible introduction of an azimuthal (or toroidal) magnetic field and gas puffing through the center of the core. Considerations of servicing and installation led to the design of a vacuum vessel in three parts, with a small number of large O-ring seals and a majority of high-vacuum Conflat seals.

3.1.7 Diagnostic Ports

Finally, to provide as much diagnostic access as possible, the vacuum vessel was designed with a large number of large diagnostic ports, particularly near the midplane, where four large tangential ports are available for Doppler spectroscopy and similar diagnostics of the plasma rotation. (See figure 3.3.) The capabilities of the machine and a mechanical drawing of the finished project are shown in table 3.1 and figure 3.1. More details on MCX construction may be found in appendix A.

Table 3.1: Operational Parameters on MCX

Quantity	Min	Max	Typical	Units
Midplane Magnetic Field	-0.23	0.23	0.2	Tesla
Mirror Magnetic Field	-1.9	1.9	1.8	Tesla
Initial Core Voltage	-11	11	-7	kV
Mirror Ratio	-13.9	20.8	9	
Fill Pressure	2×10^{-7}	5×10^{-2}	5×10^{-3}	Torr
Fill Gas	H_2, He, Ar		H_2	

3.2 Machine Capabilities

The MCX device uses three high voltage power supplies. Two of these are DC power supplies which drive the magnetic field coils at the mirrors and midplane. (See figure 3.1.) These coils and power supplies may be used to generate fields of up to 1.9 Tesla at either mirror and up to 0.23 Tesla at the midplane, with a typical mirror ratio of 9. The magnetic geometry for this case is shown in figure 3.2. The third power supply is an 11 kV, 1.23 mF capacitor bank which is used to supply voltage and current to the machine's center electrode, a stainless steel tube. The connections of the core to the capacitor bank can be altered to supply either positive or negative voltage.

The vacuum vessel is 55 cm diameter at the midplane with 3.26 meters between the two insulators which cut the magnetic field lines outside the mirror planes. The mirror planes themselves are separated by about 2.6 meters. When the vessel is evacuated, its base pressure is about 10^{-7} Torr ($\sim 4 \times 10^{15}$ particles per cubic meter.) It is typically filled with hydrogen to a pressure of about 5 mTorr, for $\sim 10^{20}$ H atoms per cubic meter.

At this time, the system has three principal diagnostics: a visible-light and near-UV spectrometer, several $\dot{\mathbf{B}}$ probes, and a recording of the current and voltage supplied to the plasma. The spectrometer views the plasma tangentially at the midplane and uses the Doppler shift and broadening of carbon impurity lines to measure the velocity and temperature of the plasma. The spectroscopy signal is gated to provide integration over times as short as 100 μs and collimated to a path about 1 centimeters thick. [11] (See figure 3.3.)

The $\dot{\mathbf{B}}$ probes and the current and voltage supplied to the core are each recorded at one million samples per second for eight milliseconds. The plasma current is measured through a Rogowski coil [7], and the core voltage is monitored using a resistive voltage divider. The $\dot{\mathbf{B}}$ signals imply rotation at the same velocity as that measured by spectroscopy, and the current and voltage

Figure 3.2: Vacuum calculations of the magnetic field in MCX for mirror ratio $\mathcal{R} = 9$: This is a schematic of one quadrant of the MCX machine, showing the positions of the major hardware in relation to the magnetic field surfaces. The machine midplane is at the bottom of the plot, and its axis of symmetry is on the left. The dark gray bars on the right show the positions of the field coils. (Each of these bars is actually a sequence of overlapping circles. Each circle is centered at the actual location of one turn of a magnet coil and has a radius which indicates the amount of current flowing through that turn. Separate bars therefore represent groups of closely-spaced turns within individual coils.) The long vertical black bar on the left represents the core. The grey rectangles near the top show the positions of the insulators which support the core and cut the magnetic field lines. The series of step-like lines from z=200 cm to r=27 cm show the shape of the vacuum vessel. Note that the radial and axial scales differ.

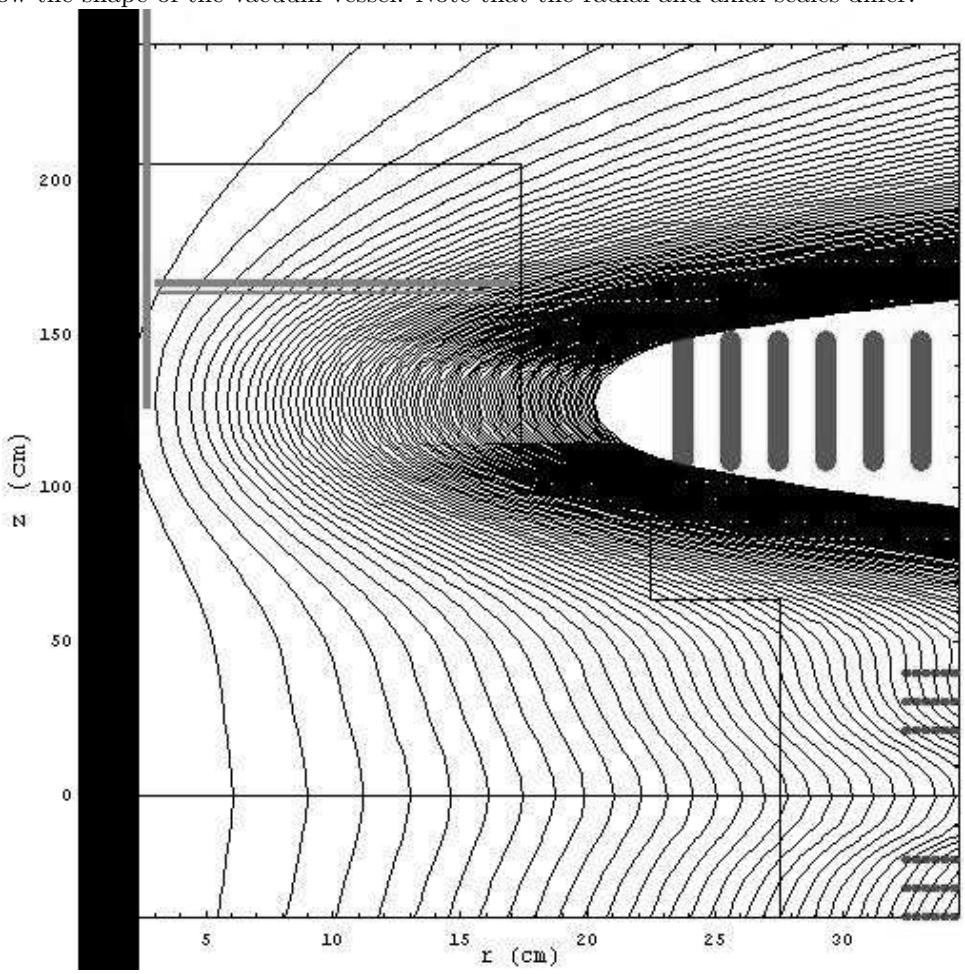

Figure 3.3: Spectrometry Layout: When viewing the plasma through the bottom tangential port through lens L_3, a red shift is observed. When using mirror M_1 and M_2 and lenses L_1 and L_2 to view the plasma through the top tangential port, a blue shift is observed. Both Doppler shifts are of the same magnitude, consistent with plasma rotation.

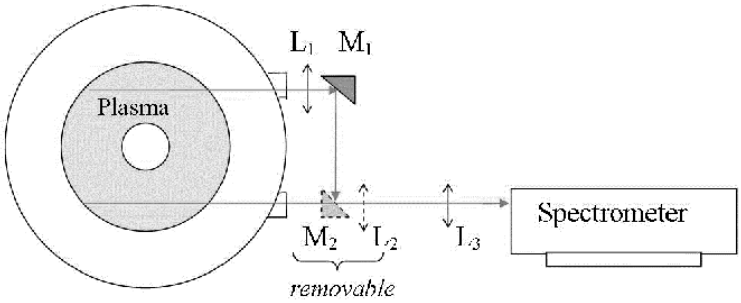

traces are consistent with a dense highly-ionized plasma rotating at this same velocity, typically about 70 km/s.

More details on the construction of the MCX experiment may be found in appendix A. More information on the Doppler spectrometry may be found in appendix B.

Chapter 4: Models and Conventions

For the purposes of this dissertation, we adopt several simple models to approximate the MCX plasma. Those readers interested in the detailed justification of these models and possible improvements to them should refer to appendices C, D, E, F, and H.

The MCX temperatures, densities, length scales, and time scales are such that MHD and the Frozen-In Theorem provide good approximations to the plasma dynamics. (See section C.1 for details on these models and the calculations supporting their application to the MCX plasma.) The volumes near the mirror planes and near the vessel walls will have somewhat different properties, but since these are believed to be small regions, the corrections to MHD necessary to accurately model the edges will be ignored.

In this paper, all temperatures will be given in terms of the associated particle energies in electron-Volts (eV) and all other quantities in their typical SI units, except when otherwise noted. For reference, 1 eV equals 11604 Kelvin or 1.6022×10^{-19} Joules [18, p. 17]. In these units, Boltzmann's constant is $k = 1.6022 \times 10^{-19}$ J/eV, although we will often omit k from being explicitly written in our formulae.

In this paper, the terms "supersonic" and "sonic Mach number" are used to compare the azimuthal speed v_ϕ to the ion thermal speed, $v_{Ti} = \sqrt{\frac{kT}{m}}$. While it is recognized that this is not the same as the plasma sound speed, the chosen terminology is judged to be less confusing than terms like "superthermal" or "thermal Mach number".

4.1 Measurements of Plasma Parameters from Circuit Model

The current passing through the core and the voltage between the core and the vacuum vessel are used to determine plasma properties. Both are digitized by CAMAC modules at a rate of 1 MHz. (See section A.7.)

The current and voltage traces allow measurements of the plasma resistance and input power as functions of time, and when the crowbar is fired, the current and voltage monitors allow us to measure the charge stored on the core due to the coaxial system's capacitance. (See figure 4.1.) These numbers can be used to estimate the rotational speed and the ion and neutral densities as well as the thermal energy and momentum confinement times. Figure 4.1 shows the records of voltage and current for a typical run.

The utility of the crowbar-based measurements clearly rests on the repeatability of the

Figure 4.1: Circuits for supplying voltage to the core, and for modeling the plasma response: The capacitor bank (C = 1.7 mF, section A.5.3) is shown on the left, with its voltage and current monitors, V_B and I_B. The resistor R=0.5 Ohms is a series resistor included in the circuit to limit the capacitor bank's output current. The ignitrons are high-current, high-voltage mercury-vapor switches which close within 2 μs after receiving a trigger pulse, but which cannot be re-opened until the current through them ceases. (See section A.5.2) The Start Ignitron is typically closed 100 μs after the CAMAC system (section A.7) begins collecting data. The Crowbar Ignitron is fired later in the shot, typically at 1.6 ms, in order to measure the ion density. (See section 4.1.2.) V_P and I_P measure the voltage and current applied to the core electrode. Both experimental data and theoretical considerations imply that the plasma may be modeled as a resistor and capacitor in parallel; see [20] and [1]. This model compares will with simulations and with a "dummy load" consisting of a resistor and capacitor in parallel. (See section H.3.) At the same time, there will be some leakage current which may be modeled as a resistor. The Free Wheeling Ignitron is planned but not yet implemented, and is described briefly in section 6.3.

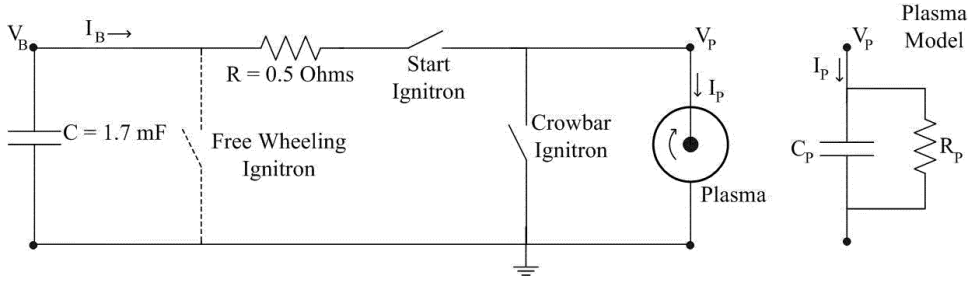

Figure 4.2: Sample Voltage and Current Traces: The plots below show the voltage (top) and current (bottom) evolution for a typical shot (number mcx030612-26). The circles mark the following transitions: 1) Firing of the Start Ignitron and beginning of the shot; 2) End of the Holdoff phase and beginning of plasma breakdown and the Formation phase; 3) End of the Formation phase and beginning of the Sustainment phase; 4) Firing of the crowbar, beginning of the current reversal, and destruction of the plasma by setting the cross-field voltage to zero. The horizontal axis is time in microseconds. The signs of the voltage and current have been changed for clarity. These different phases are described in detail in section 5.1.

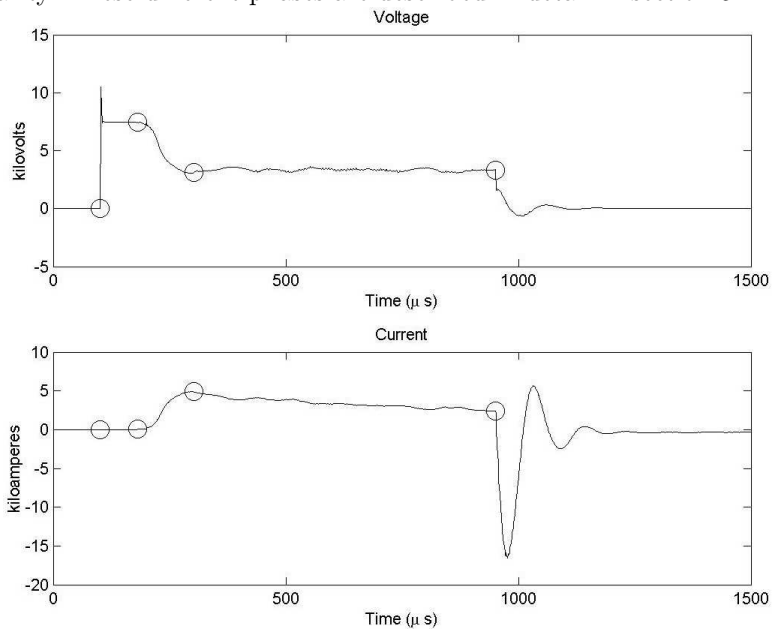

experiment. A comparison of the shots' I and V traces *before* the crowbar's introduction shows they are very reproducible. (Changing the time at which the crowbar is fired while keeping other parameters the same is called a "crowbar scan," and allows measurement of changes in the plasma density with time.)

4.1.1 Rotational Velocity from Measured Voltage

The rotational velocity of the plasma may be estimated by calculating $\frac{V}{aB}$, where a is the plasma width [1], here assumed to be 0.21 meters. This gives a result comparable to the spectroscopically-measured velocity. $\frac{V}{aB}$ is typically on the order of 70 km/s, significantly faster than the 54 km/s thermal velocity of protons at a temperature of 30 eV.

4.1.2 Ion Density from Current Reversal

If a crowbar is applied so as to short the inner electrode to the outer vessel, the plasma drives a current through this short. (See section 5.1.4.) Integrating this reversed-current pulse yields a measurement of the total charge Q stored by the plasma just before the crowbar. That, combined with the last pre-crowbar voltage measurement $V_{crowbar}$ allows a measurement of the plasma's stored electrostatic energy $U = \frac{1}{2}QV_{crowbar}$ [1]. The velocity and the result that the electrostatic energy is stored in the form of rotation gives a measurement of the mass of the rotating plasma and thus the ion density, typically $\sim 10^{20}\mathrm{m}^{-3}$. (Sections 5.1.4, and F.2.1) This calculation does require a good estimate of the plasma geometry.

4.1.3 Neutral Density from RC Time

The neutral density may be estimated by assuming any one of several different loss rates are equal to the charge-exchange rate. Since charge exchange is expected to be the dominant mechanism of momentum loss and of charge diffusion across the plasma, upper limits on the neutral density n_0 may be obtained from the charge-exchange cross-section and the RC time for plasma decay (with resistance R measured just before the crowbar and capacitance C based on the voltage just before the crowbar and the charge dumped during the current reversal). See section F.2.2 for details on this calculation.

4.1.4 Confinement Times from Spectroscopic and Circuit Data

Since the power supplied by the capacitor bank drives cross-field currents which heat the plasma, the IV traces also allow a calculation of the thermal energy confinement time from the ratio of the plasma temperature to the input $I \cdot V$ power. (See section G.3.) Since the energy confinement time is the ratio of the thermal energy to the rate at which thermal energy is lost, we may write for a plasma volume $\mathcal{V}$,

$$\tau_E = \frac{(3n_e kT_e + 3n_i kT_i)\mathcal{V}}{2\langle IV \rangle} \tag{4.1}$$

$$\tau_E \sim \frac{3n_i k\langle T_i \rangle \mathcal{V}}{\langle IV \rangle} \tag{4.2}$$

Here we have assumed $n_e \approx n_i$ and $T_e \sim T_i$, and assumed that all input power becomes thermal energy, (i.e. Ohmic heating).

The momentum confinement time is calculated by comparing the plasma momentum (from velocity and mass [1]) to the input power - see below. Since plasma heating is expected to be due primarily to viscosity, the input power drives both rotation and heating without being divided between them, although an improved model would consider the finite rate at which momentum is converted to thermal energy as well as non-viscous momentum losses.

$$\tau_M \approx \frac{p}{\dot{p}} = \frac{mv_\phi}{m\dot{v}_\phi} \tag{4.3}$$

$$\tau_M \approx \frac{mv_\phi^2}{\partial_t(\frac{m}{2}v_\phi^2)} \tag{4.4}$$

$$\tau_M \approx \frac{mv_\phi^2}{P} = \frac{n_i m_i \mathcal{V} v_\phi^2}{IV} \tag{4.5}$$

To put τ_M in terms of directly-measurable quantities, we note that the models we have been using have $\frac{1}{2}m_i n_i v_\phi^2 \mathcal{V} = \frac{1}{2}QV$:

$$\tau_M \approx \frac{Q\langle V \rangle}{\langle IV \rangle} \approx \frac{Q}{I} \tag{4.6}$$

where we assume the voltage used in the numerator will be averaged over the same period as the power in the denominator. Since we have defined $R = \frac{V}{I}$ and $C = \frac{Q}{V}$, when V and I are approximately constant, we may also write the following:

$$\tau_M \approx \langle \frac{V}{I} \rangle \frac{Q}{\langle V \rangle} = RC \tag{4.7}$$

(See also sections D.4 and G.4. In this dissertation, we will often calculate τ_M using the average velocity from the various emission lines and equation 4.5. For purely-circuit analysis, we will use τ_{RC} to denote the RC time, which also gives an estimate of the momentum confinement time, as shown above. The estimate of τ_M from spectroscopic data is typically a factor of four lower than τ_{RC}.)

4.2 Interpretation of Doppler Spectroscopy

We measure the velocity and ion temperature of the plasma at a single radius via the Doppler shift and broadening of carbon ion emission lines. We use the velocity of the highest-ionized state to estimate the velocity along the line of sight and thus $v_{\phi max}$. Less-ionized states have consistently shown lower velocities, and this is taken to indicate radial stratification of the plasma because the outer regions are expected to be both cooler and slower (section E.1.1). The lower observed velocities are likely due to some combination of a velocity profile and of integration over different radii. Details of this model and estimates of these effects can be found in appendices B and E. The spectroscopy shows Gaussian emission line-shapes which are separated from their zero-velocity positions by more than the line width, indicating supersonic rotation. The line width is dominated by Doppler broadening due to the plasma's temperature, and so a measurement of the line width gives the ion thermal velocity and the temperature of the ion species. We assume that the hydrogen plasma has the same temperature and velocity as the ion species directly observed. Different species give different velocities and temperatures, since different species will exist at different temperatures, and the spectrometer observes light coming from multiple regions. (See figure 4.2.) We generally work in terms of the highest-observed T_i and v_ϕ, which are expected to correspond to the deepest, fastest, and hottest portions of the plasma.

The calculations to deconvolve the effects of integrating over the double-cone in the presence of a stratified plasma are rather complex, and are beyond the scope of this work

4.3 Interpretation of $\dot{\mathbf{B}}$ Traces

Six $\dot{\mathbf{B}}$ probes have been attached to the machine and are used to measure changes in magnetic flux. They reinforce the picture of rotating plasmas and the phases of the discharge described in section 5.1. Visible in some of the $\dot{\mathbf{B}}$ data is an m=1 disturbance which is rotating with the plasma [3]. Since the velocities measured by the $\dot{\mathbf{B}}$ probes are lower than but on the order of velocities derived from spectroscopic measurements, and the $\dot{\mathbf{B}}$ probes are located near the

Figure 4.3: Source Geometry for Spectroscopy: The plasma (dark region) has a cylindrical cross-section, but the light collected by the spectrometer comes from a double-cone region which includes plasma from several radii and directions of rotation. The component of velocity measured by the spectroscopic system is that moving towards or away from the cones' shared vertex. The opening angle of the double-cone is exaggerated for clarity.

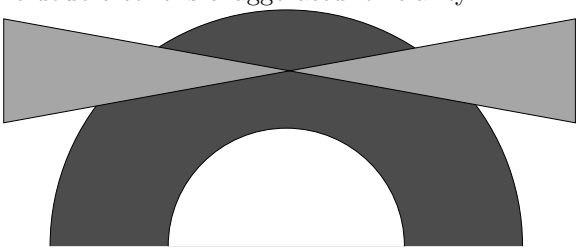

Figure 4.4: Magnetic Probe Positions: Each $\dot{\mathbf{B}}$ probe consists of three coils of conducting wire oriented at right angles to each other. The coils are located inside the tips of the probes at the positions shown.

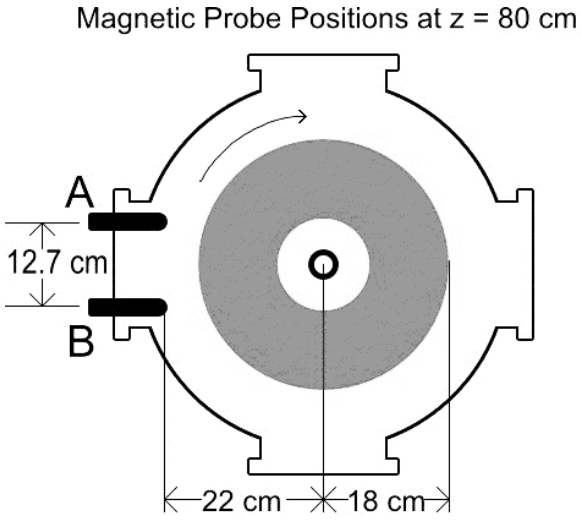

vessel wall while the spectrometer is focused halfway between the core and the wall, the $\dot{\mathbf{B}}$ data also provide some evidence for velocity shear and no-slip boundary conditions. In addition, the $\dot{\mathbf{B}}$ probes provide a rough estimate of the plasma diamagnetism. Finally, changes in the $\dot{\mathbf{B}}$ data correlate well with changes in the current and voltage characteristics corresponding to the different parts of the discharge described in chapter 5.

4.4 Expected Uncertainties

In this section, we estimate the dominant sources of error in the analysis of the MCX plasma. In general, there are four types of uncertainty in analyzing trends within the plasma, arranged here in order of increasing influence on MCX. The cumulative effects of these errors for several sample measurements are given in table 4.1.

Instrumental uncertainty

Any measurement has some finite resolution limited, for example, by the digitizer recording the measurement. Since MCX digitizers have 12-bit precision and reach full-scale at ± 5 Volts, the instrumental resolution is about 2.4 mV. Since the core voltage measurement is made through a 2390:1 voltage divider network, this gives a resolution on the measurement of the core electrode's voltage of 5.8 Volts. For a typical voltage measurement of 2600 V during the sustainment phase of the plasma discharge, (section 5.1.3) this gives an instrumental uncertainty in the voltage measurement of about 0.22%. Since the voltage measurement is typically done as an average over 100 or more individual samples, the instrumental uncertainty is further lowered, to 0.022%.

Calibration error

There are also uncertainties in the calibration of the voltage dividers, digitizers, and other equipment used to take measurements. These calibration errors affect data from different runs identically, so although the absolute values of individual measurements are in doubt, the differences between measurements are valid. As an example, the voltage divider used to measure the core (or load) voltage contains 10 resistors which have individual precisions of $\pm 5\%$, giving an overall calibration uncertainty of about $5/\sqrt{10}\% = 1.6\%$.

Natural variation

Plasmas are inherently chaotic, with a wide variety of wave modes that couple nonlinearly to each other, and to initial and boundary conditions. Because of this, it is rarely useful to rely on individual snapshots of bulk behavior. Instead, the bulk properties measured in MCX are averaged over 100 - 200 data points within each data run, and several runs are made at each point in parameter space. The many samples contributing to each of the voltage measurements quoted in this dissertation allow us to work in terms of the average rotation velocity (from $v_\phi = \frac{V}{aB}$) without worrying about these rapid variations. These oscillations introduce an uncertainty in the average voltage of about 2.4 V (0.13%) for a typical shot. (For this example we used run number mcx030505-5, with an average voltage of 1800 V.)

A larger contributor to natural variation is the differences among multiple runs at identical external conditions. To measure these differences, each data point in this dissertation comes from a set of at least three shots for which external parameters such as fill pressure and applied magnetic field and initial voltage are the same within measurement error. Continuing with our typical shot, we note that for the triplet including mcx030505-5, the standard deviation of the load voltage measurements is 720 V, or 27% of the average voltage, 2600 V.

Interpretive error

By far the largest contribution to the uncertainty in MCX's derived quantities comes from assumptions we make about the plasma dimensions and profiles. The calculations presented here assume the plasma occupies a cylindrical shell 1.4 meters long with an inner radius of 6 cm and an outer radius of 27 cm. All of these dimensions are estimated from vacuum plots of the magnetic field like that shown in figure 3.2. Variations in these boundaries may change the measured densities and velocities by large amounts, as shown in table 4.1.

Measurements of the stored charge are complicated by the presence of the leakage resistance, inductances in the plasma and cabling, changes in the plasma characteristics during the current reversal, and as-yet unexplained shifts in the voltage corresponding to zero current. Resolving these issues may change the measured charge Q by as much as a factor of two in either direction.

The spectroscopic measurements also face some interpretive uncertainty since the spectrometer integrates light coming from a large region of plasma with non-uniform temperature and velocity.

Calculations of bulk density and average velocity are further complicated by possible voltage

drops and variations in density and velocity. Radial variations in plasma characteristics may shift these derived quantities by a factor of two or more. Further information on the effects of profiles may be found in section H.2. Comments on future diagnostics which should help to resolve profile uncertainties can be found in chapter 6.

Table 4.1: Estimated uncertainties: This table shows the estimated errors in a number of quantities central to MCX, starting with the direct measurements and finishing with several derived quantities. None of the figures in this table include contributions from shot-to-shot variation or contributions from velocity and density gradients, although they do include instrumental and calibration errors as well as natural variations within a single run. Quantities marked with an asterisk (*) consider uncertainties in the plasma dimensions. Those marked with a dagger (†) consider interpretive uncertainties in the stored charge, Q.

Quantity	Measurement	Uncertainty	Units
Spectroscopic v_ϕ	110	±5	km/s
Spectroscopic T_i	50	±10	eV
Fill Pressure	5	±0.5	mTorr
Average Core Voltage	2600	±1.6%	Volts
Midplane Field	2000	±12%	Gauss
Mirror Field	18700	±3%	Gauss
Current just before crowbar	1670	±8%	Amps
Plasma i.r. at Midplane r_i	0.06	+0.01 / -0.035	meters
Plasma o.r. at Midplane r_o	0.27	+0.005 / -0.1	meters
Plasma Width at Midplane a	0.21	+0.04/-0.1	meters
Plasma Length L	1.4	+1.2/-0.7	meters
Stored Charge Q	0.49	±8%	Coulombs
Stored Charge $Q^\dagger$	0.49	+ 100% / - 51%	Coulombs
Plasma Volume $\mathcal{V}^*$	0.30	+0.26 / -0.28	m^3
$v_\phi = \frac{V}{aB}$	71	±12%	km/s
$v_\phi^* = \frac{V}{aB}$	71	+110% -36%	km/s
Ion density n_i	6.5×10^{20}	±25%	m^{-3}
Ion density n_i^*	6.5×10^{20}	+280% / -76%	m^{-3}
Ion density $n_i^{*\dagger}$	6.5×10^{20}	+650% / -88%	m^{-3}

Chapter 5: MCX Plasma Behavior

In this chapter we give an overview of the salient trends in the data obtained from our experiment. Although some qualitative explanations are included, the emphasis here is on experimental observations. We begin with a description of the major parts of a typical shot and follow with a more quantitative analysis of how the various features and measurable quantities depend on the parameters we can directly control, such as the magnetic field and the initial capacitor bank voltage.

5.1 Phases of MCX Plasma Evolution

A typical MCX discharge can be qualitatively divided into four phases, beginning when the start ignitron is fired: *holdoff, formation, sustainment*, and *current reversal*. (See figure 4.1 for a plot of typical current and voltage traces and figure 4.1 to see the locations of the ignitrons, capacitor bank, and vacuum vessel.) If the crowbar is not fired, or if it is delayed too long, a *quenching* phase results instead. A more fine-scale, quantitative assessment of how the measured quantities vary with time is given in section 5.2.7.

5.1.1 Holdoff Phase

Plasma activity is possible only after the start ignitron is fired, connecting the core electrode to the capacitor bank and providing the source of energy necessary to ionizing the hydrogen gas which fills the chamber. Within 2 μs of the ignitron's firing, the central electrode reaches a voltage approximately equal to that of the capacitor bank. This begins the *holdoff phase*. During the holdoff phase, the $\dot{\mathbf{B}}$ probes show magnetic quiescence, no current flows, and the voltage across the machine holds steady at the full voltage of the capacitor bank. This phase usually lasts between 50 and 400 μs. The length of time the machine remains at this high voltage varies inversely with applied voltage, inversely with fill pressure and directly with the midplane magnetic field. This fits with the concept of *magnetic insulation*, which implies the development of large cross-field currents should be suppressed by strong B fields' reduction of the Larmor radius and corresponding increase in confinement.

5.1.2 Formation Phase

The boundary between the holdoff phase and the formation phase is taken to be the time at which the current first differs substantially from zero. The formation phase is characterized by a rapidly rising current, fast high-amplitude $\dot{\mathbf{B}}$ probe activity, and a sudden drop in voltage, typically lasting 60 - 260 microseconds. Current data indicate that this represents a transition between neutral-dominated and MHD regimes. A large portion of the input power is expected to be used in ionization of the fill gas (hydrogen), and in ejection of carbon, oxygen, and other impurities from the insulators and vessel walls. Power is also be spent heating the insulators and in accelerating the electrons and ions to the $E \times B$ velocity.

5.1.3 Sustainment Phase

The third and longest phase is the sustainment. During this period, which may last several milliseconds, the voltage across the plasma remains relatively constant (but slowly decaying) at a level of around three kilovolts for standard input parameters. (These are: midplane magnetic field = 0.2 T, fill pressure = 5 mTorr, mirror ratio 9, and -7 kV initial capacitor bank voltage. For general trends in the sustainment voltage, see section 5.2 and appendix I) The current decays quasi-exponentially as the radial impedance of the plasma grows from a typical 0.5 Ω to around 2 Ω. The early part of the sustainment period will often show a flat, step-like feature in the load current which interrupts the decay. $\dot{\mathbf{B}}$ probe data (section 4.3) indicate that this is actually a separate phase during the transition between the formation and sustainment phases, since there is a brief decrease in magnetic activity between the formation and sustainment phases, then high magnetic fluctuations continues for the first part of the sustainment phase, until low-level, more regular magnetic oscillations emerge in the later part of the sustainment phase. In figure 5.14 we plot the power versus time.

Oscillatory Behavior

Middle to late portions of the sustainment often show quasi-periodic disturbances - triangular or square waves superimposed on the voltage and current traces. The periods of the voltage and current oscillations average about 100 us, and amplitudes vary as the discharge progresses. Although several shots made in rapid succession with the same input conditions often yield nearly-identical current and voltage histories, shots made on different days may vary substantially in the sustained voltage, the length or presence of the constant-current step near the beginning of the discharge, and the shape, period, and amplitude of the periodic

disturbances. It should be noted that the periodicity is probably *not* tied to rotation, since a plasma body moving at the typically-measured 50 - 100 km/s is expected to make a complete circuit of the machine in only a few tens of microseconds. (These times are, however, comparable to the fluctuations seen in the $\dot{\mathbf{B}}$ data.) Similarly, oscillations dependent on waves bouncing between the two magnetic mirrors are expected to present fluctuations around an order of magnitude faster than those seen. The triangular waveforms suggest a change in global plasma conditions, perhaps due to an oscillating rotational velocity [3].

Boundary Between Formation and Sustainment Phases

For the purposes of comparison between different runs, the beginning of the sustainment phase is defined to be the time at which the plasma current reaches its maximum. The maximum current attained depends on the magnetic field as shown in figure 5.12. It should be noted that this definition for the boundary time between the formation and sustainment phases is made largely for convenience. The ion density as determined by the current reversal (section 5.1.4) does not peak until roughly 500 μs after the current peak, and data from the $\dot{\mathbf{B}}$ probes shows qualitative changes at several points during what we here refer to as the sustainment phase. The full analysis of the magnetic data is beyond the scope of this work. See section 5.2.7 for more detailed information on the evolution of the plasma over the course of a shot and section 4.3 for more on the magnetic probe data. The cross-field voltage and power input during the sustainment phase provide strong evidence for rotation and a high degree of ionization. (See sections 4.1.1 and 4.1.3.)

5.1.4 Current Reversal

The final phase of interest for most discharges is the current reversal which results when the plasma is crowbarred. (Opening the circuit gives somewhat different results from the crowbar - see sections 6.3 and A.5.2.) When the crowbar connects the high-voltage side of the machine and the capacitor bank to ground, the system suddenly dumps all the stored charge to ground, resulting in a large-amplitude ringing with a period of around 100 μs. The comparison of the measured stored charge with the cross-field voltage just before the crowbar yields an estimate of the ion density. (See also sections 4.1.2 and F.2.1.) The $\dot{\mathbf{B}}$ probes often show substantial magnetic fluctuations for up to about 100 μs after the crowbar is closed. The dependence of the magnitude of the current reversal on the magnetic field is demonstrated in figure 5.12. The current reversal is the primary evidence for ion densities comparable to $10^{20}\mathrm{m}^{-3}$.

5.1.5 Quenching

A feature sometimes evident at the end of the sustainment period is a final load-voltage "pedestal" which seems to signal the extinction of the plasma. This pedestal is rarely present before 2 ms (at which point the crowbar is closed in most of our data runs), and seems to result when the input current falls below some critical value. Sometimes the pedestal appears as an electrical short across the machine but more often it appears as a slight *increase* in the load voltage and an end to fluctuations - apparently the ionization fraction has dropped low enough that the plasma body no longer conducts a significant amount of current and the voltage is too low to yield another breakdown. If the plasma was not shorted by the crowbar, the voltage decay rate leading into the pedestal gives a measure of the momentum confinement time of the plasma. (See section G.4.) When quenching occurs, the $\dot{\mathbf{B}}$ probes show a lack of magnetic activity consistent with an absence of plasma.

5.2 Parametric Dependencies

This section reports phenomenological correlations between the various directly-controllable parameters and the measured plasma characteristics. The emphasis is on reporting experimentally-observed trends, and only the most general comparison to theory is given. The best-fit equations are given in appendix I.

Each section below gives the range of the input parameters used, as well as notes on particularly clear or confusing trends. Each scan was along a different axis in parameter space with the intersection approximately at -7 kV, 5 mTorr hydrogen, 0.2 Tesla at the midplane, a mirror ratio of 9, and a crowbar at 1.6 ms.

5.2.1 Dependence on the Sign of the Applied Voltage

The voltage applied to the core may be either positive or negative (section A.5.3), although it is most common to run MCX with the core negative. Although the phases described above (section 5.1) are observed both when the core is the anode and when it is the cathode, core-positive discharges have more pronounced humps in current and voltage just after the formation phase. (See figure 5.1.) There is also some evidence to indicate that core-positive shots have large voltage oscillations during their sustainment phase and cause more mechanical damage to the machine than do negative shots, but there is as yet little data for a detailed comparison between positive and negative shots. Lehnert [20, Lehnert's section 2.9.2] hypothesizes that the neutral drag instability should be more powerful when the core is

Figure 5.1: Voltage and Current Traces for Positive and Negative Shots: The above figure shows the behavior of the plasma voltage (top) and current (bottom) during two shots at 0.2 T midplane field, mirror ratio 9, and 5 mTorr from October 30 (+7 kV), and October 31, 2002 (-7 kV). The solid curve in each plot shows the core-positive discharge while the dashed curve shows the core-negative discharge. Note a sharp depression and pronounced hump are visible in the core-positive voltage trace but not the core-negative voltage. Similar differences are visible on the current traces. While small, these differences are strongly correlated with the sign of the applied voltage for the small number of shots examined. In each case, the crowbar was closed at 2000 μs.

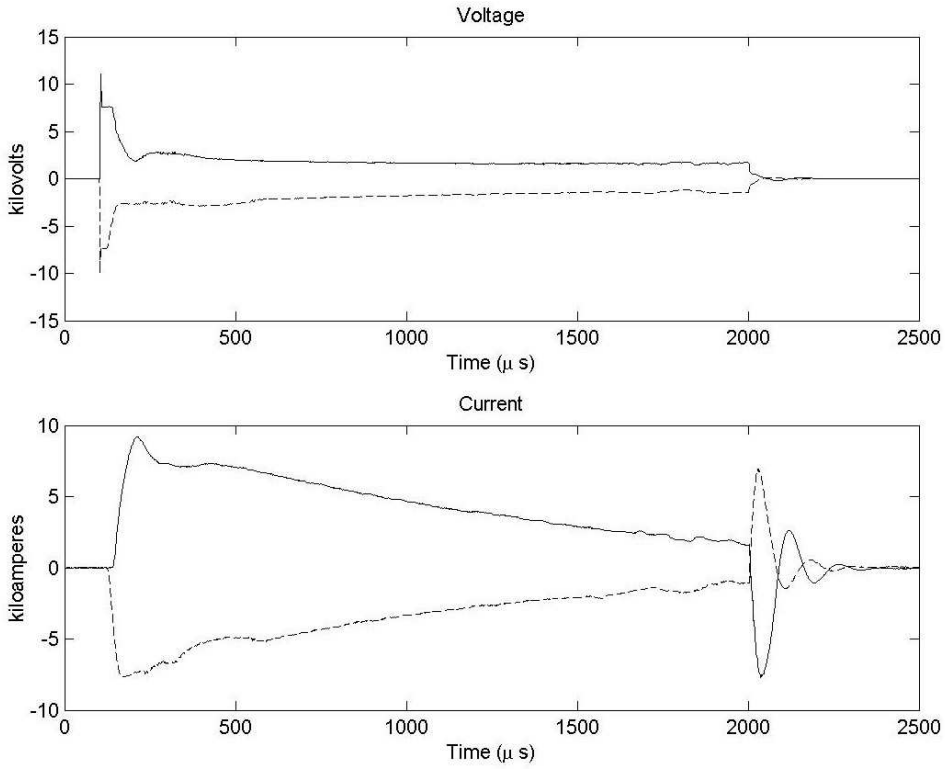

negative. It has also been noted that in the formation phase under the core-negative configuration, the combined geometry of the electric and magnetic fields means the electrons will be accelerated away from the insulators toward the midplane, presumably leading to more efficient startup than in the core-positive configuration, for which the imposed electric field tends to accelerate electrons out of the plasma volume during startup.

5.2.2 Dependence on Magnitude of the Initial Voltage

General Notes

Table I.1 shows the experimental dependencies of several parameters on the magnitude of the initial capacitor bank voltage V_0. The data set used to build this table consists of 21 shots taken at 2 kG on midplane and a mirror ratio of 9. The bank voltage was raised from -5 kV to -8 kV in 500 Volt steps with a crowbar at 1.6 ms and a fill pressure of 5 mTorr hydrogen.

Observed Trends

- Both the overall sustainment power $P_{sustainment}$ and the power at late times ($P_{1.6ms}$ at 1.6 ms) steadily increased as $|V_0|$ increased, due in part to
- increases in current (as shown by I_{1ms} and $I_{forward}$), although
- the current at late times ($|I_{1.6ms}|$) shows a definite minimal magnitude near $|-1.3|$ kA at -6 kV.
- $|V_{sustainment}|$ peaks at about 3.3 kV for $V_0 \approx -7$ kV.
- The maximum sustainment impedance is $Z_{sustainment} \approx 1.8\Omega$ near V_0 = -6 kV.

As might be expected,

- the voltage $V_{holdoff}$ present across the machine before current starts to flow is approximately equal to the charge voltage V_0, and
- the time $t_{holdoff}$ required for breakdown to begin decreases as the magnitude of the voltage increases.
- The time $t_{formation}$ required for the formation phase also decreases, implying that at high voltages, the plasma is moved to its steady-state configuration more quickly, although since
- there are minima in $U_{formation}$ (the energy expended during the formation phase) and $Q_{formation}$ (the integrated current during the formation phase) of approximately 1200 J and 0.3 C near V_0 = -7.5 kV, faster transitions are not necessarily more efficient.

We also note that near V_0 = -6.5 kV,

- the stored charge $Q_{reversed}$ peaks around 0.45 C,

Figure 5.2: Ion Density vs. Initial Capacitor Voltage: The ion density as calculated from the stored electrostatic energy and the $\frac{V}{aB}$ rotation speed. The equation for the fitted curve may be found in table I.1, and the calculation is described in section F.2.1.

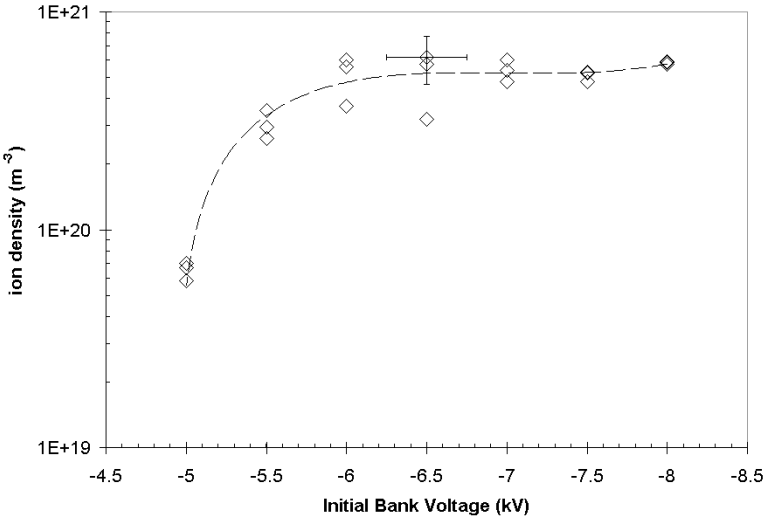

- the inferred ion density n_i reaches a maximum of about $5 \times 10^{20}\mathrm{m}^{-3}$ (see figure 5.2.2,
- $I_{reversed}$ peaks about 15 kA, and
- the neutral density n_0 reaches a minimum of about $10^{17}\mathrm{m}^{-3}$.

5.2.3 Dependence on Initial Fill Pressure

General Notes

Shots were taken at hydrogen fill pressures of approximately 3, 5, 7.5, 10.5, 13, 16, and 21 mTorr. The other input parameters were held constant at -7 kV initial bank voltage, 0.2 T magnetic field at the midplane, mirror ratio 9, and 1.6 ms crowbar. In general, the effect of the fill pressure on the performance of the MCX plasma seems rather weak. Those observed are listed in table I.2.

Observed Trends

- The power drawn by the plasma slowly decreases as P_{fill} increases, both as averaged over the full sustainment phase ($P_{sustainment}$) and in the last 100μs before the crowbar ($P_{1.6ms}$).
- The magnitudes of the voltages V_{1ms}, and $V_{1.6ms}$ also slowly decrease, but

- the maximum forward current $I_{forward}$ shows a slight increase with pressure.
- There is a corresponding decrease in the impedances Z_{1ms} and $Z_{sustainment}$.
- The rapid decrease of the holdoff time $t_{holdoff}$ as the P_{fill} increases is by far the strongest dependence of any measured parameter on the fill pressure.
- It is worrisome that the fill pressure has virtually no influence on the inferred ion density n_i, and that
- the neutral density $n_{0,G\&R}$ predicted by the diffusion model (section F.3) depends very strongly on fill pressure but the inferred neutral density, $n_{0,RC}$ does not.

These last two points may imply either a significant contribution from high-mass impurities, a complex ionization mechanism, or heat-driven out-gassing from the walls. The ion densities described herein are compatible with initial interferometer measurements and estimates from the fill pressure. (See sections F.3 and 6.2 and Table 4.1.)

5.2.4 Dependence on Mirror Ratio

General Notes

Theoretical considerations imply that MCX's mirror ratio should have a significant effect on the plasma. First, $\mathcal{R}$ governs the mirror loss cone in the non-rotating case, and is expected to play an important role in ion end losses when the rotational velocity v_ϕ is not much larger than the thermal speed v_{Ti}. Second, changes in $\mathcal{R}$ imply changes in the plasma geometry, including the aspect ratio and the position of the strike point of the last good flux surface on the outer wall of the vessel.

A discussion of the effects of $\mathcal{R}$ on MCX necessitates the concept of a "good flux surface". The frozen-in theorem (section C.1.2) demands that contiguous areas with high conductivity move together. Thus areas where the plasma touches the stainless steel wall must rotate at the same speed as the vessel, zero. Since electrons move relatively easily through the mirror field (and have sufficiently high thermal velocities that they are not confined by the mechanism described in section 2.3.1), rotation of the plasma requires a material insulator separating the plasma from the vessel walls by crossing the magnetic field line passing through each element of rotating plasma. The flux surfaces which satisfy this requirement are free to rotate and are thus considered "good". Those which are tied to the wall do not satisfy the conditions necessary for centrifugal confinement. See figure 5.3 for a plot of the innermost and outermost good flux surfaces at the different mirror ratios in the $\mathcal{R}$ scan.

Figure 5.3: Magnetic Field Shape Dependence on $\mathcal{R}$: The large dark bar on the left side of the figure shows the position of the stainless steel core, and the thinner horizontal and vertical gray bars show the position of the insulators. The curves of varying shade show the innermost and outermost "good flux surfaces" for mirror ratios 3, 5, 7, 9 , 11, 13, 15, and 17, with the lower mirror ratios corresponding to darker curves and the higher $\mathcal{R}$ being described by the lighter curves. For a description of what constitutes a "good flux surface", see the text in section 5.2.4. The scales in the above figure are in centimeters. For the volumes enclosed by the good flux surfaces, see table H.1.

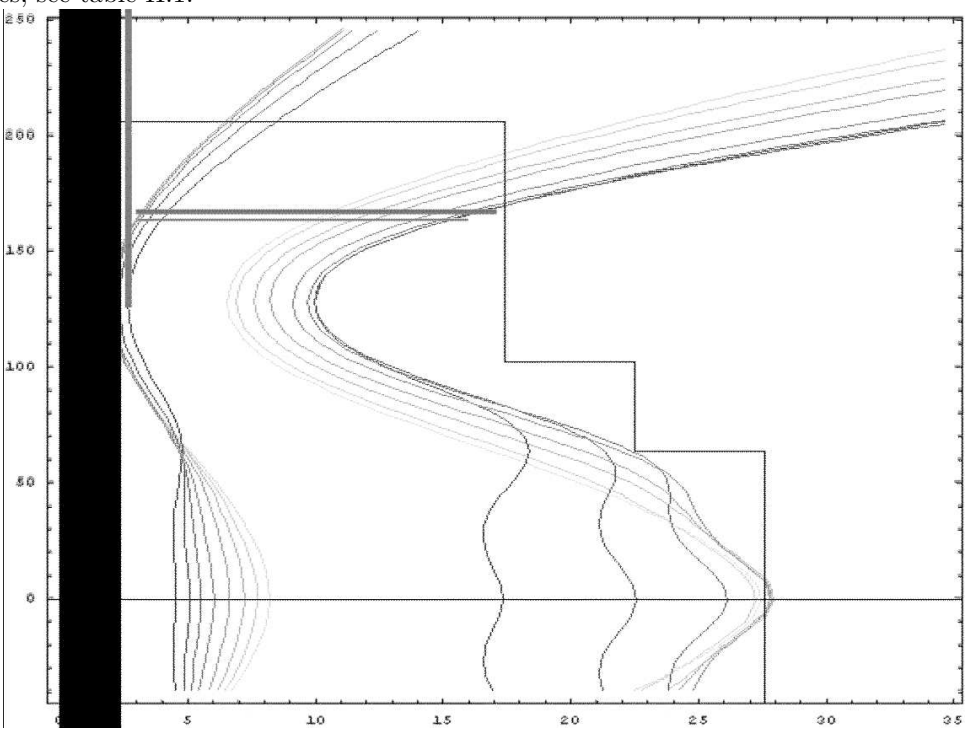

Figure 5.4: Temperature vs. Mirror Ratio: The diamonds mark the average temperature of all observed carbon emission lines; the circles show the temperature of the line with the highest Doppler shift. This scan was done for a magnetic field of 1 kG at the midplane and a fill pressure of 5 mTorr. Error bars are shown for two representative points.

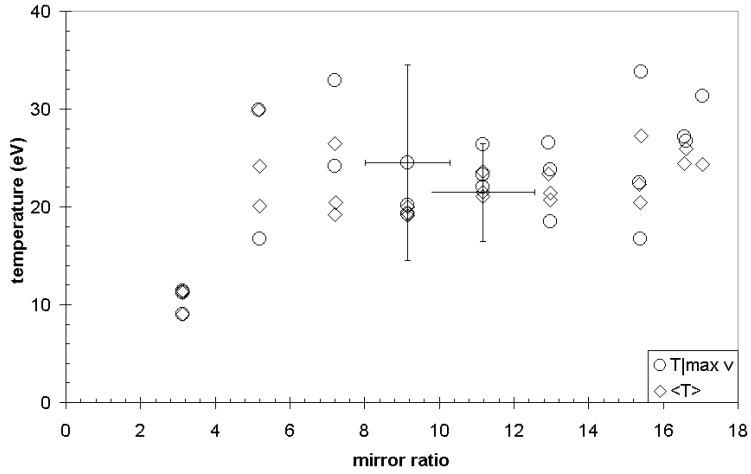

To find the dependencies of these quantities on mirror ratio, $\mathcal{R}$ was scanned over odd values from 3 to 17 in a total of 24 shots, while the magnetic field at the midplane was held at 0.1 Tesla and the hydrogen fill pressure was kept at 5 mTorr. Many of the measured parameters change monotonically for $\mathcal{R} \leq 9$, then are approximately constant or only slowly varying for $\mathcal{R} \geq 9$. (See for example, figures 5.2.4, 5.6, 5.9, and 5.7.) To clarify the cause of this trend, we superimposed calculations of the magnetic flux surfaces on a diagram of the machine for the different mirror ratios corresponding to the scan in $\mathcal{R}$. One striking result of that comparison is that the plasma width increases steadily as the strike point of the last good flux surface moves from near the mirror maximum to the midplane - at $\mathcal{R} \approx 9$, after which the geometry changes relatively little as the mirror ratio continues to increase. That many MCX plasma parameters respond strongly to $\mathcal{R} \lesssim 9$ and are almost independent of it for $\mathcal{R} \gtrsim 9$ suggests that most of the plasma is localized near the machine midplane, that the flux surfaces in the plasma are similar to the vacuum field calculations, and that the plasma is rotating in a manner consistent with the physical assumptions and approximations we have made previously. The most well-defined trends in the data are outlined in the following paragraphs, in table I.3, and in figure 5.7.

Observed Trends

- The reversal current $I_{reversed}$ increases steadily with $\mathcal{R}$, saturating when $\mathcal{R} \approx 9$ at about 7 kA.

Figure 5.5: Energy Confinement Time vs. Mirror Ratio: The energy confinement time is given in μs. Some variation may be due to changes in the plasma between the time of the spectroscopy measurement and that of the crowbar (density measurement), but most is due to the shot-to-shot variations in temperature. (See figure 5.4.) The (thermal) energy confinement time is defined in section 4.1.4. Error bars are shown for a typical point.

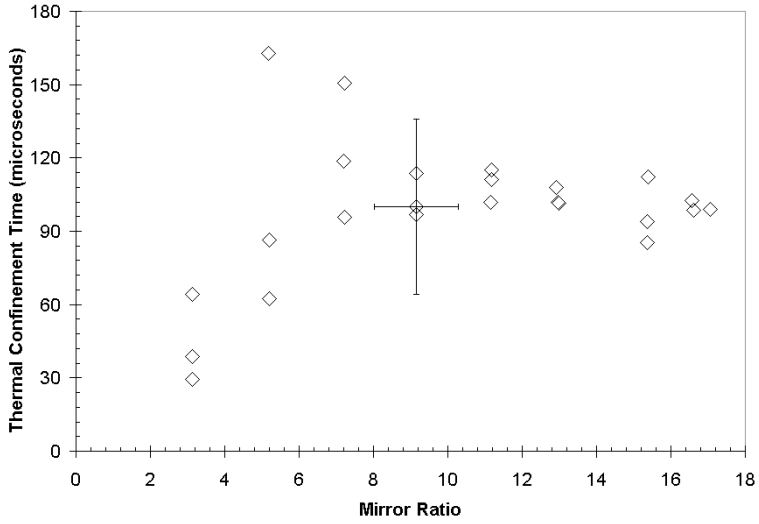

- The recovered charge $Q_{reversed}$ likewise increases to a flat-top of about 0.37 C.
- The forward current $I_{forward}$, however, decreases in magnitude as $\mathcal{R}$ increases, although it slows substantially once $\mathcal{R} \gtrsim 9$.

These trends imply that as the mirror ratio is increased, the cross-field current ionizes the hydrogen fill gas more efficiently and that fewer ions are lost at $\mathcal{R} \gtrsim 9$:

- The inferred ion density n_i increases to about 3×10^{20} while
- the inferred neutral density n_0 falls to about 1.8×10^{17}.

Both densities reaching their final values near $\mathcal{R} \approx 8$. (See figure 5.7.)

- The average voltage during the sustainment phase, $V_{sustainment}$ increases in magnitude to 1.3 kV, with corresponding increases in V_{1ms} and $V_{1.6ms}$ to about 1.2 kV.
- The $\frac{V}{I}$ impedances $Z_{sustainment}$, $Z_{1.6ms}$, and Z_{1ms} all peak near $\mathcal{R} \approx 9$, but the peak is only strong for $Z_{1.6ms}$, which peaks at about 0.8Ω, then decreases to near 0.7Ω, while the averages near 1 ms and over the full sustainment period peak between 0.35 Ω and 0.4 Ω and decrease only slightly.
- The stored electrostatic energy U increases until $\mathcal{R}$ is approximately 9, at which point $U \approx 240$ J, then decreases slowly with $\mathcal{R}$, presumably because as the mirror ratio

Figure 5.6: Rotation Velocity vs. Mirror Ratio: The figure below plots the speed of the emission line showing the greatest Doppler shift. Table I.3 shows the equation for the fitted curve. Note the changes in slope near mirror ratio 9. Error bars are shown for a typical measurement.

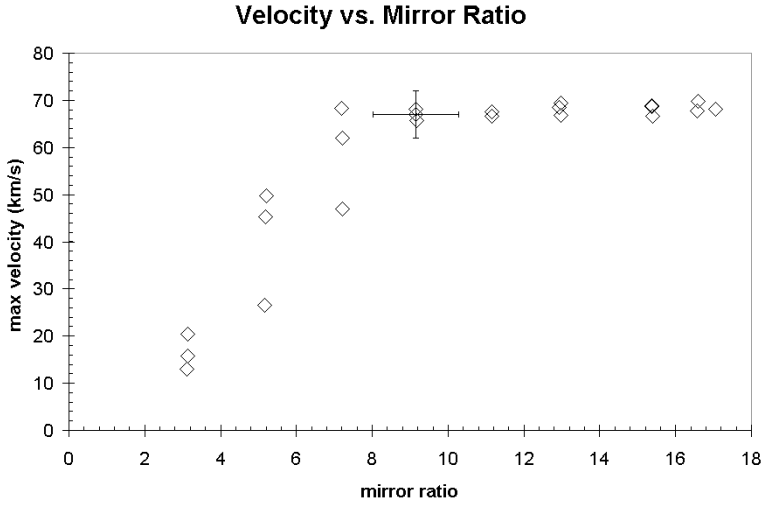

Figure 5.7: Ion and Neutral Densities vs. Mirror Ratio: The ion density, shown by the squares, is calculated from the stored electrostatic energy and the $\frac{V}{aB}$ rotation speed. The neutral density, shown by diamonds, is calculated by assuming that the plasma's RC time just before the crowbar is equal to the plasma's charge-exchange time. The equations for the fitted curve may be found in table I.4, and the calculations are described in sections F.2.1 and F.2.2. Their ratio is plotted as the X's on the right-hand scale. Since the observed neutral density is not well-matched to the best-fit power-law curves, it seems likely that particle confinement and n_0 are dominated by a process other than mirror confinement. The above data are consistent with supersonic rotation, as described in section 5.2.4. Typical error bars are shown for three data points. These neglect uncertainties in the plasma shape, the charge-exchange cross-section, and the interpretation of the reversal current.

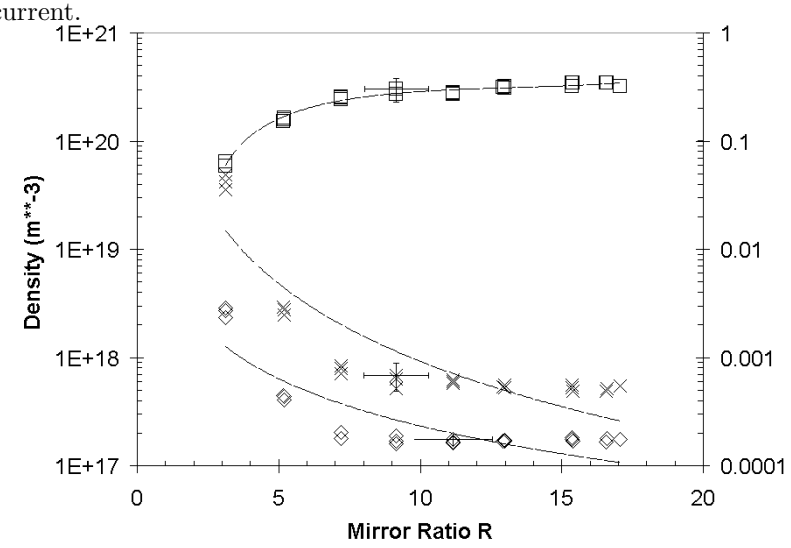

Figure 5.8: Neutral Density Estimates: The diamonds show the neutral density inferred from calculations based on the plasma RC time as described in section F.2.2. The squares show n_0 as calculated from the energy confinement time τ_E and the triangles show n_0 calculated from the momentum confinement time τ_M. Both of these use spectroscopic data and algorithms outlined in section F.2.3. Since all three methods are expected to yield upper limits on n_0, we base most calculations on the RC-based one, which is generally the least of the three. The Goldston and Rutherford particle diffusion model (section F.3) estimates much lower neutral densities. The τ_M was calculated using the mean Doppler shift of the impurity emission lines. Error bars are shown for three typical data points.

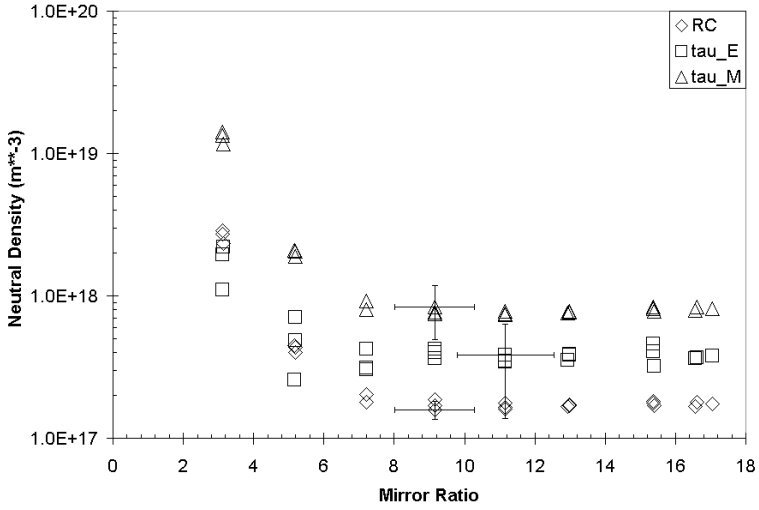

Figure 5.9: Momentum Confinement Time vs. Mirror Ratio: As the mirror ratio increases, the momentum confinement time increases until $\mathcal{R} \approx 10$, at which point τ_M begins to decrease. The calculation is done according to equation 4.5, with $v_\phi = \frac{V}{aB}$. The equation for the fitted curve is given in table I.3 as τ_{RC}. The momentum confinement time might also be calculated with v_ϕ as established by the average Doppler shift from all visible lines, and n_i from the stored energy and the averaged spectroscopy velocity, written as τ_M in appendix I. As with other shots in the scan of $\mathcal{R}$, the crowbar was at 1.6 ms, and the magnetic field at the midplane was fixed at 1 kG. Error bars are shown for a typical data point.

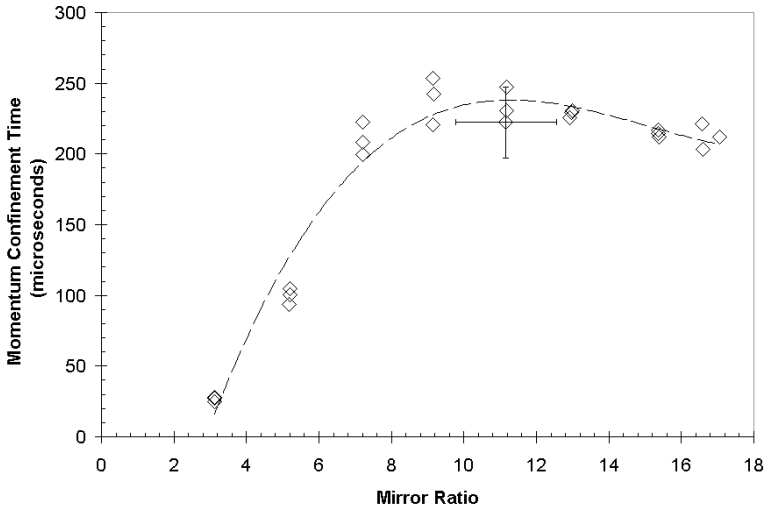

increases past 9, the width of the non-line-tied (and thus rotating) plasma at midplane decreases, so that there is less energy present in the rotation.

- The Alfvén Mach number increases until it is near 0.53 - as calculated from the stored energy and $\frac{V}{aB}$ rotation velocity. (See figure 5.2.4.)
- The RC time τ_{RC} rises quickly to a peak of 240 μs at $\mathcal{R} \approx 9$, then decreases as the mirror ratio increases. For $\mathcal{R} \gtrsim 7$, the RC time is approximately 220 μs.

The above observations are all compatible with the idea that a higher mirror ratio improves both mirror and centrifugal confinement. In contrast,

- the input $V \cdot I$ power rises with $\mathcal{R}$ to a maximum near 6.5 MW, where it stays for $\mathcal{R} \gtrsim 8$ when averaged over the sustainment period ($P_{sustainment}$).
- The average power input between 1.5 and 1.6 ms ($P_{1.6ms}$) shows a similar trend, but only reaches 2 MW.

These two observations seem to contradict the notion that a high mirror ratio provides better confinement.

- We also note the maximum observed Doppler-shift velocity, v_ϕ reaches an apparent upper limit just below 70 km/s.
- One might also expect that if mirror ratio improves confinement, the energy used during formation should be minimal for some mirror ratio. Instead, $U_{formation}$ seems independent of mirror ratio.

All observations indicate a rapid change in plasma behavior near the same mirror ratio, $\mathcal{R} \approx 9$. This is consistent with the concept of good flux surfaces illustrated in figure 5.6.

5.2.5 Dependence on Magnitude of Midplane Magnetic Field

General Notes

The scan in midplane magnetic field consisted of 21 shots from 0.039 T to 0.204 T at seven parameter settings. For the analysis described below and in table I.4, only the 15 shots with $B_{midplane} > 0.08$ Tesla are considered, since those with lower magnetic field are qualitatively different. These are shots mcx030505-4 through mcx030505-18.
Some of the clearer trends are outlined below and in figure 5.12.

Figure 5.10: Mach Number vs. Mirror Ratio: The above figure plots the Mach number as calculated from the emission line showing the most Doppler shift (diamonds) and from the average velocity and temperature of all observed lines (squares). Table I.3 shows the equations for the fitted curves. Note the changes in slope near mirror ratio 9. Note that although the fitted curves imply a maximum near $\mathcal{R} = 13$, the actual data is almost independent of mirror ratio when the latter is greater than 9. The curves differ because the the plasma velocity and temperature vary with radius. Representative error bars are shown for two data points.

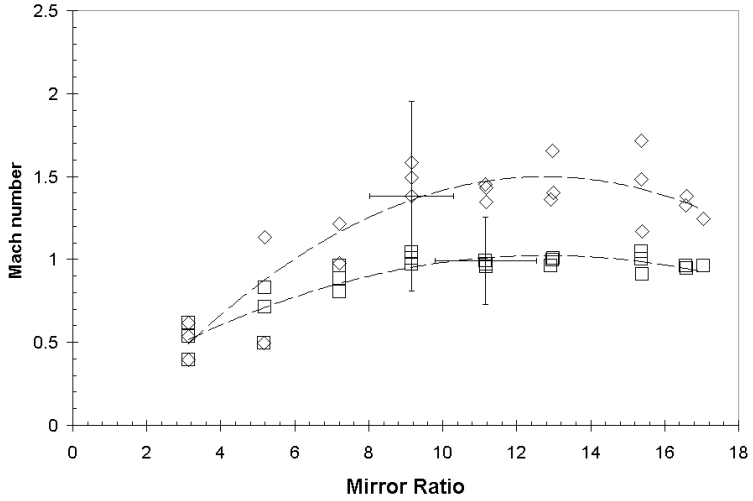

Observed Trends

- The forward (or driving) current $I_{forward}$ decreases as the magnetic field increases while the reversal current $I_{reversed}$ increases.

The above seems to match the view that increasing the magnetic field should reduce transport, enabling the hydrogen to be ionized and driven into rotation with less energy input and trapping more charge on the central electrode. (See figure 5.12.) This view is consistent with the observed steady increase in the ion density n_i. (Figure 5.11)

- As the magnetic field is increased, $t_{holdoff}$, the time required for current to start flowing also increases substantially, even as
- the holdoff voltage $V_{holdoff}$ is increasing.

This implies that the magnetic field is acting as an insulator, making it more difficult for the initial $J_\perp$ to gain strength. The increase in $V_{holdoff}$ may be visualized as the result of a voltage divider composed of the machine and the 0.5Ω series resistance: as it becomes more difficult for current to flow across the machine, a larger fraction of the capacitor bank voltage appears between the core electrode and the vessel's outer wall. Similarly,

Figure 5.11: Ion and Neutral Densities vs. Magnetic Field: The ion density, shown by the diamonds, is calculated from the stored electrostatic energy and the $\frac{V}{aB}$ rotation speed. The neutral density, shown by squares, is calculated by assuming that the plasma's RC time just before the crowbar is equal to the plasma's charge-exchange time. The equations for the fitted curves may be found in table I.4, and the calculations are described in sections F.2.1 and F.2.2. Their ratio is plotted as the X's on the right-hand scale.

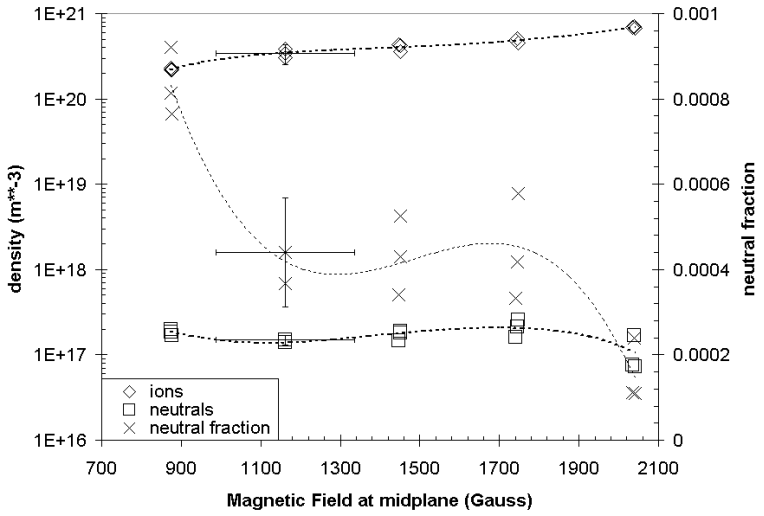

- $V_{sustainment}$, V_{1ms}, and $V_{1.6ms}$ also increase, indicating faster rotation at higher B, presumably because a strong magnetic field inhibits cross-field momentum transport.
- This is compatible with the increase in ion density n_i and decrease in neutral fraction $\frac{n_0}{n_i}$ with magnetic field. (See figure 5.11)
- Contrary to this intuitive model, however, is the steady increase with $B_{midplane}$ of the input power $P_{sustainment}$ and $P_{1.6ms}$ during the sustainment phase:

The cross-field voltage increases faster with B than the current decreases.

5.2.6 Dependence on Direction of Magnetic Field

Switching the direction of the magnetic field should reverse the direction of the plasma rotation (section 1.2), but cause no other changes to the MCX plasma. This prediction has been confirmed by changing the connections between the power supplies and the magnetic field coils (See sections A.3 and A.4.) and taking several data runs under otherwise identical conditions. Spectroscopic and I, V measurements look very similar for both sets of shots, with the exception of the Doppler-shift measurements of the velocity through the top port in the normal B direction. (See figure 3.3.) These measurements gave much lower v_ϕ than either the

Figure 5.12: Plasma Current versus Magnetic Field: In the above diagram, the magnitudes of both the forward and reversed currents have been plotted. Increasing the magnetic field increases the reversal current while decreasing the peak current necessary to form the plasma. This is compatible with the intuitive model that the presence of the magnetic field should reduce cross-field charge transport and improve confinement. For the equations of the fitted curves, see table I.4. Sample error bars are shown for two typical points.

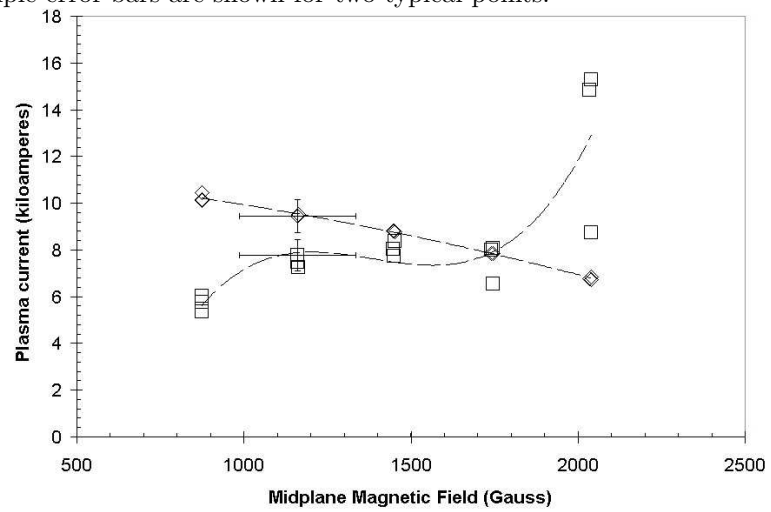

measurements through the bottom port or in the reversed-B configuration. The current and voltage traces show no such anomaly. The data set for direct comparison of the shots' dependence on the direction of the **B** field is very small, consisting of less than a dozen shots from June 16, 2003.

5.2.7 Time-Dependence of Plasma Parameters

We compare the time scales for the plasma development in order to understand which loss mechanisms and wave modes dominate plasma lifetimes and the losses of particles, energy, and momentum. The heat and momentum confinement times reflect the power necessary to maintain centrifugal confinement and thus provide information on how useful a scaled-up version of MCX would be for reactor and materials studies. The many competing time scales have been calculated and listed in table 5.1. Equations fit to the time dependence of measured parameters may be found in table I.5, and descriptions of the qualitatively different phases of the plasma are given in section 5.1. The net result of this analysis is that MCX attains a steady-state condition which is stable for many confinement times and decays away smoothly as the capacitor bank which supplies the cross-field voltage is drained of charge.

Figure 5.13: Ion Density Estimates: The circles mark calculations of the ion density based on the stored electrostatic energy at the crowbar $U_{crowbar}$ and the speed $\frac{V}{aB}$; the triangles are the same calculation using the most Doppler-shifted observed emission line instead. Error bars are shown for a pair of representative points.

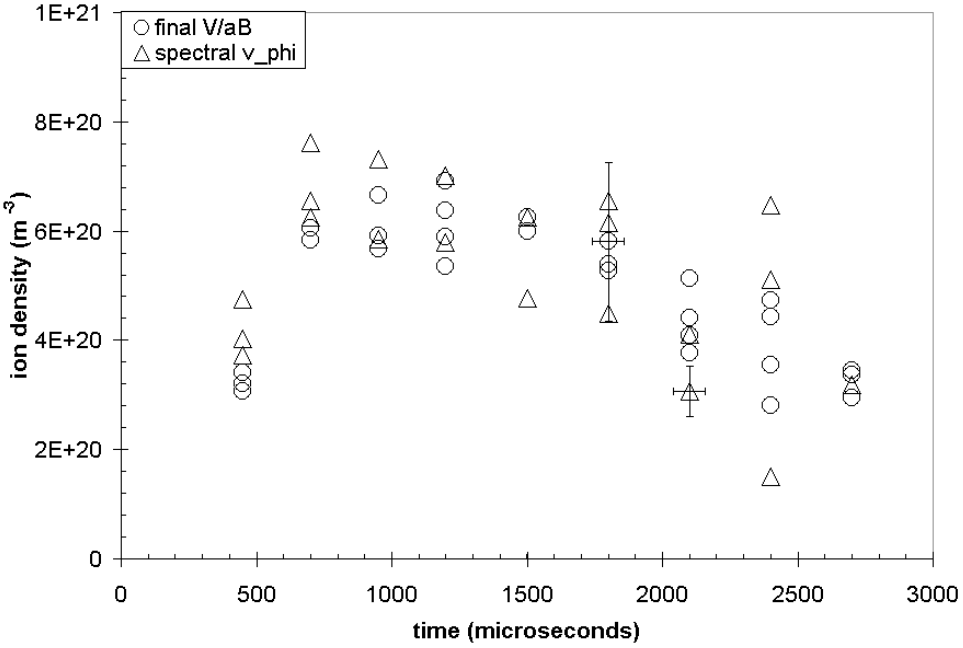

Table 5.1: Typical MCX Time scales: The above times are calculated assuming the following numbers: B = $B_{midplane}$ = 0.2 T, Z = 1, $m_i = m_p$, $n_e = n_i = 10^{20}\mathrm{m}^{-3}$, r_o = 0.27 m, r_i = 0.06 m, a = $r_o - r_i$ = 0.21m, V = 3 kV, $T_e = T_i$ = 30 eV and $\ln\Lambda = 15$. Most of the formulae used are drawn from the NRL Plasma Formulary [18, pp. 28-29] and converted to our units using Jackson's text [19, p. 819]. Additional formulae have been drawn from Chen [4, p. 172, 206]. To calculate the resistance for the bank RC time, we sum a 0.5 Ω series resistor (section A.5.3) with a typical 1 Ω plasma resistance. The plasma RC time given is the average over measurements from the mirror ratio scan with $\mathcal{R} \gtrsim 7$.

Time Scale	Formula	Typical (μs)
electron plasma	$f_{pe}^{-1} = 2\pi\sqrt{\frac{m_e\epsilon_0}{n_e e_0^2}} = \frac{1.11\times10^5}{\sqrt{n_e}}$	1.1×10^{-5}
electron gyroperiod	$f_{ce}^{-1} = \frac{2\pi m_e}{e_0 B} = \frac{3.57\times10^{-5}}{B}$	1.8×10^{-4}
ion plasma	$f_{pi}^{-1} = 2\pi\sqrt{\frac{m_i\epsilon_0}{n_i Z^2 e_0^2}} = \frac{4.77\times10^6}{\sqrt{n_i}}$	4.8×10^{-4}

electron collision	$\tau_e = \nu_e^{-1} = 3.44 \times 10^{17} \frac{T_e^{\frac{3}{2}}}{n_e \ln \Lambda}$	0.038
ion gyroperiod	$f_{ci}^{-1} = \frac{2\pi m_i}{Ze_0 B} = \frac{0.0658}{B}$	0.33
thermal electron transit	$t_{Te} = \frac{L}{v_{Te}} = L\sqrt{\frac{m_e}{kT_e}} = 2.39\frac{L}{\sqrt{T_e}}$	0.61
digitizer sampling		1 μs
ion collision	$\tau_i = \nu_i^{-1} = 2.08 \times 10^{19} \frac{\sqrt{m_i T_i^3}}{Z^4 n_i \sqrt{m_p} \ln \Lambda}$	2.3
inverse shear scale	$\frac{a}{v} = \frac{a^2 B}{V}$	2.9
Alfvén transit	$t_A = \frac{L}{v_A} = \frac{L\sqrt{\mu_0 n_i m_i}}{B} = 4.59 \times 10^{-11} \frac{L\sqrt{n_i}}{B}$	3.2
$E \times B$ rotation	$\frac{2\pi\langle r\rangle}{v_\phi} = \frac{\pi(r_o+r_i)(r_o-r_i)B}{V}$	15
thermal ion transit	$t_{Ti} = \frac{L}{v_{Ti}} = L\sqrt{\frac{m_i}{kT_i}} = 102\frac{L}{\sqrt{T_i}}$	26
holdoff	section 5.1.1	110
formation	section 5.1.2	130
momentum confinement	section 4.1.4	210
plasma RC time	section 5.2.4	220
thermal energy confinement	section 4.1.4	240
mirror particle confinement	τ_{loss}, section C.2.2	910
bank RC	see below	1.8×10^3
sustainment	without crowbar, section 5.1.3	3.6×10^3
viscous	section E.4	4.3×10^4
Bohm diffusion	$\tau_B = \frac{a^2}{D_B} = 1.6 \times 10^7 \frac{a^2 B}{T}$	4.7×10^3
magnetic diffusion time scale	$\tau_b = \frac{\mu_0 a^2}{\eta}$	5.9×10^3
classical ion diffusion	$\frac{a^2}{D_{i\perp}} = \frac{a^2 m_i \omega_{ci}^2}{kT_i \nu_i}$	1.3×10^4
classical electron diffusion	$\frac{a^2}{D_{e\perp}} = \frac{a^2 m_e \omega_{ce}^2}{kT_e \nu_e}$	3.9×10^5

- The current I and power $P = IV$ drawn by the plasma both show rapid decreases as time passes (Figure 5.14),
- with a corresponding increase in the plasma impedance Z.
- The neutral density n_0 also seems to decrease (as calculated from the RC time at the crowbar), while
- the ion density n_i shows a peak of about $6 \times 10^{20}\mathrm{m}^{-3}$ near 1200 μs, with corresponding decreases in n_0/n_i.
- The Alfven Mach number M_A also shows a peak (of 0.45) near 1200 μs.

Figure 5.14: Input Power versus Time: The above plot shows the magnitude of the $I \cdot V$ power input into the plasma in the last 100 μs before the crowbar for each time at which the crowbar was closed. For the equation of the fitted curve, see table I.5. Representative error bars are shown for one point.

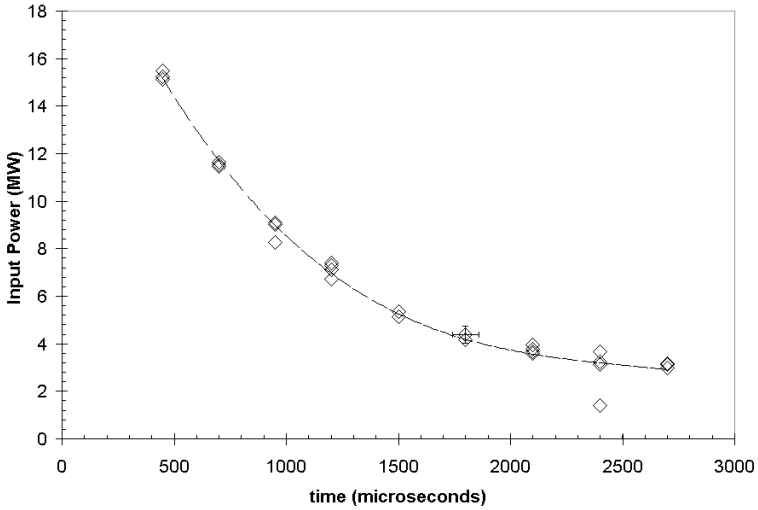

Chapter 6: Planned Upgrades to MCX

There is a series of planned improvements to the MCX device. These are:

6.1 Fiber-optic and Multichord Spectrometry

Direct measurement of the velocity profile would be very helpful in understanding the MCX plasma, since velocity shear is one of the most important parameters in the centrifugal confinement scheme. This measurement may be done by multichord spectroscopy in a fairly straightforward manner, but this will likely require a new CCD camera for the spectrometer and fiber optic coupling of the spectrometer to the machine. Fiber optics will also allow the spectrometer to be moved further away from the magnets and reduce the crowding of hardware near the machine. At this writing, fiber optics have been used successfully a small number of times to direct light from the plasma to the spectrometer, but have not yet been used to perform analysis of the velocity profile.

6.2 Interferometer

A direct measurement of the ion density in the plasma is urgently needed to overcome ambiguities in the circuit model and plasma shape. The typical way to make this measurement is via interferometry, since the index of refraction in a plasma - and thus the ratio of its wavelength to frequency - is strongly dependent on the electron density. A He-Ne interferometer has been borrowed from Swarthmore and tested on the MCX plasma and gives very rough agreement with the ion densities calculated from the current reversal [26], although the interferometer gives densities noticeably lower. (See section F.2.1 for details on the current reversal measurement of ion density.) The two results differ substantially in part because the interferometer is a line-averaged density measurement taken near the mirror plane, while the current reversal measures the mass of the entire rotating plasma. The results from the interferometer are also still quite preliminary, since the data set is very limited. The principal difficulty with the interferometer system is mechanical vibrations of the optical components. These vibrations are large and fast enough to make a large portion of the interferometer data unusable. Mounting a new interferometer system on an optical table and / or substituting a longer-wavelength laser should improve the signal-to-noise ratio.

6.3 Freewheeling Crowbar

An alternative to the use of the crowbar to short the plasma is the use of another switch to interrupt current flow to the plasma. (See section 5.1.4.) The rate at which voltage decays from that point should provide information on the rate at which the plasma rotation decays away, giving the momentum confinement time. The current system uses an ignitron to connect the capacitor bank to the core, closing in about a microsecond, but ignitrons cannot be re-opened until the current through them returns to zero. Several alternatives involving the use of inductors, other ignitrons, and thyratrons are under consideration.

6.4 Diamagnetic Loops and Mirnov Arrays

The current set of $\dot{\mathbf{B}}$ probes have provided tantalizing hints of a rotating magnetic structure inside MCX, but questions remain about the axial and azimuthal structure. Additional magnetic probes are under construction so that a full magnetic-probe array (Mirnov array) may be installed and used to measure axial and azimuthal mode numbers. In particular, more extensive magnetic diagnostics will allow us to determine whether the variations are local or due to flute-like modes that extend the axial length of the plasma. There are also indications that the plasma is not axisymmetric, but the full extent of the deviations are not known. Additional $\dot{\mathbf{B}}$ probes will also allow us to determine the axial extent of the plasma.
Several diamagnetic loops have been constructed and is awaiting *in-situ* calibration. A diamagnetic loop generates a signal voltage via Faraday's Law, $\nabla \times \mathbf{E} + \frac{\partial \mathbf{B}}{\partial t} = 0$, and so is sensitive to changes in the magnetic flux threading the loop. By measuring the change in magnetic flux during a shot, the diamagnetic loops will determine the change in magnetic pressure within its circumference. Under the assumption that the sum of magnetic andthermal pressures is approximately constant, the loop will thus give information about the plasma's thermal pressure. Interpretation of the loop voltage will be somewhat difficult because the plasma diamagnetism and $\mathbf{g} \times \mathbf{B}$ drift currents will create signals of similar magnitude, and because it is expected that some magnetic flux will be pushed toward the core, which is surrounded by a much lower-density plasma. [3]

6.5 ECH Preionization

A great deal of the voltage and charge from the capacitor bank is expended during the early stages of the plasma, as discussed in section 5.1.2, and this process seems to correspond to ionization of the plasma and a build-up of rotation. The input of microwave radiation resonant

with the electron-cyclotron frequency (Electron-Cyclotron Heating or Electron-Cyclotron-Resonance Heating) will ionize a substantial portion of the fill gas and hopefully decrease the $\int IV\,dt$ drawn during the formation phase.

6.6 Augmented Capacitor Banks

We note that the capacitor bank (section A.5.3) used so far in this experiment gives an RC decay time of 1.8 ms, which is somewhat shorter than the time scale of most of our data, so the plasma only approximates steady state conditions. (See table 5.1) This complicates analysis of the design's stability and confinement characteristics. The ion density, for example, reaches its peak at about t = 1200 μs, 1000 μs after breakdown first occurs, and then decays by a factor of 2 in the subsequent 1400 μs. (See table I.5 and section 5.2.7.)

To separate these effects and possibly obtain hotter and faster-rotating plasmas by providing more input power and voltage, preparations are being made to increase the number of capacitors in each bank and / or use secondary capacitor banks to sustain the plasma at a lower current and voltage after the primary banks have been largely drained of charge. There are also plans to vary the impedance between the capacitor bank and the core.

6.7 Improved Insulators

The Teflon, HDPE, and Pyrex insulators which are present in MCX show extensive damage and are likely the source of much of the carbon seen in the discharges as well as other impurities. In addition, the structure of the insulators is not axisymmetric at one end, and this may be the source of some of the non-axisymmetry observed in the plasma's rotation and discharge. Replacing the plastic and glass insulators with alumina will increase the plasma's purity and hopefully lead to higher temperatures. Modifying the insulator geometry for better symmetry may lead to better confinement, higher temperatures and faster rotation. (See section A.6 for more on the current set of insulators.)

6.8 Langmuir Probes

The MCX team also hopes to install several probes to measure the electric potential of the plasma and better determine the outer edge of the plasma. This will provide tighter constraints on the plasma geometry and a better understanding of the electric field's penetration of the plasma.

Chapter 7: Conclusions

7.1 Supersonic Rotation

The MCX plasma rotates faster than the thermal velocity under a wide variety of conditions. Evidence for this rotation comes from several independent diagnostics: Line-emission spectroscopy has been used to show that the rotational velocity exceeds the thermal velocity when we assume that the protons are co-rotating with the ionized carbon impurities and have come to the same temperatures. Since line-integration and reflected light will tend to lower the average Doppler shift and broaden the observed spectrum, purely optical effects will tend to make the measured values for M_S lower than their actual values. (See appendix B for more details on the spectroscopic data.) A plot of two estimates of the Mach number vs. mirror ratio may be found in figure 5.2.4.

Because analysis of plasma rotation is such an important part of MCX's goals, we have not been content to rely purely on spectroscopic data. We have also estimated the rotational velocity based on $\frac{V}{aB}$ and reasonable assumptions of plasma width, finding velocities comparable to those resulting from the spectroscopic analysis. (See sections H.2.1, 4.1.1, and D.1.)

Finally, we have also observed periodic variations on $\dot{\mathbf{B}}$ probes separated in azimuthal angle. From the phase shift between successive probes and the periods of the variations, we find a magnetic field structure rotating with a velocity comparable to that deduced from the spectroscopic and voltage data [3]. (See section 4.3)

7.2 High Density

The ion density has been calculated from the current reversal which results when we short out the plasma's electric field. The stored charge and voltage present just before the crowbar combine to give a measurement of the plasma momentum, which we use to calculate a mass and ion density through comparison to the plasma velocity as described in sections 4.1.2 and F.2.1. Although this method is somewhat indirect, initial comparisons with data from a diffusion model (section F.3) support the ion densities described herein. In addition, we believe the primary component of the plasma is hydrogen rather than high mass impurities since the fill pressure is much higher than the base pressure. Calculations of the density versus mirror

ratio, initial capacitor voltage and magnetic field may be found in figures 5.7, 5.2.2 and 5.11, respectively. All these data show densities of order $10^{20}\mathrm{m}^{-3}$. The density measurements are corroborated by data from the $\dot{\mathbf{B}}$ probes, which have oscillations that correlate well with Alfven-velocity transit times for densities comparable to those measured by the current reversal [3].

7.3 Low Neutral Density

We calculate upper limits on the neutral density based on the plasma RC time and both energy and momentum decay times. Like the ion density, these measurements are not as precise as we would like, but correlate well with each other and with several simple models. Calculations of the density versus mirror ratio and magnetic field may be found in figures 5.7 and 5.11, respectively. Detailed estimates of n_0/n_i from a variety of models may be found in appendix F. These calculations regularly give neutral fractions n_0/n_i less than one part per thousand.

7.4 Quasi-Steady State

Table 5.1 compares the duration of the typical MCX sustainment phase to other time scales relevant to the evolution of the plasma discharge. In particular, the sustainment period is only a factor of 2 longer than the RC decay time of the bank that sustains it, indicating that the limited energy supply is likely limiting the duration of our plasma discharges. Since the lab has many more capacitors available than the 7 used to provide the data for this paper, we have recently moved to a system which uses 20 capacitors to power the core. This seems to increase the duration of the sustainment phase by a factor of about two, although the data are still preliminary. From this, we believe that the magnetic and Bohm diffusion times will not limit the plasma lifetime, even though they currently have magnitudes similar to the sustainment phase's duration.

It should also be noted that the plasma confinement times are much longer than the various collision and transit time scales (Table 5.1), indicating that none of these processes drive instabilities in MCX. In addition, the measured characteristic times for energy and momentum losses are much shorter than the duration of the plasma: Our estimate of the particle and energy confinement times (section C.2.2) predicts these to be somewhat less than 1 ms, but in the absence of a crowbar, the plasma lasts several milliseconds, comparable to the RC decay time of the bank. It is the capacitor bank's loss of charge which causes the decay of the plasma. Recent data show that increasing the number of capacitors also increases the lifetime

of the sustainment phase.

7.5 A Promising Confinement Scheme

We have firmly established the MCX centrifugal confinement scheme as a useful method for obtaining a high density, highly ionized, supersonically-rotating plasma under quasi-steady state conditions. We have also shown that these goals are best met near input parameters of -7 kV, 5 mTorr, 0.2 T, and mirror ratio 9. In the future, we hope to modify the machine to increase the plasma temperature, rotational Mach number, and ion density. We would also like to increase both confinement times and the duration of the typical plasma discharge. These improvements to the plasma may come from additional capacitors, higher magnetic field, or the introduction of baking and improved vacuum components, but we have demonstrated the fundamentals of centrifugal confinement with the current data set. The task now is to provide more diagnostics and a better understanding of the detailed plasma behavior, and to use that increased understanding to further improve the plasma.

Appendix A: Machine Characteristics and Capabilities

The Maryland Centrifugal Experiment (MCX) is a project in the Institute of Research in Electronics and Applied Physics (IREAP) at the University of Maryland - College Park (UMCP) funded by the U.S. Department of Energy (DOE) and UMCP at about $440,000 per annum. The co-Primary Investigators, Rick Ellis and Adil Hassam, proposed and designed the experiment to examine the properties of centrifugally-confined plasmas. Their analyses built on earlier works done by Bo Lehnert[20],[21] and by Adil Hassam,[15],[16] among others. The author has assisted in these theoretical analyses as well as testing and simulating much of the equipment used to run MCX.

The experimental plasma is generated inside a vacuum vessel which is roughly two meters long and 50 centimeters diameter at the midplane. It is contained by magnetic mirror fields which may reach up to 0.23 Tesla at the midplane and 1.9 Tesla at the mirror throats. The maximum attainable mirror ratio is about 20. At this writing, there is no preionization source in place and the plasma is formed directly by the high-voltage discharge from the capacitor banks. Figure 3.1 shows a diagram of the vacuum vessel and attached hardware.

The experimental proposal was based on a number of simulations, including two *Mathematica* notebooks, *MCTrans.nb* and *Bfield.nb*, and a Fortran code, *NMCX*. *MCTrans.nb* is a zero-dimensional model of energy and momentum transport. *Bfield* calculates the vacuum magnetic field. *NMCX* implements a 3D MHD model. (This is the numerical code described by Huang [17].)

A.1 Experimental Cell

The vacuum vessel, magnets, power supplies, diagnostics, and auxiliary equipment associated with MCX are positioned on and under a concrete platform attached to room 0151 in the Energy Research Facility. The diagnostic and control electronics are principally located in an adjacent screen room. The DC power supplies, ignitron firing chassis, magnets, and vacuum vessel are located on top of the deck while the vacuum pumps, gas bottles, high-voltage capacitor banks and their charging supply are located below the deck. A large rectangular hole ("the pit") beneath the midplane of the vacuum vessel allows access to the underside of the machine for high-voltage lines, pumping tubes, and other equipment.

A.2 Vacuum System

The MCX vacuum vessel is a stainless steel tube constructed in three parts of varying dimensions in order to maximize the available plasma volume while facilitating servicing and installation. The main chamber is about 4.1 meters long and 55 centimeters diameter near its midplane. (See figure 3.1.)

The vacuum is generated and maintained by a 1000 L/sec turbopump residing below deck. The turbopump controller, pressure gauge readouts, valve controls, and pumping interlocks are located in a mobile instrument rack below the deck near the pit. At this writing, the vacuum system has not yet been tied into the main computer system, so pressure is manually controlled and monitored. (Section A.7)

Although heating blankets and heating tape have been wrapped around the vessel, they have not yet been turned on. Base pressures are nevertheless in the range of high 10^{-7} Torr. Typical (hydrogen) fill pressures are in the range of 3 - 7 mTorr. Carbon emission lines are evident in the spectroscopic data, but a detailed analysis of impurities has not yet been done.

A.3 Magnetic Field Coils

The MCX magnetic field was originally conceived as having three major components, the *solenoidal field*, *mirror fields*, and *toroidal field*.

A.3.1 Solenoidal Field

The solenoidal field is provided by a pair of 200 layer x 3 turn/layer coils situated near the midplane. (See figure 3.1.) These are powered in series by the Spectromagnetics DC Power Supply (See A.4.) and were originally built for the Maryland Spheromak, covered in foam insulation, and filled with liquid nitrogen so that their resistivity would be low enough that they could generate 1 Tesla fields for that vessel.[9, p. 2]

These "MS coils" have since been stripped of their external insulation, turned upside down, mounted on recirculating-ball plates ("turnomats"), and been drilled through with several large holes to accomodate the possible addition of toroidal field coils. (Section A.3.3) They currently run without active cooling.

They have a total series resistance of 0.71Ω, allowing the Spectromagnetics to drive a peak field at midplane of 2.3 kG by themselves or 3.1 kG with the assistance of the O coils. (See section A.3.2) If the MS coils were driven in parallel, it is expected the field at midplane could be increased as high as 4.5 kG without the O coils, or 5.3 kG with them. This would, however,

Table A.1: Magnets and DC Power Supplies: Both power supplies are voltage-limited in the current configuration, and connecting the magnets in parallel would allow access to higher fields at the expense of inserting additional resistors for load-balancing. The Eratron quasi-DC power supply is used to drive the mirror coils. The Spectromagneitcs DC power supply is used to drive the midplane coils. Field strengths are given in Gauss and Gauss per Amp for the current configuration. The listed Maximum Mirror Field includes the estimated 10% overshoot on Eratron output voltage. The entries for distances between the midplane and coils are measured to the centers of the coils (or coil pair, for the mirror coils).

Eratron nominal current limit	7000 A
Eratron nominal voltage limit	600 V (overshoot $\sim$ 10 %)
Mirror coil average resistance	0.0482 Ω (2 coils per mirror)
Spectromagnetics current limit	962 A
Spectromagnetics voltage limit	177 V
Midplane coil average resistance	0.355 Ω (2 coils near midplane)
Mirror Field per Mirror Amp	5.52 G/A
Mirror Field per Midplane Amp	0.957 G/A
Midplane Field per Mirror Amp	0.265 G/A
Midplane Field per Midplane Amp	9.03 G/A
Maximum Mirror Field	19000 Gauss
Maximum Midplane Field	3100 Gauss
Maximum mirror ratio	20.8
distance of mirror coils from midplane	128 cm
distance of midplane coils from midplane	31 cm

necessitate some care in making sure that equal currents were driven in both coils. If the MS coils are driven without the O coils, the resulting mirror ratio is 0.11.

A.3.2 Mirror Fields

The mirror fields are formed by four 15 layer x 12 turn/layer electromagnet coils (with an effective field / current ratio of 178 turns). Two of these "O-coils" are near either end of the vacuum vessel (See figure 3.1. Our group originally called these magnets "the orange coils" or "O-coils" because of their color. They have since been repainted a dark red, but the name has remained.) and all four are connected in series to an Eratron power supply rated to provide

600 V and 7000 A for up to 10 seconds. They have a total series resistance of 0.1928Ω, allowing the Eratron to drive a peak field at each mirror of 17.2 kG without the MS coils (section A.3.1) or 17.4 kG with them. If each mirror-coil pair was driven in parallel, it is expected the mirror field could be driven as high as 34.4 kG by themselves or 34.6 kG with the MS coils, provided the resistances of both branches were equal. If the O coils are driven without the MS coils, the resulting mirror ratio is 20.8. In practice, the maximum field at the mirrors is about 10% higher than this because during its ramp-up, the Eratron overshoots its target current by about 10% and this feature may be used to briefly raise the maximum output current.
The O coils are water-cooled, although the one farthest from the screen room suffered an impact which has decreased the water flow through the turns on its farthest face. It should be noted by those intending to operate MCX that the mirror fields are strong enough to lift and attract heavy ferrous objects at a distance of several feet. It is essential that the vicinity of the machine be cleared of all ferromagnetic tools and steel objects before each run.

A.3.3 Toroidal Field

A toroidal field would provide a B_θ component, and might be implemented at a future date in order to provide magnetic shear and improved confinement. At present, it is imagined as having perhaps a dozen rectangular turns forming a cage around the machine with their common legs extending along the core. These twelve turns would be driven in parallel by a capacitor bank. Due to the difficulty of installation and the extensive modifications to the core, there are no detailed plans for its construction and operation.

A.4 DC Power Supplies

The Spectromagnetics DC power supply is rated at 177 V and 962 A and is used to drive the MS coils described in section A.3.1. It is not yet under computer control (section A.7) although the current provided to the MS coils is monitored by the PXI system and some design and electrical work has been done in an attempt to create a controller capable of computer-interface. The Spectromagnetics power supply is current regulated and stable to within about 2% of its output current, although the Hall current monitors now being used to measure the current are accurate only to within about 10%.
The Eratron continuous power supply used to drive the O coils (section A.3.2) is rated for a maximum of 600 A and 7000 A for 10 seconds. The Eratron is water-cooled, is under PXI control and is tied into the main interlock system. The lab does not currently have detailed

schematics or manuals for power supply, although it is known that the power supply requires a 5 V Gate pulse to run and that its output is scaled proportionally to a 0 - 10 V "Ref In" voltage. The Eratron has both an internal current monitor ("Amps Out" on the control panel) and a shunt which is monitored through the PXI system.

At present, the Eratron current is measured about once per second, which is comparable to the ring time on the overshoot and the measurements are accurate to within about 10% of the output current. Improvements to the accuracy and frequency of measurement have been discussed, but are not yet being planned in detail.

A.5 Central Electrode and Capacitor Bank

A.5.1 Core

The central electrode of the MCX device is a stainless steel tube with an outer diameter of 4.83 cm (1.90"). (See figure 3.1.) A hollow tube was chosen rather than a solid bar in part to have the option of puffing gas from the center of the machine, though this has not been implemented. Calculations have also shown that for a bar suspended between two points, a thin-walled tube will sag less than a thick-walled tube or a solid rod. The MCX core deviates from a straight line by a few millimeters. This might be improved by inserting a vertical vane down the tube. Precision coaxial positioning of the core, magnetic field, and vessel is important to avoid variations in the magnetic field as seen by the plasma in the rotating frame. Such variations would likely accelerate power loss and might drive instabilities. There are indications from both spectroscopic data and damage to the insulators and vessel wall that the plasma is not fully axisymmetric.

The high voltage of the core (typically 5 kV to 9 kV) combined with the necessity of vacuum seals, the requirement of insulator-based termination of the magnetic field lines (section A.6), and the need to support the heavy core all place tight constraints on the structure of the end assembly. Several different feedthrough schemes were considered, and the version now in place was the second to be implemented.

A.5.2 Ignitrons and Firing Chassis

The timing of the supply of current and voltage to the center electrode (section A.5.1) is provided by a series of ignitrons. These are mercury-filled glass tubes which switch on when an input high-current pulse boils the mercury and switch off only when the current falls low enough (below about 100 A) that the mercury recondenses and falls to the bottom of the tube.

Because of this, the ignitrons are polarity-sensitive and must be vertically mounted.
Each capacitor bank (section A.5.3) is equipped with three ignitrons. The Start ignitron connects the capacitor bank to the core, allowing the initiation of a high-voltage pulse. The Plasma Crowbar (or "Crowbar") ignitron shorts out the plasma, allowing a measurement of a current reversal. (See section 5.1.4.) The Bank Crowbar (or "Freewheeling Crowbar", section 6.3) ignitron diverts the current from the Start ignitron to ground, shutting it off and separating the core from any fixed voltage, allowing measurement of the discharge characteristics without external power input. It is a matter of some difficulty to balance the impedances and voltages such that the freewheeling crowbar shuts off the start ignitron current. See figure 4.1 for a diagram of the discharge circuit.
All six ignitrons receive their trigger pulses from the firing chassis sitting on deck and turn on in less than 2 μs. These ignitrons receive timing pulses from either the PXI system or another timing module. (LabVIEW and PXI are configured to initiate the trigger pulses but there are some difficulties with crosstalk between the high-voltage trigger lines and the digital timing lines. These problems have prompted a temporary shift to a separate timing unit with manual controls.)

A.5.3 Capacitor Banks

The core (section A.5.1) may be connected to either of two capacitor banks, one for each possible polarity of the applied voltage. At the same voltage, the positive polarity (core as anode) seems to do greater damage to the insulators. (See section 5.2.1.)
Although both banks are rated to $\pm$11 kV, the negative bank has shorted out each time more than about 8.5 kV has been applied. The negative bank has seven 176 μF capacitors in parallel; the positive bank has ten. Both banks are connected to the core through a 0.5 Ω resistor. The number of capacitors has recently been increased to 20 with a corresponding increase in the duration of the discharge - see section 6.6.

A.6 Insulators

As mentioned in section A.5.1, the ends of the core are connected to the vessel in a somewhat complex fashion. To prevent discharges in the end regions, the high-voltage core must be insulated from the grounded outer vessel. Since surface discharges arise much more readily than volume break-down, the electrical isolation requires the insulators to be formed of continuous and close-fitting pieces whenever possible. In addition, since hot, partially ionized

plasma conducts electricity well and since a polarization charge may be built up on the insulators, this plasma may lead to an effective short between the core and ground. For this reason, hot ions and electrons must be kept away from the end regions. Also, at least some of the insulators must be load-bearing and precisely shaped to support the core and precisely locate it on the vessel axis. The final constraints are that the magnetic field lines for the rotating plasma must be terminated on insulators (See section 5.2.4.) and that there must be a vacuum feedthrough to the high-voltage core.

Pyrex semicircles bear the core's weight just outside the throats of the magnetic mirrors and pyrex discs terminate the magnetic field lines. (See figure 3.1.) These are supplemented by teflon and HDPE rings which are intended to block plasma from reaching the area *behind* the pyrex discs. (Flash-over surface discharges across the HDPE and teflon parts of the insulators are likely the source of most of the strong, hot carbon lines seen in the spectroscopic data, see appendix B.) Alumina (Al_2O_3) tubes insulate the core from the pyrex discs to the feedthrough. It is hoped that the reduction of impurities will allow the discharge to proceed with less power loss during the formation and sustainment phases (section 5.1); cleaning the vacuum will require replacement of the teflon and HDPE portions of the plasma-facing insulators with vacuum-compatible materials.

A.7 Computer System

Computer control of MCX is based around a series of LabVIEW programs, several CAMAC digitizers, and several National Instruments PXI-based I/O modules. The PC coordinating these elements is housed in the screen room along with the CAMAC rack and the more noise-sensitive PXI modules.

Appendix B: Spectroscopic Measurements

B.1 Introduction

A CCD spectrometer has been used to measure the light emitted from the plasma near the midplane of the machine. Doppler broadenings and shifts of the H-α, C-II, C-III, and C-IV lines have been used to measure the temperature and rotation velocity of the plasma [10]. Both velocity and temperature increase with the ionization state. This is compatible with predictions of separation by ionization energy described by Lehnert [20] since the hotter, faster parts of the plasma will tend to have different ionization states and the optics necessarily integrates over a volume containing a range of temperatures and velocities.

By comparing the Doppler velocity with the measured voltage (c.f. section 4.1), we can estimate the physical width of the plasma using $a = V/(B_{midplane} v_\phi)$.

The entrance slit for the spectrometer is 2 mm high and 50 μm wide, and is focused on a 2 cm-by-0.5 mm region of plasma. See figure 3.3 for the configurations for viewing the plasma through the top and bottom tangential ports.

B.2 Velocity Measurements

Measurements of the rotation velocity and its profile under various conditions are important to understanding how the centrifugal confinement scheme might generalize to a reactor. Study of the velocity profile should also clarify poorly-understood parts of MHD theory and the cause of rotations in tokamak H-mode. Measured MCX velocities have thus far rarely exceeded 80 km/s, although the limiting mechanism is not yet clear.

Experimental evidence for rapid rotation on MCX comes from both the Doppler shift measured by impurity spectroscopy and from the stored electrostatic energy and the charge recovered at the end of each shot. (See section F.2.1.) Variations in v_ϕ with various input parameters are discussed in section 5.2.

B.3 Estimate of Plasma Width from Cross-Field Voltage, Magnetic Field, and Spectroscopic Velocity

Many plasma characteristics depend on estimates of the physical dimensions of the plasma. These include the ion density and ionization fraction and the diffusion time scales. (See Chapters F and G.)

Although we expect the plasma to be approximately bounded by the "good" flux surfaces shown in figure 5.3, at present there is no direct measurement of the plasma dimensions available on MCX. (We will define a "good" flux surface in section 5.2.4.) There are however, several ways to get rough estimates. The crudest measurement is to inspect the insulators at either end of the machine for damage. Comparison of the radial extent of damage to a plot of the vacuum magnetic field implies that the plasma is a shell at least 11 cm thick at the midplane and concentrated on the inboard side of the plasma distribution assumed in section H.2.1. The problems with this technique are obvious: The plasma dimensions may not be the same from one shot to the next, some parts of the end assembly (e.g. the steel core) resist damage more than others, and different parts of the plasma will be at different temperatures and thus inflict different amounts of damage.

A possibly better estimate is to use the measured spectroscopic velocity. Since $\langle v_\phi \rangle = \frac{V}{aB}$, and v_ϕ, V, and B are all measured , we may calculate the plasma width a. This procedure estimates plasma widths to be between 23 and 31 cm for a majority of shots, with the usual assumptions about the velocity profile and magnetic field described in section H.2.1. Not only does this give widths significantly larger than those estimated from insulator damage, but since the distance between the core and the outer wall of the vessel is only 24.3 cm and calculations of the vacuum B field imply only 21.6 cm of that width should be able to rotate without line-tying to the stainless steel walls of the vessel. We note that if the plasma pushes the magnetic field lines in toward the core, only slight increases in the plasma width are possible. (Table 4.1 gives the bounds on the plasma dimension and estimates of the resulting uncertainties in velocity and density.) Since stainless steel is a much better conductor than the plasma's parallel resistivity, most of the voltage drop should be across the plasma. (See section C.1.1 and p. 183 of Chen [4].)

Measurements of the velocity profile can be made with multi-chord spectroscopy and there are plans for this, but this has not yet been done on MCX. For the present, we estimate the velocity profile by several other methods. More on the interpretation of the Doppler shift measurements may be found in sections 4.2 and B.2.

B.4 Spectroscopic Temperature Measurements

The only measurements of temperature which have thus far been done on MCX were made by measuring the width of the emission lines [11]. By comparing the relative intensities of different ionic species of carbon, we estimate the electron temperature as about 15 eV [10]. Substantial velocity shear and reflections may contribute to the temperature. As with the velocity

measurement, it is believed that eventual multi-chord spectroscopy measurements will yield more information on temperature profiles in the plasma. More on the interpretation of the Doppler broadening measurements may be found in section 4.2.

Appendix C: Mirror Confinement and Loss Cones

A mirror machine contains the plasma in a cylindrical geometry whose axially-directed magnetic field is weakest at the midplane and strongest at either end. (See Figure 1.1.) The ratio between the strengths of the magnetic fields at the ends to the field at the center is defined to be the mirror ratio, $\mathcal{R}$. As a supplement to the confinement theory describing MCX, we will briefly examine the confinement characteristics of a conventional mirror machine. This will require knowledge of the Frozen-In Theorem and MHD.

C.1 Magnetohydrodynamics (MHD)

The simplest model commonly used in describing plasmas is Magnetohydrodynamics, although this only works on space and time scales where the electric fields due to individual charges have much shorter ranges than the plasma dimensions. In this section we check these requirements against the MCX plasma.

C.1.1 Conditions for MHD and the Induction Equation

The charges in a plasma move very easily, and the simplest model of plasma dynamics - Magnetohydrodynamics, or MHD - assumes that the space and time scales of the plasma are much larger than the scales on which local charges are neutralized. [5, p. 279] Formally, this requires that the system dimensions be much greater than the Debye length [18, p. 28],

$$\lambda_D = \epsilon_0 \sqrt{\frac{4\pi k T}{n e_0^2}} = 7430 \sqrt{\frac{T}{n}} \text{meters} \tag{C.1}$$

and the time scales of interest must be much greater than the inverse of the plasma frequencies, [12, p. 260]

$$\omega_{pe} = \sqrt{\frac{n_e e_0^2}{\epsilon_0 m_e}} = 56.4 n_e^{\frac{1}{2}} \text{rad / sec} \tag{C.2}$$

$$\omega_{pi} = \sqrt{\frac{n_i Z^2 e_0^2}{\epsilon_0 m_i}} = 1.32 Z \sqrt{n_i \frac{m_p}{m_i}} \text{rad / sec} \tag{C.3}$$

MCX typically uses a hydrogen plasma ($Z \approx 1$, $m_i \approx m_p$), and we expect quasineutrality, $n_e \approx n_i$. Measurements of the plasma in this experiment indicate $n_i \sim 10^{20} m^{-3}$ and $T \sim 30$ eV, so we expect that MCX will have $\lambda_D \sim 4.06 \mu m$, $\omega_{pe}^{-1} \sim 1.77$ ps, and $\omega_{pi}^{-1} \sim 75.8$ ps. Since these scales are much smaller than the length and time scales of MCX operation and

measurement (centimeters and microseconds - compare table 5.1), we may use one of the principal results from MHD, the Induction equation, [5, p. 279]

$$\dot{\mathbf{B}} = \nabla \times (\mathbf{v} \times \mathbf{B}) + \mathbf{c^2}\epsilon_\mathbf{0}\eta\nabla^\mathbf{2}\mathbf{B} \tag{C.4}$$

Here, η is the plasma resistivity, which is made up of components parallel and perpendicular to B, $\eta_\parallel$ and $\eta_\perp$. These are [18, pp. 29, 37]

$$\eta_\perp = 1.03 \times 10^{-4} Z \ln \Lambda T^{-\frac{3}{2}} \Omega\text{m} \tag{C.5}$$

$$\eta_\parallel = 5.26 \times 10^{-5} Z \ln \Lambda T^{-\frac{3}{2}} \Omega\text{m} \tag{C.6}$$

For the MCX parameters noted above, and assuming a Coulomb logarithm $\ln \Lambda \approx 20$, we find $\eta_\perp \sim 1.25 \times 10^{-5}\Omega$m and $\eta_\parallel \sim 6.40 \times 10^{-6}\Omega$m.

C.1.2 The Frozen-In Theorem (Flux Conservation)

The dynamics of the system depend strongly on the ratio of the two terms on the right-hand side of the induction equation, eq. C.4. Spectroscopic and voltage measurements indicate a rotational velocity in the neighborhood of 7×10^4 m/s and the scale width of the system is $a \approx$ 0.21 meters, so the ratio of the two terms on the RHS of the induction equation is on the order of

$$\frac{\nabla v}{c^2\epsilon_0\eta\nabla^2} \sim \frac{a v_\phi}{c^2\epsilon_0\eta_\perp} \sim 2000 \tag{C.7}$$

Since this ratio is much greater than one, we may neglect the resistivity term in modeling the MCX plasma. This approximation leads to the "Frozen-In Theorem":

When the changes in the magnetic field of an MHD plasma are dominated by bulk motion rather than resistive diffusion, the plasma density is closely tied to the strength of the magnetic field, so that decreasing magnetic field strength causes a local expansion of the plasma and vice versa. Thus the magnetic flux is trapped within the plasma, which is often expressed by saying "The magnetic field lines are frozen into the plasma," or "The plasma is frozen to the field lines." (See [12, pp. 120-126] and [5, p. 282].)

On a particle level, neither electrons nor ions may easily cross the magnetic field lines although they move freely along the field lines. A mirror machine combats this parallel motion by increased field strength at either end of the machine. As shall be shown in section C.2.1, this confines particles with some velocities but not others, leading to a "loss cone" in velocity-space.

C.1.3 Ion and Electron Gyroradii

It is often convenient to make the approximation $\frac{\rho}{a} << 1$, where ρ is either the ion and electron gyroradius and a is the plasma width. The gyroradius of a particle (also called its Larmor radius) may be calculated from: [18, p. 28]

$$\rho = \frac{v_T m}{qB} = \frac{\sqrt{kTm}}{qB} \tag{C.8}$$

$$\rho_e = \frac{\sqrt{kT_e m_e}}{e_0 B} = 2.38 \times 10^{-6} \frac{\sqrt{T_e}}{B} \approx 65\mu\text{m} \tag{C.9}$$

$$\rho_i = \frac{\sqrt{kT_i m_i}}{Ze_0 B} = 1.02 \times 10^{-4} \sqrt{\frac{m_i T_i}{m_p Z^2 B^2}} \approx 2.8\text{mm} \tag{C.10}$$

where we have assumed a hydrogen plasma with $T_i \approx T_e \approx$30 eV and $B \approx 0.2$ T. Since these lengths are much smaller than the 21 cm expected for the plasma width, we say that both the ions and electrons are magnetized.

C.2 Mirror Confinement without Rotation

C.2.1 Velocity-Space Loss Cone

The presence of a magnetic field makes the plasma anisotropic, since the charged particles move much more easily along **B** than across it. In a mirror machine, this leads to a rapid loss of particles with velocities aligned close to **B**.

The energy of a charged particle in a non-rotating mirror machine is given by [12, p. 39], [19, p. 34]:

$$W = \frac{m}{2} v_\parallel^2 + \mu B + q\Phi \tag{C.11}$$

Here $v_\parallel$ is the velocity of the particle parallel to the magnetic field B, m is its mass, μ is its magnetic moment, q is the particle's electric charge, and Φ is the electric potential at its location.

To a low-order approximation, both the energy W and the particle's magnetic moment

$$\mu = \frac{m v_\perp^2}{2B} \tag{C.12}$$

are conserved quantities [12, p. 38], so we may equate their values at the mirror and at the midplane. Since different species will escape at different rates dependent on their masses, temperatures, and charges, we expect that in general, a space-charge will arise and Φ will vary between the midplane and the mirrors.

$$\frac{m}{2}v_{\parallel,mir}^2 + \mu B_{mir} + q\Phi_{mir} = \frac{m}{2}v_{\parallel,mid}^2 + \mu B_{mid} + q\Phi_{mid} \tag{C.13}$$

For a marginally-confined particle, $v_{\parallel,mir} = 0$. We take $\Phi = 0$ at the mirrors, resulting in the following equation for a marginally-contained particle [29]:

$$mv_\perp^2\mathcal{R} = mv_\parallel^2 + mv_\perp^2 + 2q\Phi \tag{C.14}$$

$$v_\parallel^2 = (\mathcal{R} - 1)v_\perp^2 - \frac{2q\Phi}{m} \tag{C.15}$$

Here $v_\parallel$, $v_\perp$, and Φ are all evaluated at the midplane. If $v_\parallel$ is larger than this, the particles will escape. If it is smaller, they'll be contained by the mirror.

This is the well-known velocity-space loss cone associated with mirror machines [12, pp. 39-40] and several schemes have been proposed to deal with this defect. We shall later see in appendix D that because of the centrifugal potential introduced by its supersonic rotation, MCX effectively closes the loss cone to particles with parallel velocities less than the rotation speed ($v_\parallel < R\Omega = v_\phi$). This includes thermal ions since $v_\phi \gtrsim c_S \approx v_{Ti}$ but not electrons or energetic ions.

C.2.2 Magnitude of End Losses

Several calculations of mirror losses have been done for collisionless [29] and weakly collisional [28] plasmas. By contrast MCX is fully collisional (see section F.5), and so we use the following method to estimate the mirror losses. [6]

First, we neglect the ambipolar potential which will be set up along the magnetic field by the differences between the ion and electron loss rates. Since we are considering the non-rotating case, we also neglect the pressure gradient established by the plasma's $\mathbf{E} \times \mathbf{B}$ rotation. Then for an initially Maxwellian velocity distribution near the mirror plane, the number of particles which penetrate the mirror and are lost is proportional to the solid angle subtended by the velocity space loss cone. The angle is (section C.2.1):

$$\theta_{lost} = \cot^{-1}\frac{v_\parallel}{v_\perp} = \cot^{-1}\sqrt{\mathcal{R} - 1} \tag{C.16}$$

and the resulting loss factor is

$$p_{lost} = \frac{1}{4\pi} \int_0^{\theta_{lost}} \int_0^{2\pi} \sin\theta \, d\theta \, d\phi \tag{C.17}$$

$$p_{lost} = \frac{1}{2}(1 - \cos\theta_{lost}) \tag{C.18}$$

$$p_{lost} = \frac{1}{2}(1 - \sqrt{1 - \frac{1}{\mathcal{R}}}) \tag{C.19}$$

(For mirror ratio 9, this gives $p_{lost} = 0.029$. This is the fraction of particles near the mirror that are scattered into the loss cone and escape before again colliding. The total number of lost particles and the characteristic loss time are

$$N_{lost} \approx nA\lambda_{mfp}p_{lost} \tag{C.20}$$

$$\tau_{loss} \approx \frac{n\mathcal{V}}{N_{lost}\nu_i} \approx \frac{L}{\lambda_{mfp}p_{lost}\nu_i}\tau_{loss} \approx \frac{L}{p_{lost}v_{Ti}} \tag{C.21}$$

where A is the cross-sectional area of the plasma, n is the local density, and λ_{mfp} is the local mean free path. Using the usual model, we have $L = 1.4$m and $v_{Ti} \approx 5.4 \times 10^4$ m/s. Then

$$\tau_{loss} \approx \frac{1.4}{5.4 \times 10^4 \times 0.029} = 9.1 \times 10^{-4}\text{s} \tag{C.22}$$

This provides a rough estimate for the loss times in a mirror machine. The ambipolar potential established by a plasma is positive, which will tend to accelerate the ion loss rate. To counteract this, we have assumed a length L which is convenient for our density measurements, but which is shorter than the actual machine length, and have ignored the number of particles which will leak *into* the plasma through the mirror. We have also neglected the effects of a pressure gradient and centrifugal confinement, which will tend to decrease the loss rate. (See section D.2.)

In a real plasma, the ambipolar potential forces ions and electrons to be lost at the same net rate. Thermal energy may be lost much faster since hot electrons may leave the plasma and be replaced by cold counterparts from the walls.

C.2.3 Cross-Field Diffusion

A wide variety of laboratory plasmas show loss rates compatible with Bohm diffusion, [4, pp. 190-191]

$$D_B = 6.25 \times 10^{-2} \frac{T}{B} \frac{\text{m}^2}{\text{s}} \tag{C.23}$$

This predicts typical MCX loss rates of about 4.7 ms for the usual assumptions of magnetic field, temperature, and plasma width. (See table 5.1 for a comparison to other time scales.)

Figure D.1: Field geometry for centrifugal confinement: The plasma (shaded region) is trapped between the magnetic field lines as shown by the B field and the velocity shear and confined to large radii by the centrifugal force. The width of the plasma at the midplane is a.

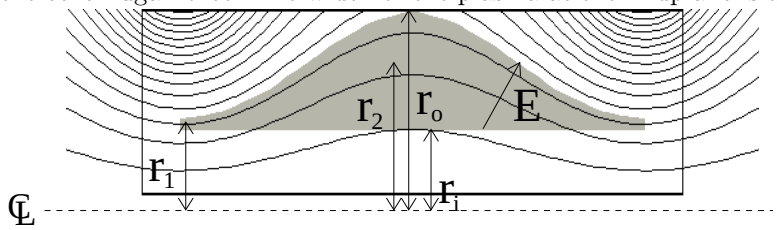

Appendix D: Rotating Plasmas and the Centrifugal Confinement Scheme

D.1 Mechanics of Plasma Rotation

The centrifugal confinement scheme is one in which crossed electric and magnetic fields induce a high-speed sheared azimuthal rotation in a plasma with the cylindrical geometry shown in figure 1.2. The Lorentz force on a charged particle of charge q is $\mathbf{F} = q(\mathbf{E} + \mathbf{v} \times \mathbf{B})$, so there exists a stable velocity at which the two components of the force cancel. This velocity is called the E-cross-B velocity and it is independent of both the charge and mass of the particle. (Thermal motion causes individual particles to move at different velocities, but the electromagnetic forces curve their paths into circular orbits around "guiding centers" which move at the E-cross-B velocity.)

$$\mathbf{v}_{\mathbf{E}\times\mathbf{B}} = \frac{\mathbf{E} \times \mathbf{B}}{B^2} \tag{D.1}$$

Thus by supplementing a traditional mirror machine with a radial electric field, a bulk rotation may be induced in the plasma. In the rotating frame of the plasma, there is an outward centrifugal force which pulls the plasma out to higher radii, enhancing the mirror effect and concentrating the plasma away from the mirrors as shown in figures 1.2 and D.1.
Since charged particles tend to flow much more easily along magnetic field lines than across them, maintaining the difference in electric potential necessary to drive the $\mathbf{E} \times \mathbf{B}$ rotation requires that no sequence of conductors and magnetic field lines connect the high-voltage and low-voltage sides of the plasma. In the cylindrical geometry outlined above, this means that both ends of the cylinder must be insulators with $R_{insulator} >> R_{plasma}$. Measured MCX plasma resistances are typically on the order of one ohm.
In addition, because the magnetic field lines are "frozen" into the plasma, the magnetic field

lines rotate with the plasma. [12, pp. 124-125] The frozen-in conditions are also satisfied inside conductors, so rotating plasmas also require the magnetic field lines to be cut by insulators between the plasma and the vacuum vessel. (Numerically, this gives a condition similar to the constraint on $R_{insulator}$ above.)

A further requirement is that the electric fields penetrate the plasma. If only a very narrow band of plasma becomes ionized, diffusive and other losses will prevent the attainment of the high temperatures and densities necessary for MHD and reactor operation, but the electric field and E-cross-B velocity will be very high. For the centrifugal confinement scheme, we believe that the high velocities of the supersonically-rotating band of plasma will cause impact ionization at the edge of the band, causing the ionized region to spread radially throughout the region capable of rotation. This region would then be limited not by typical sheath scale lengths (such as λ_D) but rather by the geometries of the insulators at the ends of the magnetic field lines. (See the discussion on "good flux surfaces" in section 5.2.4.)

It should also be noted that Lehnert's review of rotating plasmas describes a number of experiments with geometries approximating that of MCX. [20, Type "A" and "B" machines in his paper.] He gives evidence that the machines he includes achieved rotation and penetration of the electric field, and he does not list sheaths as a significant problem.

Experimentally, there is substantial evidence that the electric field penetrates the MCX plasma as well: Large current reversals have been achieved under a wide variety of plasma conditions and these are used to estimate ion densities on the order of $10^{20}\mathrm{m}^{-3}$; (See chapter F.) Rotational velocities upwards of 50 km/s and temperatures of 20 - 30 eV have also been observed spectroscopically; (See section B.2.); magnetic data and current- and voltage- traces also indicate plasma activity. (See appendix B and sections 5.1 and 4.3.) The results of each of these measurements is sufficient to rule out quiescent sheaths, so the aggregate result provides clear evidence for the penetration of electric fields into the plasma.

D.2 Mirror Loss Cone in the Presence of Rotation

The rotation of the plasma reduces the mirror loss cone by adding a centrifugal potential to the mirror confinement. In the rotating frame, this term is

$$U_{centrifugal} = -\frac{m}{2}v_\phi^2 = -\frac{m}{2}r^2\Omega^2 \tag{D.2}$$

Thus, particles with small $v_\parallel$ cannot escape through the mirror, even if their ratio $\frac{v_\parallel}{v_\perp}$ would normally place them in the mirror's loss cone. (See figure D.2.)

Figure D.2: Reduction of mirror loss cone: The area inside a conventional mirror's loss cone encompasses both the dark and lightly-shaded areas, while that in a rotating mirror's loss cone is only the darkest area. If we assume a Maxwellian distribution of the particle velocities, the number of particles at a velocity v is proportional to $e^{-\left(\frac{v}{v_T}\right)^2}$. For a plasma rotating at a high velocity, only those ions with the largest $v_{\|}$ can pass through the mirror planes. The loss cone of conventional mirror machines ceases to apply to low-velocity particles, with the critical speed being comparable to the rotational speed of the plasma.

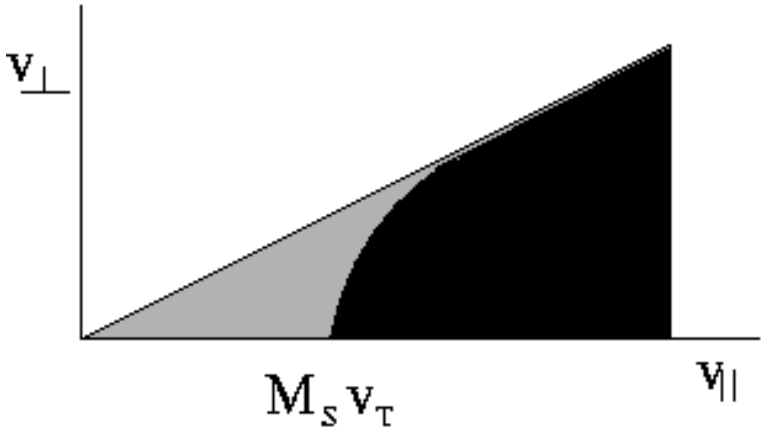

D.3 Requirements for Rotation to be Effective in Closing the Loss Cone

For good confinement, the rotational velocity for a typical magnetic field line passing through the center of the plasma should be four to five times faster than the typical ion velocity v_{Ti} in the rotating frame. [8] Since the magnetic field is strongest at the mirror planes, the magnetic flux per unit area is highest there and the field lines are closest to the axis of symmetry. In particular, any chosen field line will pass through a smaller radius at the mirror plane than at the midplane. The centrifugal force thus pushes the plasma toward the midplane, greatly enhancing the mirror confinement. (See figure D.1.)

D.4 Rotation Velocity

The centrifugal confinement scheme outlined in D.1 depends strongly on the rotation velocity and the velocity shear to suppress instabilities. Doppler-shift measurements of the rotation velocity are shown in figure 5.6. By comparing this rotation velocity to the inferred ion density, plasma volume, and input power, we obtain an estimate of the momentum confinement time,

$$\tau_M = \frac{m_i n_i v_\phi \mathcal{V}}{\partial_t (m_i n_i v_\phi \mathcal{V})} \tag{D.3}$$

$$\tau_M \approx \frac{m_i n_i v_\phi \mathcal{V}}{m_i \mathcal{V}} \frac{1}{\partial_t (n_i v_\phi)} \tag{D.4}$$

$$\tau_M \approx \frac{m_i n_i v_\phi \mathcal{V}}{m_i \mathcal{V}} \frac{1}{\dot{n}_i v_\phi + n_i \dot{v}_\phi} \tag{D.5}$$

$$\tau_M \approx \frac{m_i n_i v_\phi^2 \mathcal{V}}{m_i \mathcal{V}} \frac{1}{\dot{n}_i v_\phi^2 + n_i \dot{v}_\phi v_\phi} \tag{D.6}$$

$$\tau_M \approx \frac{m_i n_i v_\phi^2 \mathcal{V}}{m_i \mathcal{V}} \frac{1}{\dot{n}_i v_\phi^2 + n_i \frac{1}{2} \partial_t (v_\phi^2)} \tag{D.7}$$

$$\tau_M \approx \frac{m_i n_i v_\phi^2 \mathcal{V}}{m_i \dot{n}_i v_\phi^2 \mathcal{V} + \partial_t (m_i n_i v_\phi^2 \mathcal{V})} \tag{D.8}$$

$$\tau_M \approx \frac{m_i n_i v_\phi^2 \mathcal{V}}{m_i \dot{n}_i v_\phi^2 \mathcal{V} + \partial_t (m_i n_i v_\phi^2 \mathcal{V})} \tag{D.9}$$

$$\tag{D.10}$$

In the second equation above, we have assumed that the plasma volume is constant. Since the source of energy for the plasma rotation is the input power, we replace $\partial_t(m_i n_i v_\phi^2 \mathcal{V})$ with the electric power $\langle IV \rangle$. We may neglect the rate of change in the ion density, $\dot{n}_i$, since our crowbar scan indicates $m_i \dot{n}_i v_\phi^2 \approx \frac{1}{2}$ MW after the formation phase, while the input power $\langle IV \rangle$ is typically several megawatts.

$$\tau_M \approx \frac{m_i n_i v_\phi^2 \mathcal{V}}{\langle IV \rangle} \tag{D.11}$$

See sections 4.1.4 and G.4 for more on the momentum confinement time. Section 4.1 describes our measurements of v_ϕ, R, C, and n_i.

(See appendix E for experimental evidence for velocity shear on MCX and section G.4 for theory concerning the momentum confinement time.

The presence of probes in the supersonic flow might introduce shocks which might destroy the confinement, damage the probe, or otherwise alter the plasma's behavior from what it would be had the probe not been inserted; although insertion of an alumina rod showed substantial plasma damage on the side facing into the flow, changes to the plasma because of the probe's presence were negligible. In addition, Lehnert describes a limiting velocity near 110 km/s for a hydrogen plasma at mirror ratio 9 [20, pp. 508-510] but hints that the evidence for it is not entirely conclusive and that although several theoretical models have been proposed, none are entirely satisfactory.

D.5 Sonic Mach Number

The mirror configuration's end losses are reduced by an effective centrifugal force when the plasma is rotating. Since the velocity-space distribution of the ions at the midplane is

$$f(\mathbf{v}) \propto e^{\left(\frac{v}{v_T}\right)^2} \tag{D.12}$$

the degree of centrifugal confinement is most-clearly expressed in terms of the ratio of the rotation velocity to the thermal velocity. Since the ion thermal velocity is comparable to the ion sound speed, we call the ratio of rotation and thermal velocities the Mach number, M_S. The sound speed is not necessarily equal to the thermal velocity [12, pp. 262-263, 300-301], but as we are not here concerned with the description of these waves, we use the term "Mach number" out of convenience and define

$$M_S \equiv \frac{v_\phi}{v_{Ti}} \tag{D.13}$$

D.6 Alfvénic Mach Number

As the plasma rotation velocity approaches the Alfvén velocity

$$v_A = \frac{B}{\sqrt{n_i m_i \mu_0}} \tag{D.14}$$

the charged particles begin to deform the magnetic field, causing it to bow outward. An Alfvén Mach number $M_A \equiv \frac{v_\phi}{v_A}$ substantially less than 1 is thus desirable for the applicability of vacuum-magnetic field calculations. In addition, as M_A increases, the fluid pressure due to the centrifugal motion will rise; instabilities are likely when M_A becomes comparable to 1. This is analogous to the ratio of plasma thermal energy density to magnetic field energy density used in describing tokamaks,

$$\beta_{thermal} = \frac{8\pi nkT}{B^2} \tag{D.15}$$

so by analogy we define a constant to represent the ratio of rotational energy density, [19, p. 793]

$$\beta_{rotation} = \frac{4\pi n_i m_i v_\phi^2}{B^2} \equiv \frac{v_\phi^2}{v_A^2} \tag{D.16}$$

Increased $\beta_{thermal}$ in tokamaks tends to exacerbate instabilities; increased $\beta_{rotation}$ in MCX is also expected to drive instabilities.

Although calculations in this chapter have treated the plasma as if it were rotating as a rigid rotor, the actual situation is more complex. The variation in velocity with radius is treated in appendix E.

Appendix E: Velocity Shear

Although $v'_{\parallel}$ is destabilizing in tokamaks [24], $v'_{\perp}$ can provide substantial stabilization of interchange modes. Velocity shear will only be important if the velocity varies on a scale distance comparable to the plasma dimensions. In addition, it is preferable that the velocity profile not introduce additional instabilities to the plasma.

E.1 Causes of Velocity Shear

The velocity profile varies sharply across the body of the plasma, due in part to the variation in the electric field, but mostly because no-slip boundary conditions apply, so that the plasma speed approximates zero at the inner and outer plasma boundaries.

E.1.1 No-Slip Boundary Conditions

Because the walls of the steel vacuum vessel are conductive, the electrons are highly mobile and the B field lines are effectively frozen-into the walls. Since these field lines also extend into the plasma, the plasma becomes stuck to the walls. Under MHD conditions it is appropriate to assume no-slip boundary conditions, as observed in tokamaks and other devices. This yields a sheared velocity profile.

E.1.2 Electric Potential

The electric field from our simple model (section H.2.1) implies an electric potential

$$\Phi(r) = -\int_r^{r_0} E\,dr = \frac{4v_{\phi max}B}{(r_o - r_i)^2}\int_r^{r_0}(-r^2 + r(r_o + r_i) - r_o r_i)\,dr \tag{E.1}$$

$$\Phi(r) = \frac{4v_{\phi max}B}{(r_o - r_i)^2}(\frac{1}{3}r^3 - \frac{1}{2}r^2(r_o + r_i) + r r_o r_i - \frac{5}{6}r_o^3 + \frac{1}{2}r_o^2 r_i \tag{E.2}$$

where we have taken the outermost edge of the plasma as ground. The variation of the electric field with radius corresponds to a variation in the local $\mathbf{E} \times \mathbf{B}$ velocity, which produces shear.

E.2 Magnitudes of Shear

Using the model described in section H.2.1, we estimate the velocity shear and rotational frequency shear as

$$\partial_r v_\phi = 4 v_{\phi max} \frac{r_o + r_i - 2r}{(r_o - r_i)^2} \tag{E.3}$$

$$\partial_r v_\phi = \frac{6V}{B} \frac{r_o + r_i - 2r}{(r_o - r_i)^3} \tag{E.4}$$

$$\partial_r \Omega_\phi = \frac{4 v_{\phi max}}{(r_o - r_i)^2} \frac{r_o r_i - r^2}{r^2} \tag{E.5}$$

$$\partial_r \Omega_\phi = \frac{6V}{B(r_o - r_i)^3} \frac{r_o r_i - r^2}{r^2} \tag{E.6}$$

For the assumed plasma dimensions with 0.2 T across the midplane sustaining a 3 kV voltage drop, the above equations give shear at the outboard edge of the plasma as $\partial_r v_\phi = -2.0 \times 10^6 \mathrm{s}^{-1}$ and $\partial_r \Omega_\phi = -7.6 \times 10^6 \mathrm{m}^{-1}\mathrm{s}^{-1}$.

E.3 Stability of the Velocity Profile

A necessary condition for the stability of the MCX velocity profile is established by the Rayleigh criterion, which states that an azimuthal flow profile is stable only if $\partial_r(r^4\Omega^2) > 0$ at all radii [5, p. 179]. The Rayleigh criterion is necessary for stability, but not sufficient to guarantee it. The treatment below provides a more rigorous treatment of stability.
Hassam [15] shows that the growth of the nonlinear Rayleigh-Taylor mode is nonlinearly stabilized when

$$v_\phi'^{\,2} \gtrsim g\kappa \ln\left(\frac{\sqrt{g\kappa}}{\mu k_\phi^2}\right) \tag{E.7}$$

where

$$g = \frac{v_\phi^2}{r} \tag{E.8}$$

is the gravitational acceleration, κ is the scale gradient of the electron density,

$$\kappa = \left|\frac{n}{\partial_r n}\right| \tag{E.9}$$

is the scale length of the density gradient, μ is the viscosity, and k_ϕ is the wavenumber of the mode.

$$v_\phi'^{\,2} = 16 v_{\phi max}^2 \frac{4r^2 - 4r(r_o + r_i) + r_o^2 + r_i^2 + 2r_o r_i}{(r_o - r_i)^4} \tag{E.10}$$

$$g = 16 v_{\phi max}^2 \frac{(r_o - r)^2 (r - r_i)^2}{r(r_o - r_i)^4} \tag{E.11}$$

$$\tag{E.12}$$

For κ, we use the ionization gradient scale length $\kappa^{-1} = x_0 = 0.0245$ m calculated from the particle diffusion model in section F.3. ($\kappa = 40.8\text{m}^{-1}$) The smallest available k_ϕ will be the wavenumber corresponding to the circumference, so this most pessimistic estimate (an m=1 mode) is $k_\phi = \frac{1}{r}$. The viscosity we take from section E.4, $\mu = 1.0\frac{\text{m}^2}{\text{s}}$. We also use

$$v_{\phi max} = \frac{3V}{2aB} = 1.1 \times 10^5 \text{m/s} \tag{E.13}$$

Then the argument of the logarithm in equation E.7 is

$$\frac{\sqrt{g\kappa}}{\mu k_\phi^2} = \frac{4 v_{\phi max} \frac{(r_o - r)(r - r_i)}{(r_0 - r_i)^2} \sqrt{\frac{40.8}{r}}}{1.0 r^{-2}} \tag{E.14}$$

$$\frac{\sqrt{g\kappa}}{\mu k_\phi^2} = 2.7 \times 10^6 \frac{(r_o - r)(r - r_i) r^2}{0.21^2 \sqrt{r}} \tag{E.15}$$

$$\frac{\sqrt{g\kappa}}{\mu k_\phi^2} = 6.2 \times 10^7 r^{\frac{3}{2}} (r_o - r)(r - r_i) \tag{E.16}$$

This has its maximum at $r = 0.201$ m, where the logarithm is 10.9. We then use this value to calculate a conservative limit on the RHS of the criterion (E.7):

$$\frac{g\kappa}{{v'_\phi}^2} \ln \frac{\sqrt{g\kappa}}{\mu k_\phi^2} = \kappa \frac{(r_o - r)^2 (r - r_i)^2 (r_o - r_i)^4}{r(r_o - r_i)^4 (4r^2 - 4r(r_o + r_i) + r_o^2 + r_i^2 + 2r_o r_i)} \ln \frac{\sqrt{g\kappa}}{\mu k_\phi^2} \tag{E.17}$$

$$\frac{g\kappa}{{v'_\phi}^2} \ln \frac{\sqrt{g\kappa}}{\mu k_\phi^2} = \kappa \frac{(r_o - r)^2 (r - r_i)^2}{r(4r^2 - 4r(r_o + r_i) + r_o^2 + r_i^2 + 2r_o r_i)} \ln \frac{\sqrt{g\kappa}}{\mu k_\phi^2} \tag{E.18}$$

$$\frac{g\kappa}{{v'_\phi}^2} \ln \frac{\sqrt{g\kappa}}{\mu k_\phi^2} < 445 \frac{(r_o - r)^2 (r - r_i)^2}{r(4r^2 - 4r(r_o + r_i) + r_o^2 + r_i^2 + 2r_o r_i)} \tag{E.19}$$

Stability against the Rayleigh-Taylor interchange will be guaranteed if this quantity is less than 1 or if $\frac{dn}{dr} > 0$. The region between $r = 0.165$ and 0.249 m is not stable by this criterion, however:

First, since we are most concerned with keeping the plasma from reaching the chamber walls, the outermost layer of plasma is the most important for confinement. Near r_o, we have 1.1 cm in which Hassam's criterion implies stability. This is comparable to the scale length for the ion gradient estimated in section F.3 and significantly larger than the ion Larmor radius (of approximately 0.28 cm), so the communication between the interior of the plasma and the chamber walls will not be too great. Near r_i, $\frac{dn}{dr} > 0$ so the density gradient is locally stable. Second, we note that the modeled velocity profile was chosen primarily for ease of computation (section H.2.1) and likely has only a vague resemblance to the MCX plasma.

E.4 Estimates of Viscosity

Since the ions carry most of the momentum and the major velocity and shear directions are perpendicular to each other and the magnetic field, the relevant viscous coefficient is [18, p. 38], [14]

$$\eta_1^i = \frac{3nkT_i}{10\omega_{ci}^2\tau_i} \approx 1.7 \times 10^{-7} \frac{\text{kg}}{\text{m s}} \tag{E.20}$$

Here we have calculated the numerical value by substituting the usual set of parameters for MCX, 0.2 T magnetic field, 30 eV temperatures, and a density of $n = 10^{20}\text{m}^{-3}$. It is often convenient to divide the viscosity by the fluid's mass density nm_i, yielding the kinematic viscosity μ,

$$\mu_1^i \approx 1.0 \frac{\text{m}^2}{\text{s}} \tag{E.21}$$

The kinematic viscosity may be used to calculate the time scale with which collisions tend to smooth out the velocity profile by using $\tau = a^2/\mu$, yielding

$$\tau_1^i = 0.043\text{s} \tag{E.22}$$

Clearly, the time scale τ_1^i eliminates velocity shear on a slower time scale than many other phenomena in MCX. (See table 5.1.)

E.5 Implications of Velocity Shear

The rotational velocity shear damps many macro-instabilities. The relevant measure of velocity shear is $\partial_r\Omega$. The shear is stabilizing because it tends to break up convective cells, suppressing many MHD instabilities, including both the Rayleigh-Taylor and Kelvin-Helmholtz modes. Azimuthal velocity shear has been associated with improved confinement in previous experiments with the tokamak H-mode [13], [2], and has been shown to be stabilizing in various simulations and theoretical works. [15] This is qualitatively explained by noting that the velocity shear stretches the convective cells which facilitate each instability, decreasing their wave numbers k and causing neighboring cells to interfere with each other, effectively slowing the instabilities' growth rates, often to the point of stability. A quantitative analysis demonstrates that the velocity shear must be quite high to suppress these modes, so that velocities significantly greater than the ion sound velocity are necessary. In addition, the turbulent Kelvin-Helmholtz mode will only be stabilized for certain flow profiles. [2], [15]

Appendix F: Ionization Fraction

At this time, MCX has no diagnostic which yields a direct measurement of the ion and neutral densities, n_i and n_0, but several avenues have been used to estimate these quantities.

F.1 Fill Pressure and Temperature-based Estimates

The simplest and coarsest measurement is to check the fill pressure before each shot and use $2(n_i + n_0) \sim \frac{P}{kT}$, where we're assumed hydrogen is the fill gas. At a typical 5 mTorr = 0.67 Pa and T = 273.15 K, this yields $n_i + n_0 \sim 3.5 \times 10^{20}\mathrm{m}^{-3}$ [18]. Since, however, the heat of the discharge will accelerate out-gassing from the wall and the dynamics of the plasma will preferentially drive different types of particles to different areas of the vessel, this is only a rough approximation.

F.2 Current and Voltage-based Estimates

F.2.1 Current-Reversal Estimate of Ion Density

To estimate the ion density, we have used both a constant velocity profile and a constant density profile. The calculation used for the n_i quoted herein proceeds as follows: We take the stored electrostatic energy just before the crowbar to be equal to the rotational kinetic energy: [1]

$$\frac{1}{2}CV^2 = U \sim \frac{1}{2}n_i m_i \mathcal{V} v_\phi^2 \tag{F.1}$$

$$\frac{1}{2}QV = U \sim \frac{\pi}{2}n_i m_i a L (r_o + r_i) v_\phi^2 \tag{F.2}$$

For the velocity v_ϕ, we normally use $v_\phi = \frac{V}{aB}$ in accordance with the result for the bulk-averaged velocity from section H.2.1:

$$\frac{1}{2}QV = U \sim \frac{\pi V^2 n_i m_i L (r_o + r_i)}{2aB^2} \tag{F.3}$$

$$QV \sim \pi n_i m_i L (r_o + r_i)\frac{V^2}{aB^2} \tag{F.4}$$

$$n_i \sim \frac{QaB^2}{\pi V m_i L (r_o + r_i)} \tag{F.5}$$

$$n_i \sim \frac{QV}{\pi v_\phi^2 m_i a L (r_o + r_i)} \tag{F.6}$$

$$n_i \sim \frac{2U}{\pi v_\phi^2 m_i a L (r_o + r_i)} \tag{F.7}$$

A comparison between the results of this calculation for $v_\phi = \frac{V}{aB}$ and for v_ϕ from spectroscopy may be found in figure 5.13. The relation between the mirror ratio and the ion density implied by this method when $v_\phi = \frac{V}{aB}$ is shown in figure 5.7.

Calculations of the ion density using velocity and density profiles may be found in section H.2. The inclusion of profile information tends to lower the measured ion density, but the considered revisions to the circuit model (section H.3) tend to increase the density measurement.

F.2.2 Neutral Density from RC time at Crowbar

The neutral density may be estimated by assuming that the R C time scale of the plasma is approximately the charge-exchange time, τ_{CX}[21]. We use the following equation:

$$\frac{1}{\tau_{CX}} = n_0 \sigma_{CX} v_i \approx n_0 \sigma_{CX} \sqrt{v_{Ti}^2 + v_\phi^2} \tag{F.8}$$

Inverting this gives the following.: [18, p. 29]

$$n_0 \approx \frac{1}{\tau_{CX} \sigma_{CX} \sqrt{v_{Ti}^2 + v_\phi^2}} \tag{F.9}$$

$$n_0 \sim \frac{1}{RC \sigma_{CX} v_{Ti} \sqrt{M_s^2 + 1}} \tag{F.10}$$

$$n_0 \sim \frac{I_{crowbar} V_{crowbar}}{V_{crowbar} Q \sigma_{CX} \sqrt{\frac{kT_i}{m_i}} \sqrt{M_s^2 + 1}} \tag{F.11}$$

$$n_0 \sim \frac{I_{crowbar}}{Q \sigma_{CX}} \sqrt{\frac{m_i}{kT_i (M_s^2 + 1)}} \tag{F.12}$$

For plasmas with temperatures in the range of 10 - 100 eV, the charge-exchange cross-section is $\sigma_{CX} \approx 4 \times 10^{-19} \mathrm{m}^2$ [12, pp. 156-157]. Combining the estimates of ion and neutral densities gives the neutral fraction, n_0/n_i. Plots of the neutral densities thus calculated may be found in figures 5.7 and 5.8.

When compared to the ion density obtained from the electrostatic energy calculation (section F.2.1), equating τ_{RC} to the charge-exchange time typically gives neutral densities on the order of 0.1% of the ion densities. (See, for example, figure 5.7.)

F.2.3 Neutral Density from Momentum and Energy Confinement Times

Variants of the above method may use the momentum or energy confinement times to estimate τ_{CX} instead of the RC decay time. It should be noted that replacing τ_{RC} with either τ_M or τ_E gives an upper bound on the neutral density, since the presence of any other loss mechanisms

will make charge-exchange losses less important, corresponding to fewer neutrals. A comparison of these three estimates of the neutral density may be found in Figure 5.8.

F.3 Estimates from Particle Diffusion Model

F.3.1 Structure of the Particle Diffusion Model

When the neutral mean free path is much less than the plasma width, the ionization fraction may also be estimated using a diffusion model as described in Goldston and Rutherford[12, pp. 158-160]: (See figure H.2.3 for a plot of the profiles implied for the MCX plasma dimensions.)

$$n_i(x) = n_{i\infty} \tanh\left(\frac{x}{x_0}\right) \tag{F.13}$$

$$n_0(x) = n_{00} \mathrm{sech}^2\left(\frac{x}{x_0}\right) \tag{F.14}$$

$$x_0 = \frac{2v_{Ti}}{n_{i\infty}\sqrt{\langle\sigma_{ion}v_e\rangle\langle\sigma_{CX}v_i\rangle}} \tag{F.15}$$

$$n_{00} = \frac{D_c n_{i\infty}}{2D_{0\infty}} \tag{F.16}$$

$$D_{0\infty} = \frac{v_{Ti}^2}{n_{i\infty}\langle\sigma_{CX}v_i\rangle} \tag{F.17}$$

This model assumes ion density $n_i(0) = 0$, $n_0(0) = n_{00}$, $n_i(\infty) = n_{i\infty}$, $n_0(\infty) = 0$, a constant diffusion coefficient D_c for ions and a neutral diffusion coefficient $D_{0\infty}$ at $x \to \infty$.
At the moment, we are interested in bulk-averaged n_i and n_0 for a plasma of width a, so we compute

$$\langle n_i\rangle = \frac{\int_{r_i}^{r_o} n_i(x) r\, dr}{\int_{r_i}^{r_o} r\, dr} \tag{F.18}$$

$$\langle n_0\rangle = \frac{\int_{r_i}^{r_o} n_0(x) r\, dr}{\int_{r_i}^{r_o} r\, dr} \tag{F.19}$$

$$\langle\frac{n_0}{n_i}\rangle = \frac{\int_{r_i}^{r_o} \frac{n_0}{n_i} r\, dr}{\int_{r_i}^{r_o} r\, dr} \tag{F.20}$$

where we use $x = r - r_i$ for $r < \frac{1}{2}(r_i + r_o)$ and $x = r_o - r$ for $r > \frac{1}{2}(r_i + r_o)$. We substitute the following variables:

$$\chi = \frac{x}{x_0} \tag{F.21}$$

$$\xi = \frac{a}{2x_0} \tag{F.22}$$

By splitting each of the above integrals at $r = \frac{1}{2}(r_i + r_o)$, we find

$$\langle n_i \rangle = \frac{2 n_{i\infty} x_0}{a} \int_0^\xi \tanh(\chi)\, d\chi \tag{F.23}$$

$$\langle n_0 \rangle = \frac{2 n_{00} x_0}{a} \int_0^\xi \operatorname{sech}^2(\chi)\, d\chi \tag{F.24}$$

$$\langle \frac{n_0}{n_i} \rangle = \frac{2 n_{00} x_0}{a n_{i\infty}} \int_0^\xi \coth(\chi) \tag{F.25}$$

These can be evaluated using the following identities:

$$\int_0^\xi \tanh(\chi)\, d\chi = \ln(\cosh(\xi)) \tag{F.26}$$

$$\int_0^\xi \operatorname{sech}^2(\chi)\, d\chi = \tanh(\xi) \tag{F.27}$$

$$\int_0^\xi \frac{\operatorname{sech}^2 \chi}{\tanh \chi}\, d\chi = \int_0^\xi \coth \chi\, d\chi = \ln(\sinh(\xi)) \tag{F.28}$$

To use these equations we must next form estimates of the diffusion coefficients $D_{0\infty}$ and D_c. Conservation of momentum and particle number implies that like-particle collisions should not yield a net diffusion of the species, and since ions are much more massive than electrons, the mean free path for ions and ion collision frequency are dominated by ion-ion collisions [12, p. 172]. Electrons, on the other hand, may undergo significant and frequent deflections due to collision with both ions and other electrons. We therefore take D_c from cross-field electron diffusion and $D_{0\infty}$ from Goldston & Rutherford [12, p. 158] as noted above (eq. F.17):

$$D_c \approx \rho_e^2 \nu_e \tag{F.29}$$

Combining the above equations gives

$$n_{00} = \frac{n_{i\infty}^2 \rho_e^2 \nu_e \langle \sigma_{CX} v_i \rangle}{2 v_{Ti}^2} \tag{F.30}$$

$$\chi = \frac{x}{x_0} \tag{F.31}$$

$$\xi = \frac{a}{2 x_0} \tag{F.32}$$

$$\langle n_i \rangle = \frac{2 n_{i\infty} x_0}{a} \int_0^\xi \tanh \chi\, d\chi = \frac{2 n_{i\infty} x_0}{a} \ln\left(\cosh \frac{a}{2 x_0}\right) \tag{F.33}$$

$$\langle n_0 \rangle = \frac{2 n_{00} x_0}{a} \int_0^\xi \operatorname{sech}^2 \chi\, d\chi \tag{F.34}$$

$$\langle \frac{n_0}{n_i} \rangle = \frac{2 n_{00} x_0}{a n_{i\infty}} \int_0^\xi \coth \chi\, d\chi \tag{F.35}$$

and finally,

$$\xi = \frac{a n_{i\infty} \sqrt{\langle \sigma_{ion} v_e \rangle \langle \sigma_{CX} v_i \rangle}}{4 v_{Ti}} \tag{F.36}$$

$$\langle n_i \rangle = \frac{4 v_{Ti}}{a \sqrt{\langle \sigma_{ion} v_e \rangle \langle \sigma_{CX} v_i \rangle}} \ln(\cosh \xi) \tag{F.37}$$

$$\langle n_0 \rangle = \frac{2 n_{i\infty} \rho_e^2 \nu_e}{a v_{Ti}} \sqrt{\frac{\langle \sigma_{CX} v_i \rangle}{\langle \sigma_{ion} v_e \rangle}} \tanh \xi \tag{F.38}$$

$$\langle \frac{n_0}{n_i} \rangle = \frac{4 n_{00} v_{Ti}}{a n_{i\infty}^2 \sqrt{\langle \sigma_{ion} v_e \rangle \langle \sigma_{CX} v_i \rangle}} \ln(\sinh \xi) \tag{F.39}$$

F.3.2 Numerical Results of Particle Diffusion Model

We calculate $\langle \sigma_{ion} v_e \rangle$ from the following [12, p. 151]:

$$\langle \sigma_{ion} v_e \rangle = \frac{2.0 \times 10^{-13}}{6.0 + \frac{T_e}{13.6}} \left(\frac{T_e}{13.6} \right)^{\frac{1}{2}} e^{-\frac{13.6}{T_e}} \tag{F.40}$$

We take v_i as in equation F.8, the charge-exchange cross section as above (section F.2.2), $\ln \Lambda \approx 15$, $v_\phi \approx 80$ km/s, $B \approx 0.2$ T and the plasma width $a = r_o - r_i = 0.21$ m as in section H.2.1 to calculate the densities and their bulk-averaged ratio: [18]

$$T_e \approx T_i \approx 30\text{eV} \tag{F.41}$$

$$\langle \sigma_{ion} v_e \rangle \approx 3.99 \times 10^{-15} \text{m}^3\text{s}^{-1} \tag{F.42}$$

$$v_{Ti} \approx 53.6\text{km/s} \tag{F.43}$$

$$v_i \approx 96.3\text{km/s} \tag{F.44}$$

$$\langle \sigma_{CX} v_i \rangle \approx 3.85 \times 10^{-14} \text{m}^3\text{s}^{-1} \tag{F.45}$$

$$\nu_e \approx 2.66 \times 10^7 \text{s}^{-1} \tag{F.46}$$

$$\rho_e \approx 6.52 \times 10^{-5} \text{m} \tag{F.47}$$

We also take the maximum attainable ion density to be the density of hydrogen atoms implied by the fill pressure at room temperature: $n_{i\infty} \approx 2 \times 2.6868 \times 10^{25} P$ (atm), for a pressure in atmospheres. [18, p. 15] (The factor of 2 enters because hydrogen is diatomic.) For a typical MCX fill pressure of 5 mTorr, this gives

$$n_{i\infty} \approx 3.54 \times 10^{20} \text{m}^3 \tag{F.48}$$

The next quantity we need is the asymptotic ion density, which we calculate from the deep limit of ion density using F.30:

$$n_{00} = 9.45 \times 10^{16}\mathrm{m}^3 \tag{F.49}$$

Calculating the last few quantities is now straightforward:

$$x_0 \approx 0.0245\mathrm{m} \tag{F.50}$$

$$\xi \approx 4.29 \tag{F.51}$$

$$\langle n_i \rangle \approx 2.96 \times 10^{20}\mathrm{m}^{-3} \tag{F.52}$$

$$\langle n_0 \rangle \approx 2.20 \times 10^{16}\mathrm{m}^{-3} \tag{F.53}$$

$$\langle \frac{n_0}{n_i} \rangle \approx 2.24 \times 10^{-4} \tag{F.54}$$

Since electron-electron collisions should not yield a net diffusion [12, pp. 200-206], we should perhaps reduce ν_e by a factor of order 2, but we expect that since ions are much more massive than electrons, any given electron will suffer more large-angle scattering due to ions than due to other electrons. We therefore keep the above formulae, and keep in mind that the actual classical diffusion should be somewhat slower than that predicted by the model.

F.3.3 Caveats for the Particle Diffusion Model

Since the above is a diffusive model, it is only valid when the plasma is substantially thicker than the neutral mean free path. The critical depth parameter is ξ, and $e^{\xi} = 73.0$ must be much larger than 1 for applicability of the model, which we see is the case. Also, the model clearly assumes no losses due to effects such as particle escape along field lines or due to turbulent convective cells. The given estimate of ion density is thus an upper limit on a plasma of given temperature and dimensions.

Another concern with the above model may be noted: It yields a neutral density much lower than the estimates from charge exchange-based models and a very optimistic $\langle \frac{n_0}{n_i} \rangle$. (See for example, figure 5.8 and sections F.2.2 and F.2.3.) This may be mended by replacing the assumption of ion density (eq. F.48) with an assumption of edge neutral density equaling the atom density at the fill pressure. When this is done, the following numbers result:

$$n_{i\infty} = 5.74 \times 10^{29}\mathrm{m}^{-3} \tag{F.55}$$

$$n_{00} = 3.54 \times 10^{20}\mathrm{m}^{-3} \tag{F.56}$$

$$x_0 \approx 4.00 \times 10^{-4}\mathrm{m} \tag{F.57}$$

$$\xi \approx 262 \tag{F.58}$$

$$\langle n_i \rangle \approx 2.16 \times 10^{22}\mathrm{m}^{-3} \tag{F.59}$$

$$\langle n_0 \rangle \approx 1.35 \times 10^{18}\mathrm{m}^{-3} \tag{F.60}$$

$$\langle \frac{n_0}{n_i} \rangle \approx 0.0163 \tag{F.61}$$

This indeed solves the problem of neutral density, but we now instead have an estimate of $\langle n_i \rangle$ which is much higher than our previous estimates (c.f. figure 5.7).

In addition, the Goldston & Rutherford models yield values of $n_{00}/n_{i\infty} >> 1$, which seems heavily counterintuitive, since one would expect the total pressure $P \sim n_i T_i + n_e T_e + n_0 T_0 + B^2$ to be approximately constant across the breadth of the plasma. (We have omitted numerical constants and the effects of rotation for simplicity.) Since $T_i > T_0$ we expect the ion density in the depths of the plasma to be substantially lower than the neutral density at the edge. This suggests that the diffusive model may not be a good model of the MCX plasma. It may be that MCX does not reach a quasi-steady-state, but it is more likely that we have chosen inappropriate values for $D_{0\infty}$ and D_c. There is, however, some reassurance to be gained from the diffusive model: Since we expect there to be loss mechanisms such as turbulence and rapid flow along the insulators to the insulators, we expect that the diffusive model should give lower neutral fractions n_0/n_i than the real plasma. With the observation that the charge exchange-based models have the opposite bias, we may at least be confident that the true ionization fraction lies somewhere in between.

F.4 Neutral Penetration Depth

To estimate the neutral mean free path, we use a model combining the effects of both charge-exchange and electron-impact ionization based on the charge-exchange equation described in equation F.8 and Goldston & Rutherford [12, pp. 155-160]:

$$\lambda_{CX} = \frac{v_0}{n_i \langle \sigma_{CX} v_{Ti} \rangle} \tag{F.62}$$

$$\lambda_{ionize} = \frac{v_0}{n_e \langle \sigma_{ion} v_e \rangle} \tag{F.63}$$

$$\lambda_{mfp} = \left(\frac{1}{\lambda_{CX}} + \frac{1}{\lambda_{ionize}} \right)^{-1} \tag{F.64}$$

To perform these calculations, we use [12, pp.151, 157]

$$\sigma_{CX} \approx 4 \times 10^{-19} \mathrm{m}^2 \tag{F.65}$$

$$\langle \sigma_{ion} v_e \rangle = \frac{2.0 \times 10^{-13}}{6.0 + \frac{T_e}{13.6}} \left(\frac{T_e}{13.6} \right)^{\frac{1}{2}} e^{-\frac{13.6}{T_e}} \tag{F.66}$$

$$T_e \approx T_i \approx 30 \mathrm{eV} \tag{F.67}$$

$$n_e = n_i \approx 10^{20} \mathrm{m}^{-3} \tag{F.68}$$

To calculate the penetration depth of neutrals into the plasma, we must estimate the relative velocity between the neutrals and the edge plasma. An exact calculation of the neutral penetration distances would use the spectra of neutral energies due to photo- and electron impact-dissociation of hydrogen molecules near the walls. Since the binding energy of hydrogen is about 4 eV and kinetic energy should be split between the atoms, for a core temperature of 30 eV we expect typical neutral hydrogen atoms near the edge to have energies on the order of 13 eV. The typical relative velocity between one of these atoms and the bulk plasma is then approximately

$$v_0 \approx \sqrt{v_{T0}^2 + v_{\phi edge}^2} \tag{F.69}$$

where v_{T0} is the thermal velocity of the typical neutral atom and $v_{\phi edge}$ is the plasma velocity in the edge region. Because neither quantity is readily measurable, we estimate them using v_{T0} for 13 eV neutrals and $v_{\phi edge} \lesssim \frac{V}{aB}$. (This may be seen by noting that the edge plasma is slower-moving than the bulk.)

Then for a = 0.21 m, V = 3 kV and B = 0.2 T, a pure-hydrogen plasma, and the other parameters as given above,

$$v_{T0} = 3.66 \times 10^4 \text{m/s} \tag{F.70}$$

$$v_{Ti} = 5.36 \times 10^4 \text{m/s} \tag{F.71}$$

$$\frac{V}{aB} = 7.14 \times 10^4 \text{m/s} \tag{F.72}$$

$$v_0 \lesssim 8.03 \times 10^4 \text{m/s} \tag{F.73}$$

$$\langle \sigma_{ion} v_e \rangle = 2.30 \times 10^{-14} \text{m}^2 \tag{F.74}$$

$$\lambda_{CX} = 3.75 \text{cm} \tag{F.75}$$

$$\lambda_{ionize} = 3.49 \text{cm} \tag{F.76}$$

$$\lambda_{mfp} = 1.81 \text{cm} \tag{F.77}$$

This gives a rough estimate of the depths to which a cold neutral may penetrate the plasma, and shows that ionization will happen about as frequently than charge-exchange. We also note that the λ_{mfp} we calculate here is comparable to the ionization-fraction scale depth x_0 calculated in equation F.50, and is significantly smaller than the plasma width, implying that the core of the plasma should be fully ionized.

F.5 Collision Times and Lengths

Based on the above estimates of ion density and an assumption of quasineutrality, we may calculate the electron and ion collision rates: [18, p. 28]

$$\nu_e = 2.91 \times 10^{-12} \frac{n_e}{T_e^{\frac{3}{2}}} \ln \Lambda \approx 2.7 \times 10^7 sec^{-1} \tag{F.78}$$

$$\nu_i = 4.80 \times 10^{-14} \frac{n_i Z^4}{T_i^{\frac{3}{2}}} \sqrt{\frac{m_p}{m_i}} \ln \Lambda \approx 4.4 \times 10^7 sec^{-1} \tag{F.79}$$

Here we have used $T_e \approx T_i \approx 30$ eV, $n_e \approx n_i \approx 10^{20} m^{-3}$, $m_i \approx m_p$, $Z \approx 1$, and $\ln \Lambda \approx 15$. Inverting these frequencies gives an electron collision time of about 38 ns and an ion collision time of about 2.3 μs. Since observed changes in the plasma take place on time scales longer than 100 μs, and since the typical parallel-transit times are hundreds of nanoseconds for electrons and tens of microseconds for protons, the MCX plasma is fully collisional. Multiplying the above collision frequencies by the particles' thermal velocities gives the mean free paths for electrons and ions:

$$\lambda_{mfp,e} = \frac{v_{Te}}{\nu_e} = 1.44 \times 10^{17} \frac{T_e^2}{n_e \ln \Lambda} \approx 86\text{mm} \tag{F.80}$$

$$\lambda_{mfp,i} = \frac{v_{Ti}}{\nu_i} = 2.04 \times 10^{17} \frac{T_i^2}{Z^4 n_i \ln \Lambda} \approx 0.12\text{m} \tag{F.81}$$

Since the mean free paths for ions and electrons are both much smaller than the machine dimensions, MCX is collisional.

Appendix G: Confinement of Particles, Energy, and Momentum

In this appendix we separately treat ion, electron, energy, and momentum losses. Although these four quantities are individually complex and coupled together, we will separate their causes and effects as much as possible.

G.1 Ion confinement

This section describes the confinement of ions and the principal loss channels, i.e. losses across the field lines due to collisional diffusion and losses through the mirror in spite of mirror and centrifugal effects.

G.1.1 Perpendicular Confinement Time

Perpendicular losses of ions result from diffusion of the ions across the magnetic field lines. Because ions are much more massive than electrons, any given ion is much more likely to suffer a large-angle collision due to another ion than due to an electron, so at first we consider only ion-ion collisions. Since this implies the characteristic step size of the diffusion is one gyroradius and the frequency is the ion-ion collision frequency, we at first find

$$D_{i\perp} \approx \rho_i^2 \nu_{ii} \tag{G.1}$$

$$\tau_\perp \approx \left(\frac{a}{\rho_i}\right)^2 \frac{1}{\nu_{ii}} \tag{G.2}$$

We note, however, that this simple diffusive model is flawed for particle transport in that like-particle collisions should not yield a net diffusion [12, pp. 200-206], and that a more appropriate treatment would use the substantially longer ion-electron collision time:

$$D_{i\perp} \approx \rho_i^2 \nu_{ie} \tag{G.3}$$

$$\tau_\perp \approx \left(\frac{a}{\rho_i}\right)^2 \frac{1}{\nu_{ie}} \tag{G.4}$$

G.1.2 Parallel Confinement Time

In conventional mirror machines, ion loss rates along the magnetic field are much higher than across the field. As described in section C.2.2, the plasma potential due to escaping electrons (Section G.2) accelerates ion loss above what would be expected from single-particle

calculations of mirror confinement. MCX is subject to the same effect, although the rapid rotation serves to mitigate the losses somewhat. (Section D.2.)

We do not yet have direct or space-resolved measurements of the pressure profile in MCX, although it will substantially influence parallel losses. We may however, make order-of-magnitude estimates based on the ion density and temperature. (See appendix F for more on the estimates of ion density.) Using $P = nkT$, and taking typical numbers for temperature (30 eV) and density ($10^{20} m^{-3}$), we find $P \sim 481$ Torr.

In the rotating frame of the plasma, the fluid elements feel an outward centrifugal force, one component of which is directed toward the midplane due to the shape of the magnetic field. Since the velocity varies with radius, this generates a pressure gradient according to the following [16]

$$\mathbf{B} \cdot \nabla P = -nm\mathbf{B} \cdot (\mathbf{u} \cdot \nabla \mathbf{u}) = -nm \sum_{jk} B_j u_k \partial_k u_j \tag{G.5}$$

This yields a pressure gradient, trapping the charged particles at the larger-radii portions of the magnetic field lines, i.e. near the midplane and away from the mirrors. Each magnetic field line and the attached body of plasma rotates as a rigid rotor [8], though field lines on successive flux surfaces slide past each other. (See appendix E for a description of this velocity shear.) Choosing any single field line, then, we have $u = \Omega r$, where Ω is the angular velocity of rotation and r is the radius. This observation gives [8], [22]

$$P(r, \psi) = P_0(\psi) e^{\frac{m_i r^2}{4kT\Omega^2}} \tag{G.6}$$

where ψ specifies a particular flux surface and we have assumed a constant temperature T along the field line. (k is Boltzmann's constant, 1.3807×10^{-23} J / K or 1.6022×10^{-19} J/eV. This also confirms our expectation of good confinement from section D.2, provided we can reach sufficient velocities.

G.2 Electron confinement

Electrons are subject to the same set of losses as ions, so they will not be treated in as much detail here. We do however note that since electrons are much lighter than ions, their thermal velocities are much higher at a given temperature. Assuming $T_e \approx T_i$, we have [18, p. 14]

$$\frac{v_{Te}}{v_{Ti}} \approx \sqrt{\frac{m_i}{m_e}} \approx 43 \tag{G.7}$$

Because of this, the electrons are not centrifugally confined, although the small size of their Larmor radii means they are still magnetized and thus cannot easily cross the magnetic field lines.

As the electrons tend to leave the plasma, however, a positive space charge will build up inside the plasma, creating an electrostatic potential which tends to reduce further electron losses while increasing ion losses. The relationship between plasma potential and the electron loss rate without rotation was derived by Pastukhov [29] for a collisionless plasma, and by Ordonez [28] for a weakly collisional plasma. Our estimate for a collisional plasma is described in section C.2.2.

G.3 Energy confinement

Energy is lost whenever hot particles leave the plasma. Thus all particle-loss channels are also energy-loss channels. In addition, there are two routes by which energy may leave the plasma although the particle balance stays the same. We assume that charge-exchange will be a dominant contributor to energy loss.

Charge-exchange is a process whereby a hot ion collides with a (cold) neutral atom, stripping it of its electron, resulting in a relatively hot neutral atom and a cold ion. [12, pp.155 - 160] This process forms the basis for several of our estimates of ionization fraction (See sections F.3 and F.2.3.) and is expected to be the primary mechanism whereby neutrals penetrate into the cores of hot dense plasmas. Although it does not influence the particle balance, charge exchange can provide the primary energy loss mechanism for small plasmas.

The temperature of the plasma is greatly influenced by the plasma's energy confinement time, τ_E. Energy loss channels include radiative losses, particle losses through the magnetic mirrors and due to cross-field diffusion, charge-exchange losses (since the neutrals are unconfined), and turbulence.

An estimate of the energy confinement time may be obtained by comparing the input power with the measured temperature. (See sections B.4 and 4.1.4 for details on these measurements.)

G.4 Momentum confinement

Cross-field currents are necessary to maintain the rotation. The efficiency with which they do this and the rate at which momentum is lost once the input current is cut off are characterized by the momentum confinement time, τ_M. All of the energy loss channels mentioned in section G.3 are also momentum loss channels except for particle losses through the magnetic mirrors

since particles in the velocity-space loss cone already have small rotational velocities. We estimate the momentum confinement time for the MCX plasma by dividing the measured rotational momentum (from the crowbar data) by the input power. (See section 4.1.4 or D.4.)
As is usual in magnetic confinement, we rely on the MHD result that it is difficult for the charged particles composing a plasma to cross magnetic field lines, but note that they can move freely along the field. Also, as in the mirror-machine scheme, we note that charged particles will tend to avoid the high-field regions near either end of MCX.
All of the processes described above are steady-state well-behaved phenomena, but plasmas are also subject to a wide variety of instabilities which may rapidly change the plasma characteristics, usually leading to greatly increased transport and the destruction of the plasma.

Appendix H: Improvements to Models

H.1 Model of Formation Phase

The MCX group currently has no good model of the plasma formation phase (section 5.1.2), which is particularly troubling since a large portion of the capacitor bank's stored energy is lost very early in the shot. Working out whether the plasma forms, accelerates, and stabilizes due to a critical features of the current, voltage, charge, power, or deposited energy might be used to provide smoother, faster, and more efficient formation phases. Since so much energy is lost early in the discharge, understanding the behavior of the formation phase is critical to extrapolating machine development to proof-of-principle level implementations of centrifugal confinement and in using the conclusions of MCX to influence the designs of other machines.

H.2 Improved Plasma Profiles

The plasma density, velocity, and temperature will vary substantially over the width and length of the MCX plasma in ways that are not currently understood. Improved profile models which account for the effects of viscosity will help, as will better models of the shape of the plasma, including end effects. Careful inspection of figure 5.3 shows that the volumes swept out when the plasma is rotated about the axis are comparable to the volume of plasma assumed by the cylindrical model described in section H.2.1, as shown in table H.1.

H.2.1 Assumed Velocity Profile

Plasma diamagnetism and magnetic fields generated by plasma currents are ignored, reducing the assumed magnetic structure to that of the vacuum case, which is shown for mirror ratio 9 in figure 3.2. In addition, we ignore the plasma resistivity on the basis of section C.1.2, so that the electric equipotential surfaces are coincident with the magnetic flux surfaces and each magnetic field line rotates as a separate rigid rotor [8]. Moreover, we model the plasma as being a cylindrical shell with constant inner and outer radii and axial length $L = 1.4$ meters. The next assumption is that the plasma velocity profile reaches a quadratic form as shown in figure H.1. For inner radius r_i and outer radius r_o, this profile is:

Table H.1: Plasma Volume: The above volumes (in Liters) result when one calculates the volume swept out as the area between the innermost and outermost good flux surfaces is rotated about the machine axis. (See figure 5.3.) For the "small v_ϕ" columns, the radius inner edge r_i was taken to be the same as the innermost good flux surface at all distances z from the midplane. For the "large v_ϕ" columns, r_i is assumed to be a constant at the point where the innermost good flux surface reaches its maximal radius, i.e. ideal centrifugal confinement. The columns marked as "insulator" assume the plasma extends in z to the insulators at either end of the machine. The "mirror" columns assume the plasma does not extend beyond the mirror throats. For comparison, the volume of the cylinder described in section H.2.1 is 305 Liters.

$\mathcal{R}$	small v_ϕ, insulator	small v_ϕ, mirror	large v_ϕ, insulator	large v_ϕ, mirror
3	187	165	183	163
5	259	236	251	231
7	305	283	294	277
9	313	295	299	286
11	288	273	269	260
13	266	255	242	239
15	239	230	213	211
17	228	220	201	200

Figure H.1: Assumed Velocity Profile: We assume a quadratic profile with an inner radius at $r_i = 0.06$ m and an outer radius at $r_o = 0.27$ m, since the inner and outer boundaries of the plasma are expected to be non-rotating. (See section 5.2.4 for information on the inner and outer surfaces.) The velocity displayed above is normalized to its maximum value. Plasma outside this region is presumably line-tied to the walls and non-rotating. The profile is described in section H.2.1.

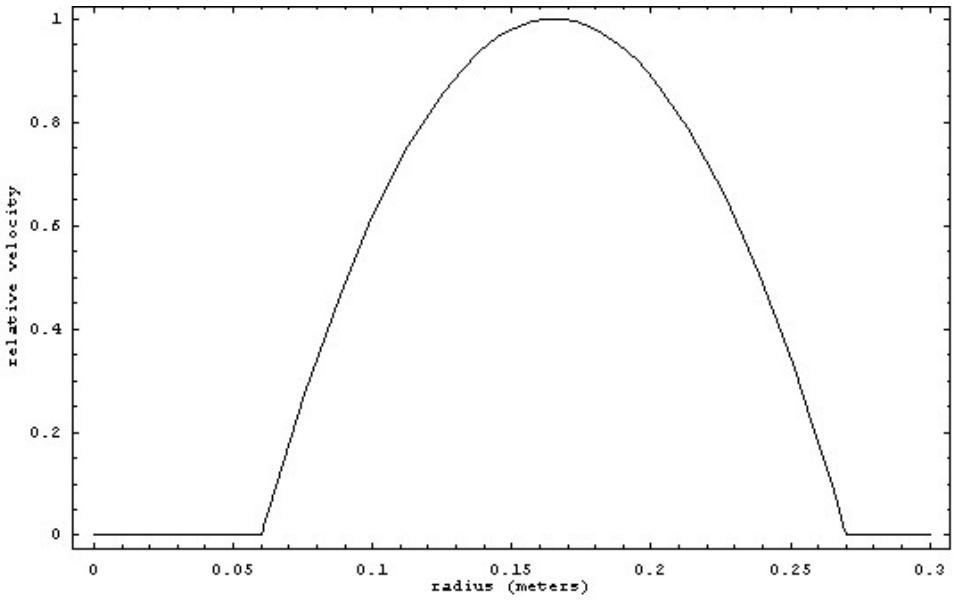

$$v_\phi(r) = 4v_{\phi max}\frac{(r_o - r)(r - r_i)}{(r_o - r_i)^2} \tag{H.1}$$

$$v'_\phi(r) = 4v_{\phi max}\frac{r_o + r_i - 2r}{(r_o - r_i)^2} \tag{H.2}$$

$$\langle v_\phi \rangle = \frac{2\pi \int_{r_i}^{r_o} r v_\phi \, dr}{2\pi \int_{r_i}^{r_o} r \, dr} \tag{H.3}$$

$$\langle v_\phi \rangle = \frac{2}{3} v_{\phi max} \tag{H.4}$$

We have used a factor of r in the integration to calculate the bulk average $\langle v_\phi \rangle$. To calculate the electric field, we use $E_r = v_\phi B$ and integrate to reach:

$$E_r = -4v_{\phi max}B\frac{(r_o - r)(r - r_i)}{(r_o - r_i)^2} \tag{H.5}$$

$$V = -\int_{r_i}^{r_o} E \, dr = \frac{2}{3} B v_{\phi max}(r_o - r_i) \tag{H.6}$$

$$V = \langle v_\phi \rangle B(r_o - r_i) = \frac{2}{3} v_{\phi max} B(r_o - r_i) \tag{H.7}$$

or equivalently,

$$v_{\phi max} = \frac{3V}{2B(r_o - r_i)} \tag{H.8}$$

$$\langle v_\phi \rangle = \frac{V}{B(r_o - r_i)} = \frac{V}{aB} \tag{H.9}$$

where $a = r_o - r_i$ is the plasma width.

Dividing by the radius gives the assumed rotational frequency,

$$\Omega_\phi = \frac{v_\phi}{r} = 4v_{\phi max}\frac{(r_o - r)(r - r_i)}{r(r_o - r_i)^2} \tag{H.10}$$

$$\Omega_\phi = \frac{6V}{B(r_0 - r_i)^3}\frac{(r_o - r)(r - r_i)}{r} \tag{H.11}$$

$$\tag{H.12}$$

Based on the vacuum magnetic field mapping, we assume $r_i = 0.06$ m and $r_o = 0.27$ m, so that the rotational velocity goes to zero at the innermost and outermost good flux surfaces. (See section 5.2.4 for the definition of a "good flux surface.") This procedure gives typical $\langle v_\phi \rangle = 71$ km/s. This cylindrical model gives a plasma volume of 305 Liters, in good agreement with the more precise calculations of table H.1.

Finally, we note that the velocity profile given in equation H.1 meets Rayleigh's stability criterion. (See section E.3 for details.)

H.2.2 Ion Density Calculation with Quadratic v_ϕ and Constant n_i

Our usual estimate of ion density is made without consideration to the velocity and density profiles present in the plasma. (See section F.2.1.) In this section, we calculate the ion density when a velocity profile is taken into account. We estimate the ion density by comparing the stored electrostatic energy ($\frac{1}{2}CV_{crowbar}^2$) to the rotational velocity as before, but use our quadratic velocity profile (section H.2.1 and figure H.1):

$$\frac{1}{2}CV_{crowbar}^2 = U = \frac{1}{2}\int n_i m_i v_\phi^2 \, d\mathcal{V} \tag{H.13}$$

$$U \approx \frac{1}{2} n_i m_i 2\pi L \int_{r_i}^{r_o} v_\phi^2 r \, dr \tag{H.14}$$

$$U \approx \pi n_i m_i L \int_{r_i}^{r_o} \left(4 v_{\phi max} \frac{(r_o - r)(r - r_i)}{a^2}\right)^2 r \, dr \tag{H.15}$$

$$U \approx \frac{3\pi n_i m_i L V^2 (r_o + r_i)}{5aB^2} \tag{H.16}$$

$$n_i \approx \frac{5UaB^2}{3\pi m_i L V^2 (r_o + r_i)} \tag{H.17}$$

$$n_i \approx \frac{5U}{3\pi m_i a L (r_o + r_i)\langle v_\phi \rangle^2} \tag{H.18}$$

$$n_i \approx \frac{15U}{4\pi m_i a L (r_o + r_i) v_{\phi max}^2} \tag{H.19}$$

Here we have assumed that the ion density is independent of radius and that the plasma is a hollow cylinder with a parabolic velocity distribution as described in section H.2.1. We give several versions of the ion density formula so that it may be calculated either from the $\frac{V}{aB}$ velocity, or from direct velocity measurements.

To find the correction this gives to our ion density measurements, we divide this ion density ($n_{i,v0}$) by our usual ion density (from equation F.7 and here labelled $n_{i,00}$), assuming that the velocity in the $n_{i,00}$ calculation is the bulk-averaged velocity:

$$\frac{n_{i,v0}}{n_{i,00}} = \frac{5}{6} = 0.833 \tag{H.20}$$

H.2.3 Ion Density Calculation with Quadratic v_ϕ and Diffusive n_i

The next step in the improvement of plasma profiles is to combine the diffusive-model density profile (described in section F.3 and Goldston & Rutherford [12]) with the assumed velocity profile described in section H.2.1 and figure H.1.

When this is done, the stored-energy calculation is changed to the following:

Figure H.2: Assumed Density Profile: We assume a density profile based on that in the Goldston & Rutherford diffusion model. See sections F.3 and H.2.3 for details. In the diagram above, both the ion and neutral densities are plotted, as normalized to their respective maxima. The ion density is peaked at the center of the plasma and the neutral density is peaked at the edges.

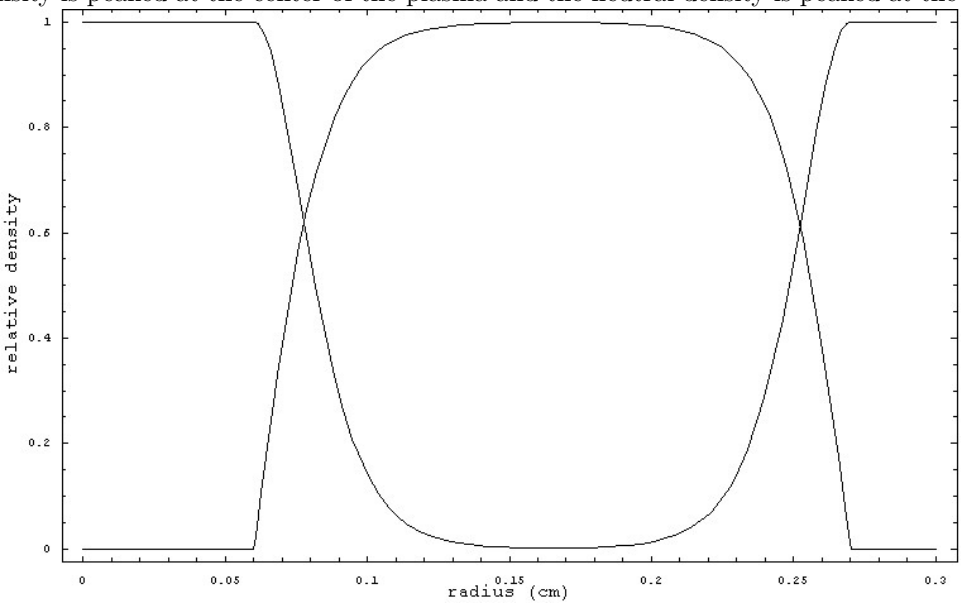

$$U = \int \frac{1}{2} n_i m_i v_\phi^2 \, d\mathcal{V} \tag{H.21}$$

$$U = \pi m_i L \int n_i v_\phi^2 r \, dr \tag{H.22}$$

$$U = \pi m_i L \int_{r_i}^{r_o} \left(n_{i\infty} \tanh\left(\frac{r_{eff}}{x_0} \right) \right) \left(4 v_{\phi max} \frac{(r_o - r)(r - r_i)}{(r_o - r_i)^2} \right)^2 r \, dr \tag{H.23}$$

For the effective depth r_{eff}, we use $r - r_i$ for $r < \frac{1}{2}(r_o + r_i)$ and $r_o - r$ otherwise. (A better formula might be

$$r_{eff} = \left(\frac{1}{r_o - r} + \frac{1}{r - r_i} \right)^{-1} \tag{H.24}$$

but this complicates the integral and is different from the formula used in section F.3.)
Although in reality x_0 will depend on the radius, we here approximate it as the constant 2.45 cm found in equation F.50. We also use $r_i = 0.06$ m and $r_o = 0.27$ m and $a = r_o - r_i$. See figure H.2.3 for these assumed density profiles.

$$U \approx \frac{16\pi m_i L v_{\phi max}^2 n_{i\infty}}{a^4} \int_{r_i}^{r_o} r(r_o - r)^2 (r - r_i)^2 \tanh\left(\frac{r_{eff}}{x_0}\right) dr \tag{H.25}$$

$$U \approx \frac{16\pi m_i L v_{\phi max}^2 n_{i\infty} x_0^3}{a^4} \int_0^{\frac{a}{2x_0}} \alpha^2 (a - \alpha x_0)^2 (r_i + r_o) \tanh\alpha \, d\alpha \tag{H.26}$$

$$U \approx \frac{2\pi m_i a L v_{\phi max}^2 n_{i\infty} (r_i + r_o)}{\xi^5} \int_0^{\xi} \alpha^2 \left(\xi - \frac{\alpha}{2}\right)^2 \tanh\alpha \, d\alpha \tag{H.27}$$

In the second equation, we have split the radial integral into two pieces based on r_{eff}, defined $\alpha = (r - r_i)/x_0$ for the inboard half of the plasma, and $\alpha = (r_o - r)/x_0$ for the outboard half, then recombined the two terms of the integral. In the last integral, we have used the same $\xi = a/2x_0$ as in section F.3. Next we use the equations from the diffusive model and assumed velocity profile (section H.2.1) to convert our scale density and velocity into averaged quantities:

$$n_{i\infty} = \frac{\xi}{\ln(\cosh\xi)} \langle n_i \rangle \tag{H.28}$$

$$v_{\phi max} = \frac{3}{2} \langle v_\phi \rangle \tag{H.29}$$

$$U \approx \frac{9\pi m_i a L \langle v_\phi \rangle^2 \langle n_i \rangle (r_i + r_o)}{2\xi^4 \ln(\cosh\xi)} \int_0^{\xi} \alpha^2 \left(\xi - \frac{\alpha}{2}\right)^2 \tanh\alpha \, d\alpha \tag{H.30}$$

$$\langle n_i \rangle \approx \frac{2U\xi^4 \ln(\cosh\xi)}{9\pi m_i a L \langle v_\phi \rangle^2 (r_i + r_o) \int_0^{\xi} \alpha^2 \left(\xi - \frac{\alpha}{2}\right)^2 \tanh\alpha \, d\alpha} \tag{H.31}$$

We are now ready to put in the values of the dimensionless constants found in section F.3: $\xi = 4.29$ and $\ln(\cosh\xi) = 3.596$. For this value of ξ, the remaining integral equals 188, giving a result for the ion density corrected for both velocity and density profiles, $n_{i,vn}$:

$$n_{i,vn} = 1.44 \frac{U}{\pi m_i a L (r_o + r_i) \langle v_\phi \rangle^2} \tag{H.32}$$

$$\frac{n_{i,vn}}{n_{i,00}} = \frac{0.720}{2} = 0.719 \tag{H.33}$$

In the last line, $n_{i,00}$ is the density calculated without profile considerations from equation F.7.

H.3 Improved Circuit Model

The resistance and capacitance calculations for the MCX plasma presented in this paper ignore perturbations due to each other and any inductances either in the plasma or in the external circuit. Estimates of the contributions from these other effects show that they will shift the values presented for R and C by roughly 10%. To check the accuracy of the resistance measurement, one shot (mcx021031-27) was chosen at random, and the resistance checked carefully from several different measurements:

- First, the measured bank voltage and current traces were compared just before the 2 ms crowbar: $\langle V_{bank}/I_{bank}\rangle|_{1.9-2.0ms} = 1.9\Omega$, $\langle V_{bank}/I_{bank}\rangle|_{2.0-2.1ms} = 0.6\Omega$. The difference gives a measure of the plasma resistance, 1.3 Ω.

- Second, the plasma resistance just before the crowbar was measured in the manner which has been used throughout this paper: $\langle V_{plasma}/I_{plasma}\rangle|_{1.9-2.0ms} = 1.4\Omega$.

- Finally, an RC decay was fit to the bank voltage and current traces just before and just after the crowbar, with the (usual) assumption that the bank had a capacitance of 1.2 mF. The fit to the last 100 μs prior to the crowbar yielded a resistance of 1.9 Ω, and the fit to the next 100 μs gave 0.6 Ω. The difference is 1.3 Ω, a third measure of the plasma resistance.

This data shows that the three estimates for the plasma resistance are equal to within 6.4% of the smallest measurement, in excellent agreement with the circuit model.

Close examination of the current and voltage traces indicates several possible adjustments to the model of the external circuit due to stray inductances and resistances in the ignitrons and cabling. These improvements are shown in figure H.3. The features of the observed current and voltage traces have also been reproduced using a P-Spice circuit simulator and a dummy load have supported the description of the circuit and plasma given in figure H.3. (The "dummy load" consisted of a 176 μF capacitor in parallel with a 2Ω resistor.)

One should also consider that some charge will drain from the core during the current reversal due to currents across the plasma. When this is done, one finds that the stored charge and ion density both rise by 10 % - 50 %, depending on the plasma resistance [26]. To fully compensate for this, one must consider that the plasma's electrical characteristics change as it decays away, so the capacitance and resistance will not be constant after the crowbar.

Complications in the current-reversal measurement of the ion density also occur because the measured current does not return to zero by the end of the CAMAC data record. Although the spurious current is quite small, it is enough to substantially alter $Q = \int I\,dt$ measurements integrated over more than a few hundred microseconds. The error may be due to drift in the CAMAC crate or due to imprecision in the Rogowski coil and RC integrator used to measure the current.

A full analysis of the MCX equivalent circuit would test the model presented in Lehnert's review paper [20].

Figure H.3: Improved Circuit Diagram established by inspecting the voltage drop and current across the crowbar and between the crowbar and plasma, and by comparison with P-Spice simulations. In reality, the inductances of the ignitrons (shown here as 0.2 μH) varies with time and current by about a factor of two. There are also transitory capacitances and resistances across the ignitrons which are significant only when the ignitrons are beginning to conduct. They do induce brief, rapid oscillation on the measured plasma voltage, but do not seem to effect the current. The plasma inductance is typically on the order of 1 μH [25].

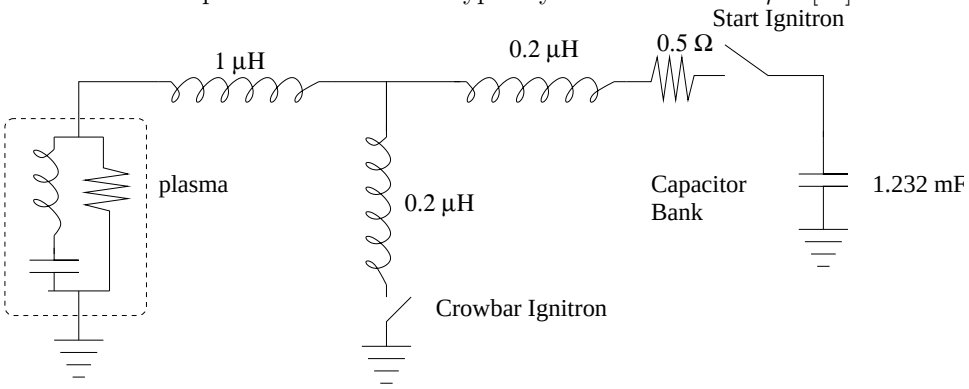

Appendix I: Curve-Fitted Dependencies

This appendix records the experimentally-determined dependencies of a large number of measured parameters on those variables which can be directly controlled in MCX. For each controlled parameter, a scan was done over MCX's normal range of operation, and the resulting data set was fit to several simple curves with the best model being reported here. It should be noted that the "best model" depends in part on subjective factors. Although the correlation coefficient R^2 was used as a guideline, equations giving a higher R^2 were occasionally rejected on the grounds that they missed important features of the data set or were very close to simple equations that gave results almost as good. For reference, $0 \leq R^2 \leq 1$, with 1 showing complete correlation and 0 no correlation.

Table I.1: Measured Dependencies on Initial Bank Voltage: Quantities with the $1.6ms$ subscript are from measurements averaged over the last 100 μs before the crowbar at 1.6 ms (i.e. from 1.5 to 1.6 ms). Quantities with the subscript $1ms$ are averaged from 0.9 to 1.1 ms. Those with the *sustainment* subscript are averaged over the sustainment period, which varies in length, but begins before 1 ms and ends at 1.6 ms. The duration of the holdoff phase is $t_{holdoff}$, and the duration of the formation phase is $t_{formation}$, during which the capacitor bank supplies a total charge $Q_{formation}$ and a total energy $U_{formation}$ to the core. (See section 5.1 for definitions of the demarcations between the holdoff, formation, and sustainment phases.) $V_{holdoff}$ is the average voltage across the chamber before the current starts to flow. $I_{forward}$ is the peak forward (driving) current during the discharge, and $I_{reversed}$ is the peak reversal current. The impedances are defined by $Z = \langle \frac{V(t)}{I(t)} \rangle$. The ion density n_i is plotted versus voltage in figure 5.2.2. $U_{1.6ms}$ is the electrostatic energy of the equivalent capacitor just before the crowbar. τ_{RC} is the RC time of the plasma at the crowbar, as measured in section F.2.2. τ_M and τ_E are the momentum and energy confinement times just before the crowbar - based on spectroscopic measurements of the rotational velocity and temperature - and M_A is the Alfvén Mach number at the crowbar based on the measured ion density and the spectroscopic velocity. Section 5.2.2 describes the stronger trends with initial voltage.

Quantity	Units	Equation	R^2
$P_{sustainment}$	MW	$0.132V_0^3 + 2.75V_0^2 + 17.1V_0 + 37.7$	0.9967
$V_{holdoff}$	kV	$0.998V_0 - 0.320$	0.9966
$t_{holdoff}$	μs	$31.3V_0^3 + 695V_0^2 + 5170V_0 + 13000$	0.9944
$I_{forward}$	kA	$0.803V_0 + 1.96$	0.9890
$t_{formation}$	μs	$16.7V_0^3 + 404V_0^2 + 3260V_0 + 8880$	0.9835
$P_{1.6ms}$	MW	$0.286V_0^3 + 5.78V_0^2 + 37.7V_0 + 84.1$	0.9713
$I_{reversed}$	kA	$-1.78V_0^3 - 38.8V_0^2 - 276V_0 - 632$	0.9296
$Q_{formation}$	C	$0.057V_0^2 + 0.868V_0 + 3.60$	0.9133

$V_{sustainment}$	kV	$0.232V_0^2 + 3.24V_0 + 7.96$	0.9086
$U_{formation}$	J	$176V_0^2 + 2630V_0 + 11000$	0.9048
$Q_{reversed}$	C	$-0.0494V_0^3 - 1.10V_0^2 - 7.97V_0 - 18.6$	0.9018
$Z_{sustainment}$	Ω	$-0.0906V_0^3 - 2.03V_0^2 - 14.6V_0 - 32.2$	0.8893
$I_{1.6ms}$	kA	$-0.392V_0^2 - 4.72V_0 - 15.5$	0.8854
τ_{RC}	μs	$-51.3V_0^3 - 1120V_0^2 - 8020V_0 - 18400$	0.8723
$Z_{1.6ms}$	Ω	$-0.282V_0^3 - 6.12V_0^2 - 43.0V_0 - 95.9$	0.8540
n_i	m^{-3}	$-5 \times 10^{19}V_0^3 - 10^{21}V_0^2 - 8 \times 10^{21}V_0 - 2 \times 10^{22}$	0.8507
$U_{1.6ms}$	J	$-62.6V_0^3 - 1480V_0^2 - 11200V_0 - 27100$	0.8398
$n_{0,RC}$	m^{-3}	$5 \times 10^{16}V_0^3 + 1 \times 10^{18}V_0^2 + 9 \times 10^{18}V_0 + 2 \times 10^{19}$	0.8207
$V_{1.6ms}$	kV	$0.477V_0^2 + 6.07V_0 + 16.0$	0.7709
$\frac{n_0}{n_i}$		$0.0002V_0^3 + 0.0047V_0^2 + 0.0337V_0 + 0.0795$	0.7496
I_{1ms}	kA	$0.191V_0^3 + 3.73V_0^2 + 24.3V_0 + 50.5$	0.7392
M_A		$-0.029V_0^3 - 0.621V_0^2 - 4.43V_0 - 10.2$	0.7384
τ_M	μs	$-75.1V_0^2 - 975V_0 - 2.95 \times 10^3$	0.7072
τ_E	μs	$-128V_0^2 - 1.68 \times 10^3V_0 - 5.20 \times 10^3$	0.5686
Z_{1ms}	Ω	$0.452V_0^3 + 0.09V_0^2 + 60.5V_0 - 134$	0.5375
V_{1ms}	kV	$-0.275V_0^3 - 5.47V_0^2 - 35.8V_0 - 79.8$	0.5242

Table I.2: Measured Dependencies on Fill Pressure: $P_{1.6ms}$ is $\langle I(t)V(t)\rangle$ averaged over the last 100 μs before the crowbar at 1.6 ms (i.e. from 1.5 to 1.6 ms). Quantities with the subscript $1ms$ are averaged from 0.9 to 1.1 ms. Those with the *sustainment* subscript are averaged over the sustainment period, which varies in length, but begins before 1 ms and ends at 1.6 ms. The duration of the holdoff phase is $t_{holdoff}$. $V_{holdoff}$ is the average voltage across the chamber before the current started to flow. $I_{forward}$ is the peak forward (driving) current during the discharge. The impedances are defined by $Z = \langle\frac{V(t)}{I(t)}\rangle$. $n_{0,G\&R}$ is the neutral density calculated from the diffusion model in section F.3, and T_{maxv_ϕ} is the temperature of the fastest-moving carbon emission line as measured by Doppler spectroscopy. Section 5.2.3 describes the stronger trends with fill pressure.

Quantity	Units	Equation	R^2
$t_{holdoff}$	μs	$1190P_{fill}^{-1.51}$	0.9801
$I_{forward}$	kA	$0.0035P_{fill}^2 - 0.1241P_{fill} - 3.18$	0.9188
$P_{1.6ms}$	MW	$-0.0947P_{fill} + 5.62$	0.9159
V_{1ms}	kV	$0.06P_{fill} - 3.71$	0.9063
$V_{sustainment}$	kV	$0.059P_{fill} - 3.60$	0.8959
$n_{0,G\&R}$	m^{-3}	$2\times10^{11}P_{fill}^3 - 2\times10^{12}P_{fill}^2 + 9\times10^{12}P_{fill} + 10^{13}$	0.8865
$P_{sustainment}$	MW	$0.0051P_{fill}^2 - 0.1905P_{fill} + 8.37$	0.8462
Z_{1ms}	Ω	$0.0004P_{fill}^3 - 0.0151P_{fill}^2 + 0.1469P_{fill} + 1.21$	0.8358
$Z_{sustainment}$	Ω	$-0.0008P_{fill}^2 - 0.0204P_{fill} + 1.65$	0.8229
$V_{holdoff}$	kV	$-0.0007P_{fill}^3 + 0.0217P_{fill}^2 - 0.136P_{fill} - 7.17$	0.7923
I_{1ms}	kA	$0.0003P_{fill}^3 - 0.0153P_{fill}^2 + 0.188P_{fill} - 2.74$	0.6993
T_{maxv_ϕ}	eV	$0.0305P_{fill}^3 - 1.16P_{fill}^2 + 12.0P_{fill} - 6.33$	0.5686
$V_{1.6ms}$	kV	$0.0863P_{fill} - 3.46$	0.6026

Table I.3: Measured Dependencies on Mirror Ratio: Quantities with the $1.6ms$ subscript are from measurements averaged over the last 100 μs before the crowbar at 1.6 ms (i.e. from 1.5 to 1.6 ms). Quantities with the subscript $1ms$ are averaged from 0.9 to 1.1 ms. Those with the *sustainment* subscript are averaged over the sustainment period, which varies in length, but begins before 1 ms and ends at 1.6 ms. The duration of the Holdoff Phase is $t_{holdoff}$. $V_{holdoff}$ is the average voltage across the chamber before the current started to flow. $I_{forward}$ is the peak forward (driving) current during the discharge and $I_{reverse}$ is the maximum current returned from the core when the crowbar is fired. When the reversal current is integrated, it gives $Q_{reverse}$. v_ϕ gives the velocity of the fastest-moving Doppler-shifted line found by the spectroscopy. The impedances are defined by $Z = \langle\frac{V(t)}{I(t)}\rangle$. $\frac{V}{Bv_\phi}$ gives an estimate of the scale length of the electric potential at the position of the largest observed Doppler shift. $M_S|_{\langle v_\phi,T\rangle}$ is an average rotational Mach number for the plasma, using averages of the multiple Doppler shifts and Doppler broadenings from each shot; these multiple broadenings are averaged to yield $\langle T\rangle$. T_{maxv_ϕ} gives the temperature of the ion species showing the highest Doppler shift, $M_S|_{maxv_\phi}$ gives its Mach number, and M_A gives the ratio of its velocity to the Alfvén velocity. Figure 5.2.4 shows the dependence of both estimates of the Mach number on mirror ratio. n_i is the ion density from the stored electrostatic energy calculation (section F.2.1); $n_{0,RC}$ is calculated from the plasma RC time (section F.2.2), and $n_{0,G\&R}$ is the neutral density from the diffusion model presented in section F.3. τ_M, τ_E and τ_{RC} are the momentum confinement, heat confinement and plasma RC times. (The confinement times are calculated in section 4.1.4; the plasma RC time is described in section F.2.2.) $U_{1.6ms}$ is the electrostatic energy of the equivalent capacitor just before the crowbar. The neutral fraction $\frac{n_0}{n_i}$ uses the neutral density from the RC time and the ion density from the electrostatic energy calculation.

Quantity	Units	Equation	R^2
$I_{reverse}$	kA	$0.004\mathcal{R}^3 - 0.178\mathcal{R}^2 + 2.53\mathcal{R} - 4.63$	0.9847
n_i	m^{-3}	$2 \times 10^{17}\mathcal{R}^3 - 8 \times 10^{18}\mathcal{R}^2 + 10^{20}\mathcal{R} - 2 \times 10^{20}$	0.9737
$Q_{reverse}$	C	$0.0003\mathcal{R}^3 - 0.012\mathcal{R}^2 + 0.170\mathcal{R} - 0.386$	0.9682
$V_{sustainment}$	kV	$-0.0008\mathcal{R}^3 + 0.0292\mathcal{R}^2 - 0.357\mathcal{R} + 0.0445$	0.9615
Z_{1ms}	Ω	$0.0002\mathcal{R}^3 - 0.0073\mathcal{R}^2 + 0.935\mathcal{R} - 0.0201$	0.9615
$V_{1.6ms}$	kV	$-0.0008\mathcal{R}^3 + 0.0317\mathcal{R}^2 - 0.391\mathcal{R} + 0.294$	0.9611
$Z_{sustainment}$	Ω	$0.0002\mathcal{R}^3 - 0.0094\mathcal{R}^2 + 0.118\mathcal{R} - 0.0866$	0.9609
τ_M	μs	$0.0351\mathcal{R}^3 - 1.65\mathcal{R}^2 + 23.8\mathcal{R} - 56.2$	0.9594
τ_{RC}	μs	$0.174\mathcal{R}^3 - 7.80\mathcal{R}^2 + 110\mathcal{R} - 255$	0.9574
V_{1ms}	kV	$-0.0006\mathcal{R}^3 + 0.0251\mathcal{R}^2 - 0.3116\mathcal{R} - 0.0057$	0.9559
$P_{1.6ms}$	MW	$0.0011\mathcal{R}^3 - 0.0423\mathcal{R}^2 - 0.520\mathcal{R} - 0.0457$	0.9551
M_A		$0.0003\mathcal{R}^3 - 0.0138\mathcal{R}^2 + 0.203\mathcal{R} - 0.461$	0.9519
$P_{sustainment}$	MW	$0.0031\mathcal{R}^3 - 0.1153\mathcal{R}^2 + 1.39\mathcal{R} + 1.08$	0.943
$U_{1.6ms}$	J	$0.153\mathcal{R}^3 - 7.38\mathcal{R}^2 + 109\mathcal{R} - 270$	0.9400
$Z_{1.6ms}$	Ω	$0.0006\mathcal{R}^3 - 0.0228\mathcal{R}^2 + 0.281\mathcal{R} - 0.33$	0.9277
v_ϕ	km/s	$0.05\mathcal{R}^3 - 2.03\mathcal{R}^2 + 27.2\mathcal{R} - 50.9$	0.9264
$I_{forward}$	kA	$0.740 \ln \mathcal{R} - 11.4$	0.8774
$\frac{V}{Bv_\phi}$	m	$-0.0006\mathcal{R}^3 + 0.0211\mathcal{R}^2 - 0.249\mathcal{R} + 1.52$	0.8446
$M_S\|_{\langle v_\phi, T \rangle}$		$-0.0054\mathcal{R}^2 + 0.139\mathcal{R} + 0.135$	0.8344
I_{1ms}	kA	$-0.0029\mathcal{R}^2 + 0.0667\mathcal{R} - 3.83$	0.8238
$M_S\|_{maxv_\phi}$		$-0.0109\mathcal{R}^2 + 0.277\mathcal{R} - 0.269$	0.8127
$\frac{n_0}{n_i}$		$0.222\mathcal{R}^{-2.38}$	0.7978
$t_{holdoff}$	μs	$0.0109\mathcal{R}^3 - 0.422\mathcal{R}^2 + 5.06\mathcal{R} - 4.70$	0.7769
$I_{1.6ms}$	kA	$0.0003\mathcal{R}^3 - 0.0138\mathcal{R}^2 + 0.167\mathcal{R} - 2.24$	0.7567
$n_{0,RC}$	m^{-3}	$7 \times 10^{18}\mathcal{R}^{-1.45}$	0.748
$V_{holdoff}$	kV	$-0.0024\mathcal{R}^3 + 0.0859\mathcal{R}^2 - 0.925\mathcal{R} - 3.68$	0.6255
$n_{0,G\&R}$	m^3	$-5 \times 10^{10}\mathcal{R}^3 + 8 \times 10^{11}\mathcal{R}^2 + 3 \times 10^{12}\mathcal{R} + 3 \times 10^{13}$	0.5991
T_{maxv_ϕ}	eV	$0.0511\mathcal{R}^3 - 1.62\mathcal{R}^2 + 16.0\mathcal{R} - 24.4$	0.5742
$\langle T \rangle$	eV	$0.0362\mathcal{R}^3 - 1.15\mathcal{R}^2 + 11.4\mathcal{R} - 13.2$	0.5733
τ_E	μs	$0.178\mathcal{R}^3 - 6.16\mathcal{R}^2 + 65.4\mathcal{R} - 101$	0.5161

Table I.4: Measured Dependencies on Magnetic Field: $B_{mid} = B_{midplane}$ is in Gauss. Quantities with the $1.6ms$ subscript are from measurements averaged over the last 100 μs before the crowbar at 1.6 ms (i.e. from 1.5 to 1.6 ms). Quantities with the subscript $1ms$ are averaged from 0.9 to 1.1 ms. Those with the *sustainment* subscript are averaged over the sustainment period, which varies in length, but begins before 1 ms and ends at 1.6 ms. The duration of the holdoff phase is $t_{holdoff}$. $V_{holdoff}$ is the average voltage across the chamber before the current started to flow. $I_{forward}$ is the peak forward (driving) current during the discharge and $I_{reverse}$ is the maximum current returned from the core when the crowbar is fired. When the reversal current is integrated, it gives $Q_{reverse}$. v_ϕ gives the velocity of the fastest-moving Doppler-shifted line found by the spectroscopy. The impedances are defined by $Z = \langle \frac{V(t)}{I(t)} \rangle$. $\frac{V}{Bv_\phi}$ gives an estimate of the scale length of the electric potential at the position of the largest observed Doppler shift. n_i is the ion density from the stored electrostatic energy calculation (section F.2.1); $n_{0,RC}$ is calculated from the plasma RC time (section F.2.2). τ_M and τ_{RC} are the momentum confinement and plasma RC times. (The confinement times are calculated in section 4.1.4; the plasma RC time is described in section F.2.2.) $U_{1.6ms}$ is the electrostatic energy of the equivalent capacitor just before the crowbar. The neutral fraction $\frac{n_0}{n_i}$ uses the neutral density from the RC time and the ion density from the electrostatic energy calculation. Figures 5.12 and 5.11 plot the forward and reverse currents and the ion and neutral densities as magnetic field changes.

Quantity	Units	Equation	R^2
$I_{forward}$	kA	$7 \times 10^{-7} B_{mid}^2 + 0.001 B_{mid} - 11.6$	0.995
$t_{holdoff}$	μs	$7 \times 10^{-8} B_{mid}^3 - 0.0002 B_{mid}^2 + 0.2325 B_{mid} - 78.919$	0.9925
$P_{sustainment}$	MW	$5.85 \ln B_{mid} - 34.1$	0.9920
n_i	m^{-3}	$6 \times 10^{11} B_{mid}^3 - 3 \times 10^{15} B_{mid}^2 + 4 \times 10^{18} B_{mid} - 2 \times 10^{21}$	0.9751
$P_{1.6ms}$	MW	0.002 B_{mid} - 0.0935	0.9476
$V_{sustainment}$	kV	$-3 \times 10^{-9} B_{mid}^3 + 10^{-5} B_{mid}^2 - 0.0163 B_{mid} + 6.34$	0.9065

$\frac{n_0}{n_i}$		$-3 \times 10^{-12} B_{mid}^3 + 1 \times 10^{-8} B_{mid}^2 - 2 \times 10^{-5} B_{mid} + 0.0083$	0.9027
V_{1ms}	kV	$-3 \times 10^{-9} B_{mid}^3 - 10^{-5} B_{mid}^2 - 0.02 B_{mid} + 7.91$	0.8436
$V_{holdoff}$	kV	$6 \times 10^{-7} B_{mid}^2 - 0.0024 B_{mid} - 4.80$	0.8004
$U_{formation}$	J	$8 \times 10^{-7} B_{mid}^3 - 0.0042 B_{mid}^2 + 7.46 B_{mid} - 3180$	0.7846
$Z_{sustainment}$	Ω	$2 \times 10^{-9} B_{mid}^3 - 7 \times 10^{-6} B_{mid}^2 + 0.0093 B_{mid} - 3.69$	0.761
$I_{reversed}$	kA	$2 \times 10^{-8} B_{mid}^3 - 0.0001 B_{mid}^2 + 0.137 B_{mid} - 53.3$	0.7361
Z_{1ms}	Ω	$2 \times 10^{-9} B_{mid}^3 - 7 \times 10^{-6} B_{mid}^2 + 0.01 B_{mid} - 4.05$	0.7065
$U_{1.6ms}$	J	$2 \times 10^{-6} B_{mid}^3 - 0.0081 B_{mid}^2 + 10.7 B_{mid} - 4340$	0.6887
v_ϕ	km/s	$0.0389 B_{mid} + 35.8$	0.6798
$Q_{reverse}$	C	$10^{-9} B_{mid}^3 - 5 \times 10^{-6} B_{mid}^2 + 0.007 B_{mid} - 2.61$	0.6492
$Z_{1.6ms}$	Ω	$4 \times 10^{-9} B_{mid}^3 - 2 \times 10^{-5} B_{mid}^2 + 0.201 B_{mid} - 7.88$	0.6467
$V_{1.6ms}$	kV	$-0.0012 B_{mid} + 0.0734$	0.6474
$t_{formation}$	μs	$-5 \times 10^{-5} B_{mid}^2 + 0.141 B_{mid} - 43.1$	0.63
$n_{0,RC}$	m^{-3}	$-7 \times 10^8 B_{mid}^3 + 3 \times 10^{12} B_{mid}^2 - 4 \times 10^{15} B_{mid} + 2 \times 10^18$	0.5962
τ_M	μs	$3 \times 10^{-7} B_{mid}^3 - 0.0012 B_{mid}^2 + 1.52 B_{mid} - 584$	0.5848
τ_{RC}	μs	$10^{-6} B_{mid}^3 - 0.0041 B_{mid}^2 + 5.31 B_{mid} - 1990$	0.5689
$Q_{formation}$	C	$3 \times 10^{-10} B_{mid}^3 - 2 \times 10^{-6} B_{mid}^2 + 0.0028 B_{mid} - 0.9965$	0.5540

Table I.5: Measured Dependencies on Time: $t = t_{crowbar}$ is the time in microseconds at which the crowbar is fired. Quantities with the *crowbar* subscript are from measurements averaged over the last 100 μs before the crowbar. $I_{forward}$ is the peak forward (driving) current during the discharge and $I_{reversed}$ is the maximum current returned from the core when the crowbar is fired. $n_{0,RC}$ is the neutral density calculated from the RC time (section F.2.2) and n_i is the ion density calculated from the electrostatic stored energy just before the crowbar ($U_{crowbar}$, section F.2.1). τ_M and τ_{RC} are the momentum confinement and plasma RC times, and the impedances are calculated using $Z = \langle \frac{V(t)}{I(t)} \rangle$. Section 5.2.7 gives qualitative descriptions of the evolution of the MCX plasma over a shot, and figure 5.14 shows how the input power changes during a shot. Table 5.1 lists the various timescales governing the evolution of the MCX plasma.

Quantity	Units	Equation	R^2
$P_{crowbar}$	MW	$-10^{-9}t^3 - 9\times10^{-6}t^2 - 0.0226t + 23.7$	0.9894
$P_{sustainment}$	MW	$10^{-6}t^2 - 0.0088t + 19.2$	0.95
$Z_{sustainment}$	Ω	$0.0005t + 0.4944$	0.8981
$I_{crowbar}$	kA	$-8\times10^{-7}t^2 + 0.0039t - 5.87$	0.8873
$n_{0,RC}$	m^{-3}	$-7\times10^{7}t^3 + 4\times10^{11}t^2 - 1\times10^{15}t + 7\times10^{17}$	0.8501
M_A		$8\times10^{-11}t^3 - 5\times10^{-7}t^2 + 0.0008t + 0.0349$	0.8289
n_i	m^{-3}	$2\times10^{11}t^3 - 10^{15}t^2 + 2\times10^{18}t - 2\times10^{20}$	0.8258
$\frac{n_0}{n_i}$		$-4\times10^{-13}t^3 + 2\times10^{-9}t^2 - 4\times10^{-6}t + 0.0026$	0.8188
τ_M	μs	$-3\times10^{-8}t^3 - 3\times10^{-7} + 0.316t - 58.5$	0.7538
$I_{forward}$	kA	$3\times10^{-7}t^2 - 0.0001t - 5.09$	0.6793
$Q_{reverse}$	C	$10^{-10}t^3 - 7\times10^{-7}t^2 + 0.0011t - 0.0282$	0.6297
$Z_{crowbar}$	Ω	$-9\times10^{-10}t^3 + 4\times10^{-6}t^2 - 0.0038t + 1.94$	0.6159
$I_{reverse}$	kA	$10^{-9}t^3 - 9\times10^{-6}t^2 + 0.0163t + 7.41$	0.5734
τ_{RC}	μs	$-7\times10^{-8}t^3 + 0.0002t^2 + 0.0359t + 37.7$	0.5533
$U_{crowbar}$	J	$10^{-7}t^3 - 0.0009t^2 + 1.45t + 1664$	0.5411

BIBLIOGRAPHY

[1] O. Anderson, W. R. Baker, A. Bratenahl, H. P. Furth, and W. B. Kunkel. "Hydromagnetic Capacitor." *Journal of Applied Physics.* Vol. 30, No. 2, pp. 188-196 (1959)

[2] H. Biglari, P.H. Diamond, and P. W. Terry. "Influence of sheared poloidal rotation on edge turbulence." *Physics of Fluids B.* Vol. 2, no. 1 (1990)

[3] A. Case, A. DeSilva, R. Ellis, R. Elton, J. Ghosh, H. Griem, A. Hassam, Y. Huang, R. Lunsford, R. McLaren, S. Messer, J. Rodgers, C. Teodorescu. "Magnetic Fluctuations in MCX." *Bulletin of the American Physical Society.* DPP03 poster, October 2003.

[4] Francis F. Chen. *Introduction to Plasma Physics and Controlled Fusion Volume I: Plasma Physics.* Plenum Press: New York, 1984.

[5] A. R. Choudhuri. *The Physics of Fluids and Plasmas: An Introduction for Astrophysicists.* Cambridge University Press: New York, 1998.

[6] R Cohen. *email communication.* October 8, 2003.

[7] A. W. DeSilva. *Plasma Diagnostics.* unpublished notes compiled at the Institute for Plasma Research, University of Maryland, in 1996.

[8] R. F. Ellis, A. B. Hassam, S. Messer, B. R. Osborne. "An experiment to test centrifugal confinement for fusion". *Physics of Plasmas.* Vol. 8, No. 5. (May 2001)

[9] A. B. Filuk. *Particle Confinement and Fueling Effects on the Maryland Spheromak.* U. Maryland-College Park Thesis; Physics Paper Number 91-208. (March 1991)

[10] J. Ghosh, R. C. Elton, H. R. Griem, A. Case, R. Ellis, A. B. Hassam, S. Messer, C. Teodorescu. "Spectroscopic measurements of plasma rotation and ion and neutral atom temperatures in the Maryland Centrifugal Experiment (MCX)." *Physics of Plasmas.* submitted December 2003.

[11] J. Ghosh, R. Elton, H. Griem, C. Teodorescu, A. Case, R. Ellis, A. Hassam, S. Messer. "Spectroscopic Measurements of Plasma Rotation and Temperatures in MCX." *Bulletin of the American Physical Society.* DPP03 poster, October 2003.

[12] R. J. Goldston and P. H. Rutherford. *Introduction to Plasma Physics.* IOP Publishing Ltd: Philadelphia, 1997.

[13] R. Groebner. "An emerging understanding of H-mode discharges in tokamaks." *Physics of Fluids B.* Vol. 5, p. 2343 (1993)

[14] A. B. Hassam. *comments on draft of this dissertation,* December 16, 2003.

[15] A. B. Hassam. "Nonlinear stabilization of the Rayleigh-Taylor instability by external velocity shear." *Physics of Fluids B.* Vol. 4, p. 485 (1992)

[16] A. B. Hassam. "Steady-State Centrifugally Confined Plasmas for Fusion." *Comments in Plasma and Controlled Fusion.* Vol. 18, No. 263 (1997)

[17] Y. M. Huang, A. B. Hassam. "Velocity shear stabilization of centrifugally confined plasma." *Physics Review Letters.* Vol. 87, p. 235002 (2001)

[18] J. D. Huba. *NRL Plasma Formulary.* Naval Research Laboratory: Washington, DC, 2002.

[19] J. D. Jackson. *Classical Electrodynamics.* John Wiley & Sons: New York, 1975.

[20] B. Lehnert. "Rotating Plasmas". *Nuclear Fusion* 11, 1971. pp. 485-533.

[21] B. Lehnert, J. Bergstrom, S. Holmberg and B. Wilner. "On the Interaction between a Fully Ionized Plasma and a Neutral Gas Blanket". *Physica Scripta* 1, 1970. pp. 39-45.

[22] B. Lehnert. "Rotating Plasma Devices". *Progress in Nuclear Energy.* Pergamon Press: New York, 1962.

[23] B. Lipschultz. personal conversation at MIT PSFC. June 9, 2003.

[24] D. R. McCarthy. "Edge Harmonic Oscillations Produced by Toroidal Velocity Shear." *Physics of Plasmas* 9, 6 pp. 2451-2454.

[25] R. McLaren. *personal conversation.* January 8, 2004.

[26] S. Messer, A. Case, A. DeSilva, R. Ellis, R. Elton, J. Ghosh, H. Griem, A. Hassam, Y. Huang, R. Lunsford, R. McLaren, J. Rodgers, C. Teodorescu. "Status of the Maryland Centrifugal Experiment (MCX)." *Bulletin of the American Physical Society.* DPP03 poster, October 2003.

[27] T. G. Northrop. *The Adiabatic Motion of Charged Particles* Interscience Publishers: New York, 1963.

[28] C. A. Ordonez. "Effect of a Plasma Sheath and Ion Injection on Axial Particle and Energy Confinement in a Collisional Mirror Plasma." *Physics of Plasmas* 1, 5 (1994).

[29] V. P. Pastukhov. "Collisional Losses of Electrons from an Adiabatic Trap in a Plasma with a Positive Potential." *Nuclear Fusion* 14, 1 (1974).

INDEX